Title
Vacuum Gap Breakdown For Pulsed Power Liners, From Amperes To Megaamperes

Author
Cordaro, Samuel

Publication Date
2022

UNIVERSITY OF CALIFORNIA SAN DIEGO

Vacuum Gap Breakdown For Pulsed Power Liners, From Amperes To Megaamperes

A dissertation submitted in partial satisfaction of the
requirements for the degree
Doctor of Philosophy

in

Engineering Sciences (Engineering Physics)

by

Samuel Winget Cordaro

Committee in charge:

Sergei Krasheninnikov, Co-Chair
Simon Bott-Suzuki, Co-Chair
Alexey Arefiev
Kevin Quest
George Tynan

2022

The dissertation of Samuel Winget Cordaro is approved, and it is acceptable in quality and form for publication on microfilm and electronically:

University of California San Diego

2022

DEDICATION

To my loving wife Sierra, our lovely child Natalia, my friends and family, and Theo the best dog in the world.

EPIGRAPH

Remember:

Matter. How tiny your share of it.

Time. How brief and fleeting your allotment of it.

Fate. How small a role you play in it.

-Marcus Aurelius, The Meditations, c. AD 171-175

TABLE OF CONTENTS

LIST OF FIGURES

LIST OF TABLES

ACKNOWLEDGEMENTS

To my wife, Sierra, thank you for all your love and patience during this process, and for always keeping my coffee cup full. I could not have gotten through this without you. To my child, Natalia, your screams and laughs pushed me to finish this document. Thank you bug. To my friends and family, thanks for dealing with me.

Dr. Simon Bott-Suzuki, thank you for answering that email so many years ago, it has changed my life. Your support as a mentor in the lab and in life has proved to be invaluable to the success of my experiments and my growth as a person and an experimental physicist.

Professor Sergei Krasheninnikov, thank you for taking a chance on me, and for your patience and understanding. I could not have gotten through this without your help and advising.

Professor Alexey Arefiev, Professor George Tynan, Professor Kevin Quest, thank you all for sitting on my committee and being a part of this process, I appreciate it more than you know.

Thank you to everyone I interacted with during my experiments at Cornell University in the Laboratory of Plasma Studies over the years, you all taught me so much about plasma physics, the ”Black Magic” that is pulsed power engineering and what it is like to be on a large team working for a secular goal. I will always cherish the time I spent there. And a special thanks to Professor Bruce Kusse and Professor David Hammer, thank you for all your insights over the years on my research, the lunches, the beers, the stories, the advocacy, and for letting me play on COBRA once a year.

Dr. William Potter, thank you for all your help during my experiments at Cornell. So many of the beautiful images in this work could not have been possible without your assistance. Oh and thanks for all the Dad info.

Thanks to everyone in the D&D group and at Wizards of the Coast, Sundays have always been a wonderful escape for me over these last 5 years.

Thanks to the National Nuclear Security Administration (NNSA) Stewardship Sciences Academic Alliances (SSAA) program through the Department of Energy (DOE) Cooperative

Agreement No. DE-FC03- 02NA00057, Sandia National Laboratories, and the Cornell Center for supporting my research, schooling, and travel over the years.

Thank you Dr. David Yager-Elorriaga, Dr. Gabriel Shipley, Dr. David Ampleford, and the LDRD program at Sandia National Laboratories for allowing me to participate in a ride along experiment on the Sandia Z-machine. Being able to work with you all and do an experiment on such a large machine was definitely a highlight of my PhD.

Thank you Dr. Louis Sebastian Caballero Bendixen, for teaching me about machining, pulsed power design, and high voltage switches.

Thank you to all the past and present members of the Pulsed Power Plasmas group at UCSD, working in the lab has been a lot of fun with each of you.

Thank you UCSD, you are located in such a beautiful place and it has been so wonderful to get to live here. Thanks to all the coffee shops on campus for fueling my addiction.

Professor Jim Napolitano, thanks for all your help during my undergraduate degree. Your teaching and advising helped set me on this path.

Professor Peter Persans, thank you for giving me the motivation to never ever give up on my goals in physics. You did more for me and the trajectory of my life than you probably will ever know with such simple words.

Chapter 4, in part, is a reprint of material as it appears in the following first author publications: S. W. Cordaro , S. C. Bott-Suzuki, J. Banasek, and Tobias Oliver. ”Effect Of Coaxial Electrode Geometry on the Electric Field Enhancement Factor for a High Voltage Vacuum Gap.” IEEE Trans. Plasma. Sci. Accepted for publication, set to be published online 7/22. S.W. Cordaro, S.C. Bott-Suzuki. ”Time and Space resolved current density mapping in three dimensions using magnetic field probe array in a high voltage coaxial gap.” AIP-Journal of Applied Physics 122, 213303 (2017). S.W. Cordaro, S.C. Bott-Suzuki, L.S. Caballero Bendixen, Levon Atoyan, Tom Byvank, WilliamPotter, B.R. Kusse, J.B. Greenly. ”Two Dimensional Triangulation Of Breakdown In A High Voltage Coaxial Gap.” Rev. Sci. Instrum. 86, 073503

(2015). The dissertation author was the primary investigator and author of these papers.

VITA

2013	B.S. Applied Physics, Concentration in Plasma Physics, Rensselaer Polytechnic Institute, Troy, NY
2018	M.S. Engineering Sciences (Engineering Physics), University of California San Diego, La Jolla, CA
2022	Ph.D. Engineering Sciences (Engineering Physics), University of California San Diego, La Jolla, CA

PUBLICATIONS

S. W. Cordaro , S. C. Bott-Suzuki, J. Banasek, and Tobias Oliver. ”Effect Of Coaxial Electrode Geometry on the Electric Field Enhancement Factor for a High Voltage Vacuum Gap.” IEEE Trans. Plasma. Sci. Accepted for publication,set to be published online 7/22

J. T. Banasek 1, T. G. Oliver 1, S. W. Cordaro 1, S. C. Bott-Suzuki . ”Free space Thomson scattering to study high energy density shocks.” : Rev. Sci. Instrum. 92, 093503 (2021)

S. C. Bott-Suzuki, A. Bykanov, O. Khodykin, M. Tillack, S. Cordaro, C. McGuffey. ”Characterization of Plasma Emission in the 1-6 nm Band from Laser-Irradiated Cryogenic Xenon Targets” Journal of Applied Physics 126, 113103 (2019)

Simon C. Bott-Suzuki , Samuel W. Cordaro, L. Atoyan, T. Byvank , W. Potter, B. R. Kusse, J. B. Greenly, D. A. Hammer and C. A. Jennings. “The Role of Ion Acoustic Instability in the Development of the Azimuthal Current Density Profile in Liner Experiments at 1 MA” (Invited paper) IEEE Trans. Plasma Sci, 46, 1921 (2018)

S.W. Cordaro, S.C. Bott-Suzuki. ”Time and Space resolved current density mapping in three dimensions using magnetic field probe array in a high voltage coaxial gap.” AIP-Journal of Applied Physics 122, 213303 (2017)

S. C. Bott-Suzuki, S. W. Cordaro, L. S. Caballero Bendixsen, L. Atoyan, T. Byvank, W. Potter, B. R. Kusse, J. B. Greenly and D. A. Hammer. ”Study of the time-resolved, 3-dimensional current density distribution in solid metallic liners at 1 MA.” Phys. Plasmas 23, 092711 (2016)

L.S. Caballero Bendixsen, S. C. Bott-Suzuki, S. W. Cordaro, K. Mahadevan, S. Chapman, J.P. Chittenden.“Axial Mass fraction measurements in a 300kA dense plasma focus.” Phys Plasmas, 23, 093112 (2016)

S. C. Bott-Suzuki, S. W. Cordaro,L. S. Caballero Bendixsen, I. C. Blesener, L. Atoyan, Byvank, W.Potter, K. S. Bell, B. R. Kusse,J. B. Greenly,and D. A. Hammer. ”Investigation of the effect of a power feed vacuum gap in solid liner experiments at 1 MA” Phys. Plasmas 22, 094501 (2015)

S. C. Bott-Suzuki, L. S. Caballero Bendixsen, S. W. Cordaro, I. C. Blesener, C. L. Hoyt, A. D. Cahill, B. R. Kusse, D. A. Hammer, P. A. Gourdain,C. E. Seyler, J. B. Greenly, J. P. Chittenden, N. Niasse, S. V. Lebedev, and D. J. Ampleford. ”Investigation of radiative bow-shocks in magnetically accelerated plasma flows.” Physics Of Plasmas 22, 052710 (2015)

S.W. Cordaro, S.C. Bott-Suzuki, L.S. Caballero Bendixen, Levon Atoyan, Tom Byvank, William Potter, B.R. Kusse, J.B. Greenly. ”Two Dimensional Triangulation Of Breakdown In A High Voltage Coaxial Gap”. Rev. Sci. Instrum. 86, 073503 (2015)

ABSTRACT OF THE DISSERTATION

Vacuum Gap Breakdown For Pulsed Power Liners, From Amperes To Megaamperes

by

Samuel Winget Cordaro

Doctor of Philosophy in Engineering Sciences (Engineering Physics)

University of California San Diego, 2022

Sergei Krasheninnikov, Co-Chair
Simon Bott-Suzuki, Co-Chair

Vacuum gap breakdown at high voltages, in the range of tens of kilovolts to megavolts, occurs in many systems where high-current conduction is required. Several standard geometries have been extensively investigated under both pulsed and D.C. conditions and are generally well understood and documented. To date, little detailed analysis of explosive emission in coaxial geometry has been performed, although this geometry is a common feature of high-energy devices including vacuum transmission lines, switch systems, and fusion devices.

Of specific interest is the evolution of the current density and magnetic field in space and time along the electrodes and how it effects plasma formation in the gap. As current rises, plasma channels form in the gap as pathways to travel to the load. If the channel formation is asymmetric in distribution about the azimuth, the resulting current could be non-uniform, leading to early time scale instabilities in the load.

Experiments were performed on machines with currents ranging from amperes to megaamperes to investigate implications of asymmetric breakdown distribution and how these effects scale, via the use of magnetic field probe array around the load to measure the magnetic field evolution, and thus current density distribution, in time and space. Results show a strong link between asymmetric plasma formation and current distribution in the load, which scales from ampere to megaampere experiments. Fowler-Nordheim analysis at 240 amperes for gap sizes $>150\mu$m, shows geometry was the driving factor in breakdown initiation and distribution, while at gap sizes $<100\mu$m surface profile played the dominant role. Through electroplating and dip-coating metals of varied work functions, it was found that at 1 megaampere the surface profile of the material dominates in driving the formation of breakdown channels in a vacuum gap, and in the case of a graphite coating a uniform gap and current distribution was achieved. With an external axial magnetic field at 1 megaampere, it was found that the asymmetric distribution of breakdown could be mitigated, and uniformity of gap plasma could be achieved. Experimental results show while asymmetric breakdown does lead to asymmetric current in the load, effective and mitigation is possible.

Chapter 1

Motivation

”A philosopher without clothes and one without books. ’I have nothing to eat,’ says he, as he stands there half-naked, ’but I subsist on the logos.’ And with nothing to read, I subsist on it too.” - Marcus Aurelius, The Meditations,c. AD 171-175.

1.1 Energy Production/Consumption

Energy production and consumption is essential for the production of food, consumer goods, transportation, heating/cooling and lighting homes, facilitating and maintaining communications etc. All things that give rise to a quality of life that is unprecedented in the whole of human history. This energy consumption increases with each year Figure 1.1, from this it is easy to posit that with increased energy consumption comes increased quality of life. A simple projection (overlayed in blue) of 100 years in the future shows the energy consumption roughly doubles. This is especially concerning as the vast majority of energy that is produced and consumed comes from sources that are expected to be depleted in decades Figure 1.2. Further concerning still is the detrimental environmental cost of the production and consumption of fossil fuels with the generation of greenhouse gases.

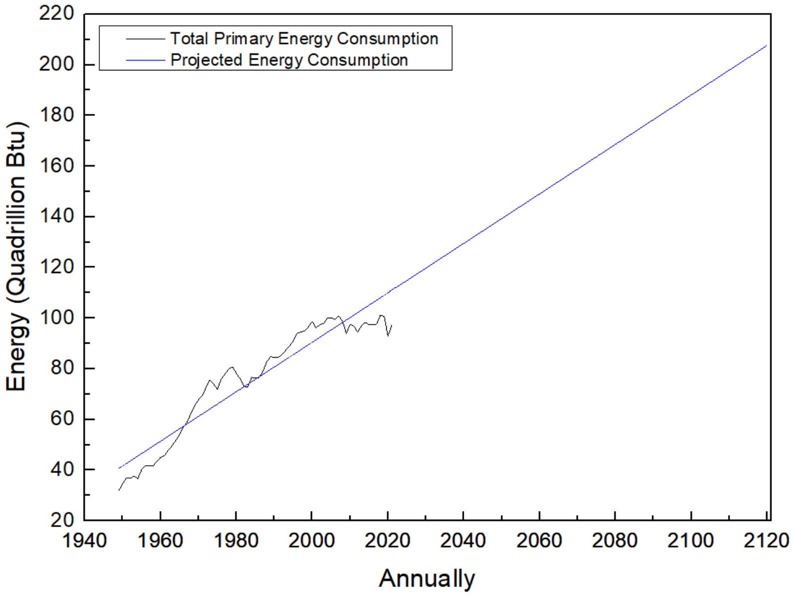

Figure 1.1: Energy Consumption (black) of the United States of America (data taken from U.S. Energy Information Administration) and a simple linear fit projection 100 years into the future.

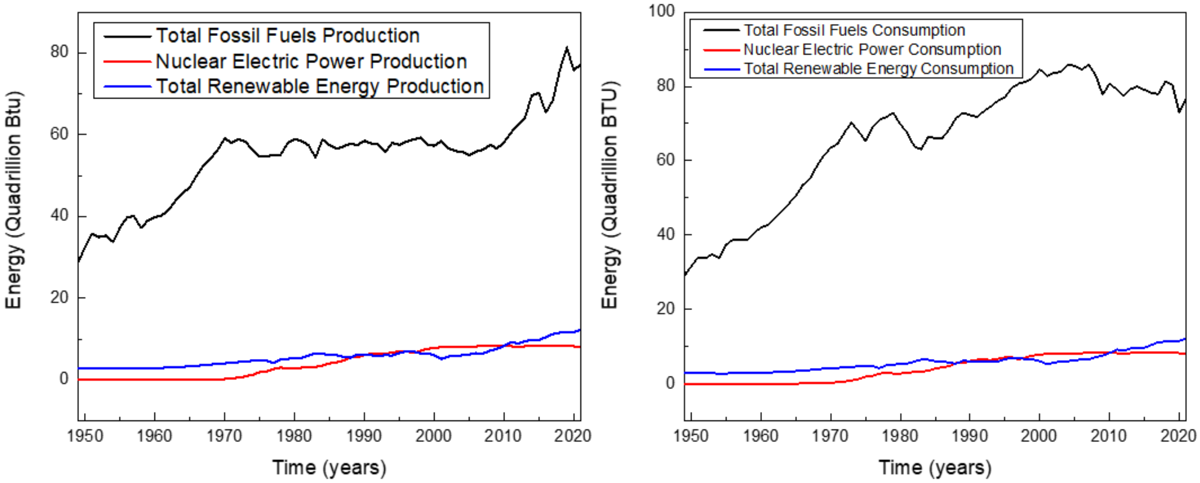

Figure 1.2: Energy production (left) and consumption(right) separated by type of energy of the United States of America (data taken from U.S. Energy Information Administration)

Of further concern is the detrimental environmental cost of the production and consumption of fossil fuels with the generation of greenhouse gases. These issues are exacerbated when considering the stratification of those who benefit from the increased consumption of fossil fuels, and the ever increasing geopolitical pressures that arise from the increased need for said fossil fuels. With a world population that is projected (Figure 1.3) to increase by 1-10 billion people (baring a sharp drop in quality of life), it is unlikely these issues will go away and will most certainly only get worse.

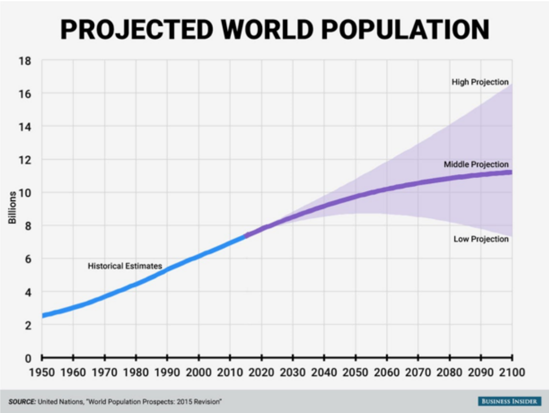

Figure 1.3: Projected human world population through the year 2100, with high, middle, and low projections. This data is sourced from the United nations, and the graph is taken from Business Insider.

In order to curb the detrimental environmental effects of the consumption and production of fossil fuels, emission limits must be set and met. This solution is at odds with the projected energy consumption demands. So then to protect the environment and meet the ever expanding energy demands, a different, powerful approach to energy production is needed. Fusion energy is an attractive solution to this energy needs criteria, especially considering that most nations are now closing nuclear power plants. Fusion is safe and has large fuel reserves with minimal damage to the environment. Furthermore, fusion can easily provide large quantities of electricity in a reliable manner, that could easily replace fossil fuels. Obviously fusion does not come without significant downsides, namely the scientific and engineering challenge of getting it working as well as waste handling, and the potential of tritium leakage.

The remainder of this chapter will outline the basics of D-T Fusion reactions and and briefly describe the inertial and magnetic confinement approaches to fusion before narrowing in to focus on a single approach to fusion, namely inertial confinement and magnetized liner inertial fusion on the Sandia Z-Machine.

1.1.1 D-T Fusion

Fusion is a form of nuclear energy whose nuclear processes occur at the opposite end of the atomic masses spectrum as fission. Where Fission involves the splitting of U^{235}, a heavy nuclei, fusion is the coming together (fusing) of light elements like hydrogen (H) and its isotopes deuterium (D) and tritium (T). For reference, the fusion of hydrogen is the main reaction that powers our sun [31] [15],[20].

In the most basic of terms a light element fusion reaction can be initiated generating a nuclear reaction by having two light elements (like deuterium) bombard one another, getting them close enough together to fuse. The problem with having two deuterium nuclei undergo a nuclear reaction is that they have to get within a nuclear diameter of one another. At such a close distance, the inter-particle Coulomb potential generates a strong repulsive force between the two positively charged deuterium nuclei. This repulsive force in turn deflects the particle orbits and decreases the likelihood that a a nuclear reaction will occur. This decreased likelihood can be overcome with sufficiently high temperatures and the use of two different light elements such as deuterium (D) and tritium (T). While there are other possible fusion reactions such as D-D or D-^3He, the D-T reaction has the highest cross-section at lower temperatures (Figure 1.4).

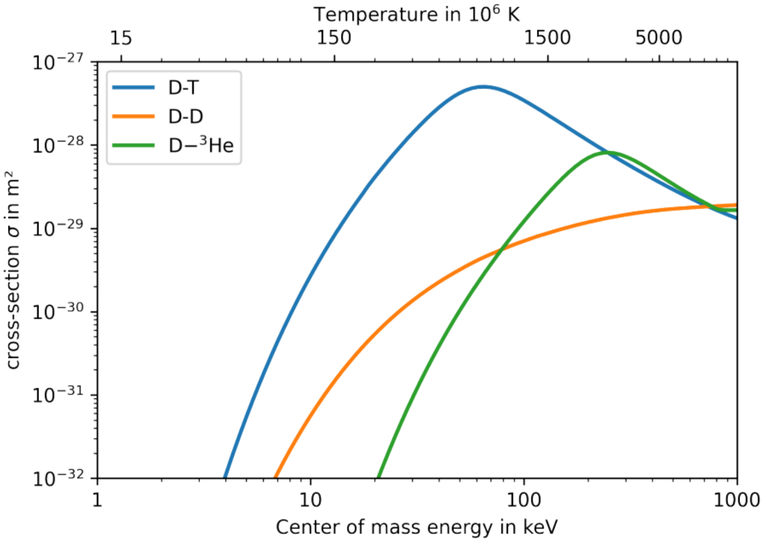

Figure 1.4: Cross section of different fusion reactions. Data are taken from ENDF-Database

Subsequently, the use of light elements like hydrogen is responsible for one of main advantages to fusion energy, namely fuel reserves. As deuterium occurs naturally in ocean water (1 atm D 6700 atoms of hydrogen) and is very inexpensive and easy to extract. Some current estimates say it would take 2-3 billion years to use up all the deuterium in the ocean. However, tritium does not occur naturally on earth and is obtained by breeding with the lithium isotope Li^6. Estimates of the current available Li^6 on Earth indicate it would take tens of thousands of years to exhaust.

With the fusion of a deuterium nucleus with a tritium nucleus,

$$D + T - > \alpha + n + 17.6MeV \tag{1.1}$$

the product is alpha particles (α), neutrons (n) and a significant amount of nuclear energy (17.6 MeV), which corresponds to 3.5 MeV in the alpha particle and 14.1 MeV in the neutron. These high energy neutrons can then be captured and their kinetic energy harnessed in the form of heat that boils water and spins turbines.

The energies required to do this are immense and have enormous number of physics related issues and are subsequently topics of major importance to fusion research. Many different approaches exist to attempt to solve theses issues and have been outlined extensively in works far better than mine.

1.1.2 Magnetic Confinement Fusion

Magnetic Confinement Fusion (MCF) is a fusion approach that relies on the fact that ions and electrons cannot travel across magnetic field lines easily, with this fact large magnetic fields can be used to confine a hot dense plasma in order for particles to fuse [59],[4].

The basic principle of MCF is that in a strong magnetic field a particle is bound to the magnetic field lines as a result of the Lorentz force, in straight magnetic field lines the particle will follow a helical path around the magnetic field, with a radius of gyration known as the Larmour radius ($r_\perp = v_\perp/\omega_c$). These particles gyrate in a linear direction of the center of the gyration circle, with a parallel velocity along the field line. The perpendicular component of the particle velocity is in then perpendicular to the magnetic field, and has an angular cyclotron frequency, $\omega_c = qB/m$, where q is the charge, B is the magnetic field, and m is the mass of the particle. This means that due to their weight difference, electrons and ions will gyrate at different rates with different Larmour radii, and if the magnetic field is non uniform they will also move in different directions. To address this a MCF fusion reactor has a magnetic field strength chosen such that ions radii of gyration are much smaller than the dimension of the device. The most typical design used is that of a toroid, or tokamak. It consists of a toroidally shaped vacuum chamber with a D shaped cross section around which magnetic field coils are wound. The toroidal field coils generate a toroidal magnetic field, a transformer coil is placed in the center of the toroid and induces an electric field along the toroidal field lines which drives a toroidal flow for ions and electrons in opposite directions. This opposite movement generates a current in the plasma, which generates a poloidal magnetic field. The superposition of the toroidal and poloidal field lines result in field lines that wind around the torous in a nested like shape that confine the charged plasma particles.

To summarize, requirements to achieve ignition with MCF:

- Confine long timescale$\sim 10s$
- Have the fuel reach densities of$\sim 10^{23} m^{-3}$ and temperatures of $\sim 10 keV$

1.1.3 Inertial Confinement Fusion

Inertial Confinement Fusion (ICF) is a fusion approach that relies on the inertia of the fuel to provide the confinement needed for particles to fuse [43].

To achieve the necessary conditions for fusion (high pressure, short time scale, greater than 4keV temperatures), ICF targets are typically a spherical capsule made up of a multi-layer shell filled with a low density gas ($\leq$ 1 mg/cm3). The outer region of the shell is known as the ablator [24] and the inner being made up of frozen deuterium-tritium, the fuel. An external driver delivers energy rapidly ($<$1 μs) to the ablator, this heats up and expands outward. As the ablator expands, the rest of the shell is forced inward to conserve momentum, behaving in accordance with the rocket model [2]. The work done on the fuel is then the product of the pressure generated by the ablation process multiplied by the enclosed volume of the shell. Therefore, for some pressure, a thinner shell that encloses more volume can be accelerated faster than a thicker shell (this leads to issues on the interface of these two layers). As the rest of the shell compresses inward the fuel consists of two distinct regions: a central hot spot where 2-5 percent of the fuel is, and a dense main fuel region comprising of the remaining of the mass providing the compression/confinement. In the case of D-T reaction (Eq. 1.1) fusion occurs when energy production and α particle deposition from the central hot spot region is sufficient enough to ignite a self-sustaining thermonuclear burn shock front that propagates radially outward into the main fuel to produce large amounts of energy.

Typically, to be viable and to achieve ignition, minimum thresholds of pressure and temperatures must be met. These values are determined by the size of the capsule, and the power (E/t) of external driver used.

To summarize, requirements to achieve ignition with ICF:

- Confine over short timescale $\sim 10^{-9}s$
- Triple product of density, temperature, time $> 10^{21} keV s/m^{-3}$
- High fuel density $n_{fuel} \sim 10^{31} m^{-3}$

1.1.4 Magneto Inertial Fusion

Magneto Inertial Fusion (MIF) differs from ICF in that a strong magnetic field is applied to the fuel in an attempt to reduce ignition conditions on standard ICF. The large magnetic field changes the plasma kinetics and energy transport of the system to lower requirements for pressure, density, and fuel compression to reach the conditions for fuel self-heating and ignition [68] [49].

An MIF approach is typically characterized by a thick cylindrical liner to compress the fuel at a slower speed than traditional ICF, a preheating of the fuel to a temperature threshold early in the current rise to reduce adiabatic compression needed to reach keV temperatures, and magnetization of the preheated fuel to reduce cross field thermal fluxes [16] that can cause energy losses during implosion. Much like ICF, fusion in MIF occurs near the implosion stagnation phase (peak compression) when the fuels internal energy is maximized. During this phase, the thick liner provides the majority of the radial inertial confinement and the fuel self heating is enhanced by the external magnetic confinement within the volume of the fuel [40].

1.1.5 Magnetized Liner Inertial Fusion

The Sandia Z-machine [79][74] is the worlds largest pulsed power accelerator, it can store up to 22 MJ in its capacitor banks and discharge in$\sim 100ns$. This is a linearly rising pulse with a peak electrical power of 80 TW and a peak current of up to 26 MA. The Z-machine is used to study plasmas in extreme regimes, as well as to study MIF and ICF experiments. The Z-machine (Figure 1.5) has 36 Marx generators composed of 60 2.6 microfarad capacitors each charged to 90kV, storing 632 kJ, for a total of $\sim 22MJ$ of stored energy. This stored energy is discharged in a 1.3 μs into the pulse forming section. In this section there are series of switches and low-inductance transmission lines that compress the electrical energy in time, which allows the peak electrical power delivered to the insulator stack is as high as 80 TW in a$\sim 100ns$ linearly rising current pulse. Typically based on load hardware and inductance, Z delivers 26 MA to the load.

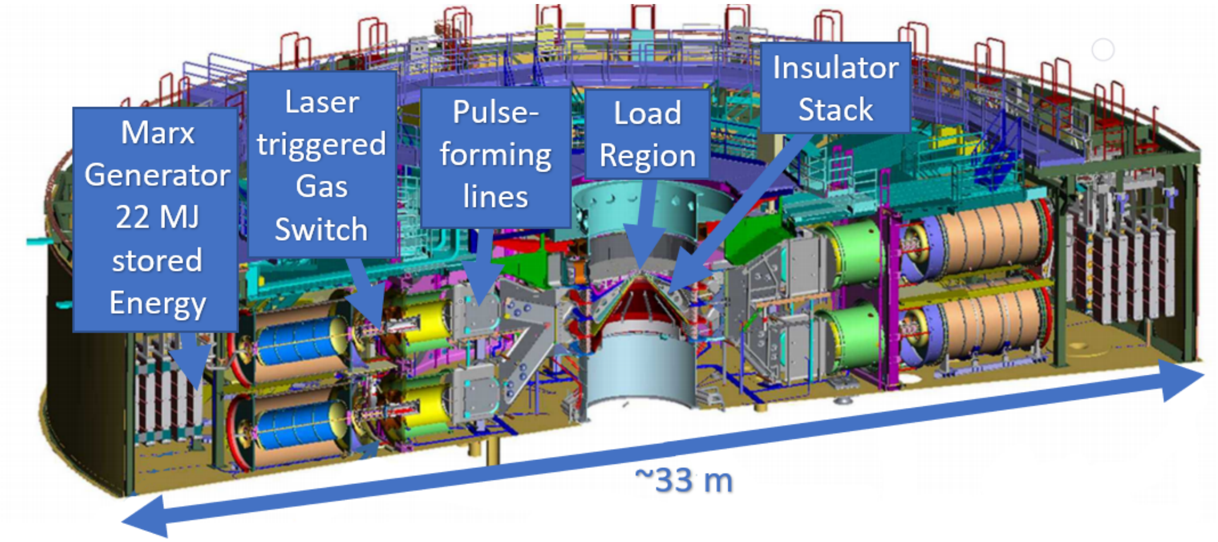

Figure 1.5: Cross section of the Sandia Z-machine, with various components labeled, and the diameter of the machine shown.

Magnetized Liner Inertial Fusion (MagLIF) experimental MIF load design that is fired on the Sandia Z-machine [80], [78][77] [24]. The target is a thick 1 cm tall solid cylindrical metal liner made of Beryllium or Aluminium and filled with a high pressure gas fuel ($\sim 1-5mg/cc$ density of deuterium gas (Figure 1.6). Figure 1.6(a) is the magnetization phase in which an axial magnetic field (15-30T) is generated throughout the load on a μs timescale by an external magnetic field coil placed around the liner region, during implosion this field is compressed to

100's of Tesla. The axial field limits thermal conduction losses from the hot fuel to the cold liner walls during the implosion phase, in addition it aids in increasing trapping of charged particles in the radial direction during stagnation. As the Z-machine discharges, an azimuthal magnetic field is formed around the liner and begins to drive liner implosion via the Lorentz force (JxB). Figure 1.6 (b) the preheat phase, as the liner implosive begins, a 527 nm kilojoule-class laser is coupled to the cold DT gas fill causing the fuel to be preheated, which increases the initial adiabat of the fuel. Figure 1.6 the compression stage, where a high pressure ($\sim Mbar$) high conductive, high β (thermal/magnetic pressure ratio) and the axial magnetic field is partially frozen into the plasma. This is a quasi adiabatic implosion at subsonic speeds, and the liner accelerates to a peak implosion speed ($\sim$70 km/s) driving the plasma to a small radius on axis to reach fusion conditions.

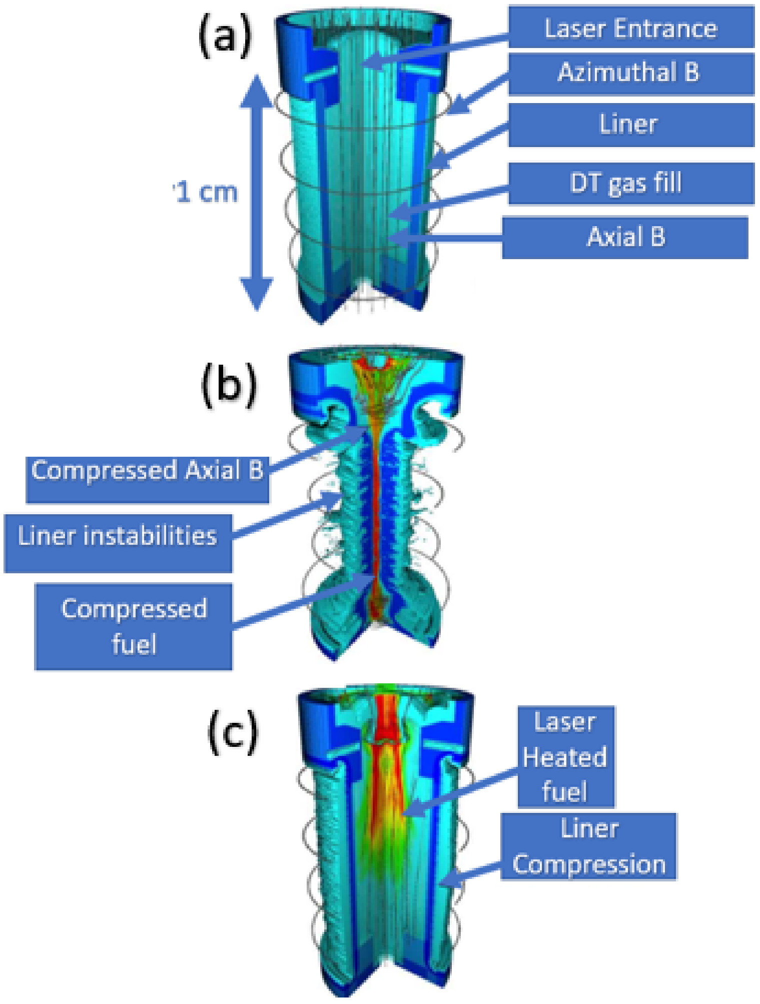

Figure 1.6: Schematic diagram of MagLIF concept, with a) being the magnetization and start of implosion phase b) Laser preheat phase c) Compression phase

The major dynamics of the MagLIF experiment can be described by the analytical model outlined in [52].

1.2 Barriers to Liner Fusion

Why the above sections make it seem like achieving these requirements is straight forward, they are in fact not. High gain inertial fusion has eluded researchers for many years, and has lead to a robust amount of high energy density (HED) research and development of many different approaches to fusion, with only a few listed above. Barriers to achieving fusion range from physical ones, asymmetries in current delivered to the load, energy losses at the load/load region, surface interactions of the various load materials, current delivery magnitude and design limitations, laser fuel energy coupling.

Of specific interest to this work is asymmetries in current delivered to the load, more specific still is the way in which the liner is mounted to the cathode power feed in the Z-machine. Typically the liner is fixed to the upper anode and the entire assembly unit is inserted into the cathode which is fixed to the power feed. As a result of this, a small azimuthal vacuum gap (∼25μm) between the liner and the cathode remains, as shown in the cartoon of Figure 1.7. The existence of this gap could lead to asymmetries in the current delivered to the load.

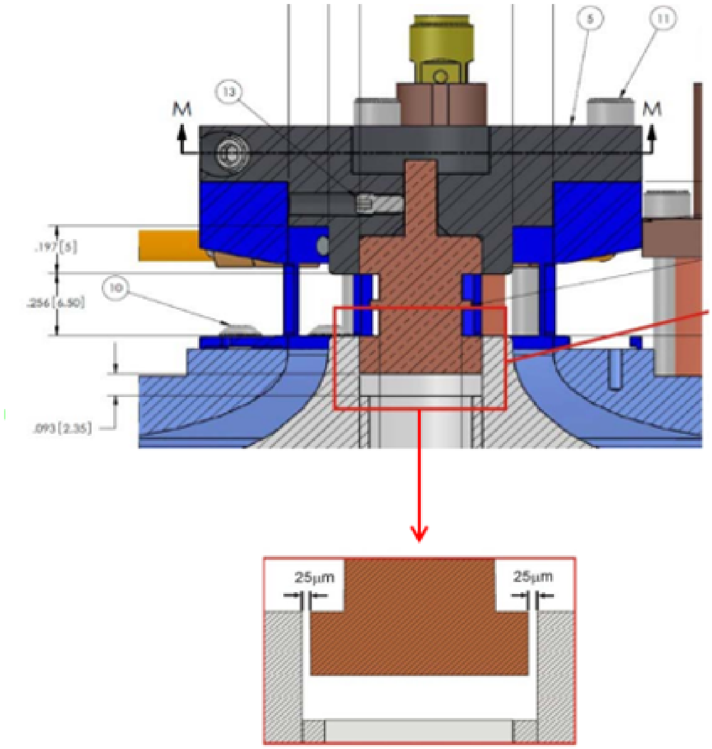

Figure 1.7: two dimensional cross section of the MagLIF experiment showing a coaxial gap at the cathode power feed.

This can be explored simply by using the semi-analytical model of the liner equation of motion [52],

$$\dot{r}_l = \frac{p_{l,s=N_{l,s}} - p_{\text{Bazimuth,l, }v} - p_{\text{Baverage axial },v}}{\frac{m_{l,S}}{2}} 2\pi r_l h \tag{1.2}$$

where r_l is the liner radius, $P_{l,s=N_{l,s}}$is the pressure at the liner interface with vacuum, $p_{\text{Bazimuth,l, }v}$ is the azimuthal magnetic field pressure, $p_{\text{Baverage axial },v}$ is the axial magnetic field pressure,$m_{ls}$is the liner mass, and h is the height of the liner, and the values in Table 1.2.

Table 1.1: Typical experimental quantities for the MagLIF fusion load on the Sandia Z-Machine.

Applied Axial magnetic field	Peak Current	Liner radius	Fuel radius	Fuel Pressure	Liner outer radius	Mass density liner	Liner Pressure	Liner Height
30 T	18 MA	0.465 mm	2.325 mm	3 GBar	3.48 mm	428 mg/cm	2.48 MBar	7.5 mm

If we then mirror the 2-D image and the 1-D model about the y-axis (Figure 1.8) and then split the total current from the left hand side to the right hand side, we can then plot the equation of motion for the liner versus the percent difference in the current from the left hand side to the right hand side (Figure 1.9).

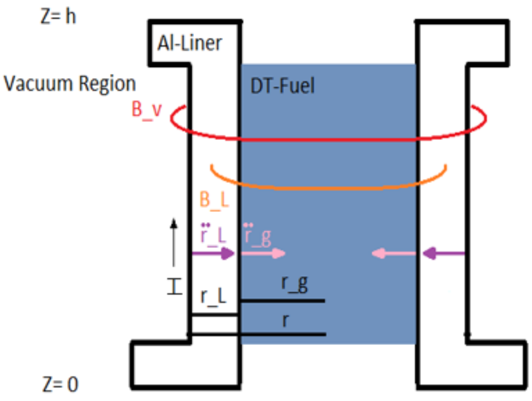

Figure 1.8: Cartoon of the experimental schematic of a two dimensional slice of the MagLIF fusion liner load.

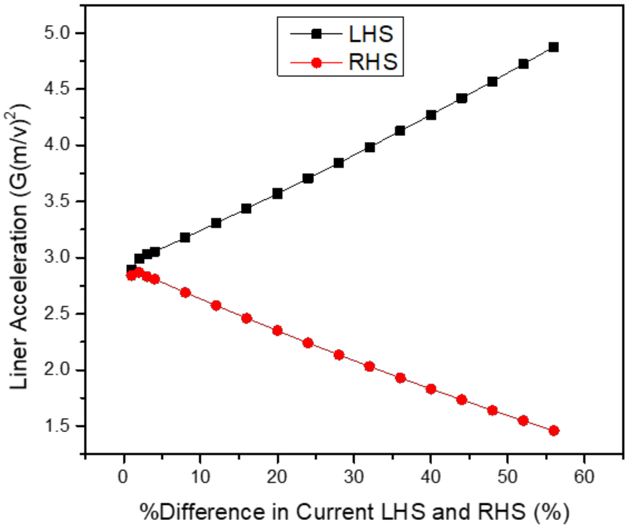

Figure 1.9: Liner Acceleration versus the percent difference in current from the left hand side and the right hand side.

This shows that if an asymmetry exists and persists in a MagLIF experiment, even as small as a 1% difference from the LHS and RHS, the LHS will accelerate 1.73 % faster than the RHS. This would be detrimental to the overall success of the liner compression phase due to a strong dependence on the current symmetry in the load. The existence of the coaxial gap at the cathode power feed is the topic of the remainder of this document. Results will show asymmetries exist in current density distribution in the 10's of %.

1.3 Physics Questions

If we consider that the push fit design of MagLIF we can narrow our scope down further to the behavior of this gap. Consider that the existence of the gap could lead to asymmetries in the current load we can pose the following questions.

1. As stated above, the re-loadable MagLIF design potentially has a coaxial vacuum gap at the cathode power feed. As the current rises the vacuum gap will breakdown, forming plasma channels for the current to travel to the load. What happens if the plasma channels that form are asymmetric about the azimuth of the coaxial vacuum gap? Does this have implications for current distribution in the liner load?
2. Ignition sale drivers for pulsed power inertial fusion will be on the order of 60-70 MA, do data from small university scale experiments (100's of amps) to larger machines (MA scale) in a way that allows prediction of the effects of issues at the ignition scale? Are these effects expected to be exacerbated or mitigated?
3. If the plasma channels that form in a coaxial vacuum gap are asymmetrically distributed about the azimuth what are the driving factors in the development of these asymmetries ?
4. If asymmetries in the vacuum gap lead to asymmetries elsewhere in the liner load, this could prove detrimental to the liner compression phase as it depends strongly on current symmetry in the load. With asymmetric compression fusion is not possible. Can the presence of these asymmetries be mitigated? If so, how/why?

Chapter 2

Coaxial Gap Breakdown Machine

”It makes me nervous when I see you have the hammer out in the lab” - Dr. Simon Bott-Suzuki

2.1 Design Parameters

Vacuum gap breakdown at high voltages, typically in the range of tens of kilovolts to megavolts, occurs in many systems, particularly where high current conduction is required. Several standard geometries, such as sphere-sphere, plane-plane, and point-plane, have been extensively investigated under both pulsed and D.C. conditions and, in general, are well understood and documented [58][11][35][57]. To date, little detailed analysis of explosive emission in coaxial geometry has been performed, although this geometry is a common feature of high energy devices including vacuum transmission lines and switch systems. The present work is motivated by the need to better understand the mechanisms by which breakdown initiation occurs in a coaxial gap over a few nanoseconds to a few microseconds at tens of kV at gap sizes of up to 1 mm, and how these behaviors scale to large machines.

An experimental system was developed at the University of California San Diego to study the mechanisms and influences of coaxial geometry vacuum gaps. This table top experiment, the Coaxial Gap Breakdown (CGB) machine, was designed for ease of use and scale-ability to existing accessible machines. Of specific importance is choosing a relevant current pulse width, current, voltage, and simple load design. The Cornell pulsed power machine COBRA has a peak current of 1.1 MA, at a variable rise time of 120 ns,and a voltage of 70 kV. COBRA's current pulse is the same rise time as the as the Sandia Z-machine, and is equivalent in magnitude to the pre-pulse current (Figure 2.1). With these values in mind we chose a fast current pulse 150 ns, low current 250 A, and 25 kV. With these values we fall into a scaleable to megaampere regime. The combination of low current and high voltage was to isolate breakdown behavior in the coaxial gap.

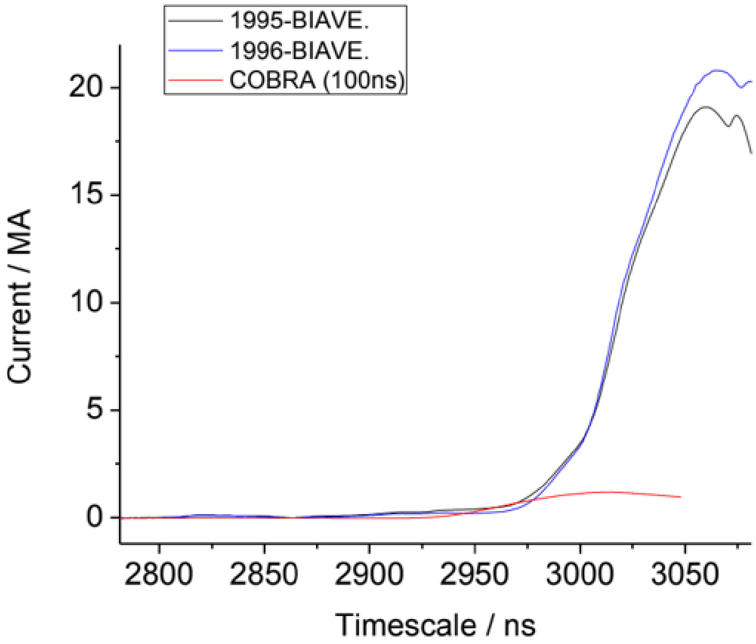

Figure 2.1: Z-machine pre-pulse current with COBRA pulse ()

2.2 Coaxial Gap Breakdown Machine for Table-Top Pulsed Power

The majority of the work presented in this thesis was performed at the Pulsed Power Plasmas laboratory at University of California, San Diego on the Coaxial Gap Breakdown (CGB) machine (Figure 2.2), that I have built from the ground up. CGB current and voltage pulse (Figure 2.3) is achieved through the use of a simple charge circuit that is charged and held by a trigatron air gap, which is subsequently triggered via a trigger unit. The pulse is truncated through a water resistor pulse forming line an sent to the chamber. The machine is fired at a repetition rate of ∼0.1 Hz via the Master Control Program (MCP) tower which triggers the trigger unit box and activates and collects all data from all diagnostics. The remainder of this section will outline specifics of how the machine works and the diagnostics used.

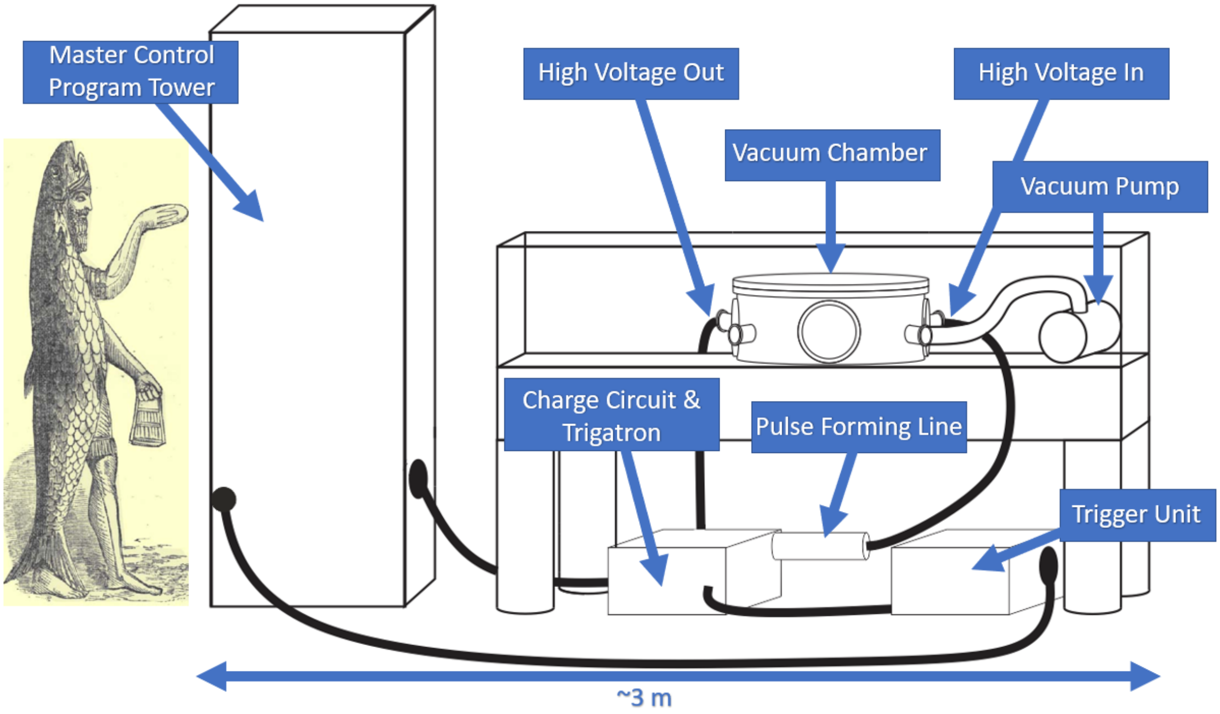

Figure 2.2: Coaxial Gap Breakdown Machine Diagram with ”human” for scale

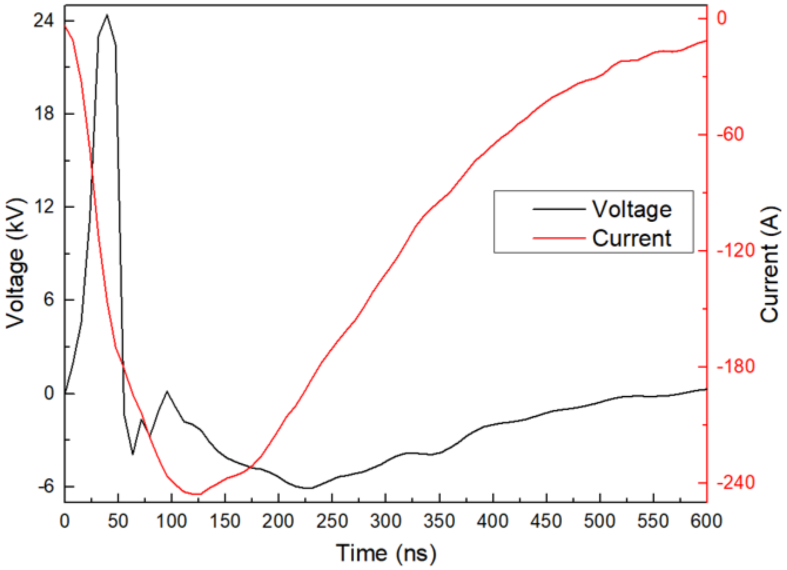

Figure 2.3: Typical current (red) and voltage (black) profiles of the CGB machine.

2.3 Circuit Design

In order to build an experiment with a current and voltage pulse that meets the design parameters of fast rise time, low current, with high voltage we modeled circuits using CASTLE. CASTLE is a freeware circuit analysis and simulation code that is designed for pulsed power systems with transmission lines.

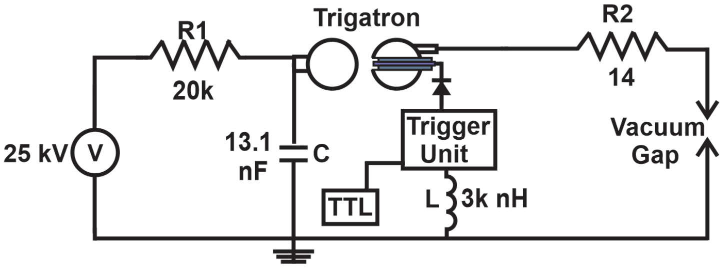

Figure 2.4: Charging Circuit simulation diagram.

Figure 2.4 shows the simple RC charge circuit design that is connected to the load (Vacuum spark gap - inductance) via a spark gap trigger (Trigatron). The simulated and experimental current pulse into the load is shown in Figure 2.5, as seen they are in good agreement.

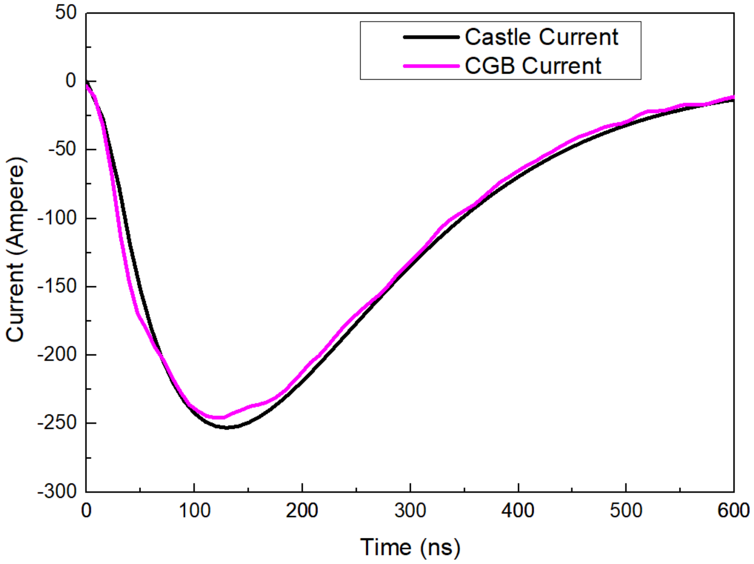

Figure 2.5: Current signals for CASTLE simulation (black) overtop typical CGB machine current (pink).

2.3.1 Spark Gap Triggering

In order to trigger the experiment at a specific time to align diagnostics, we make use of a Trigatron [63]. A Trigatron is a triggerable spark gap, that is low cost for high energy switching. The construction is very simple, a diagram of the sphere sphere Trigatron used on the CGB is shown in Figure 2.6.

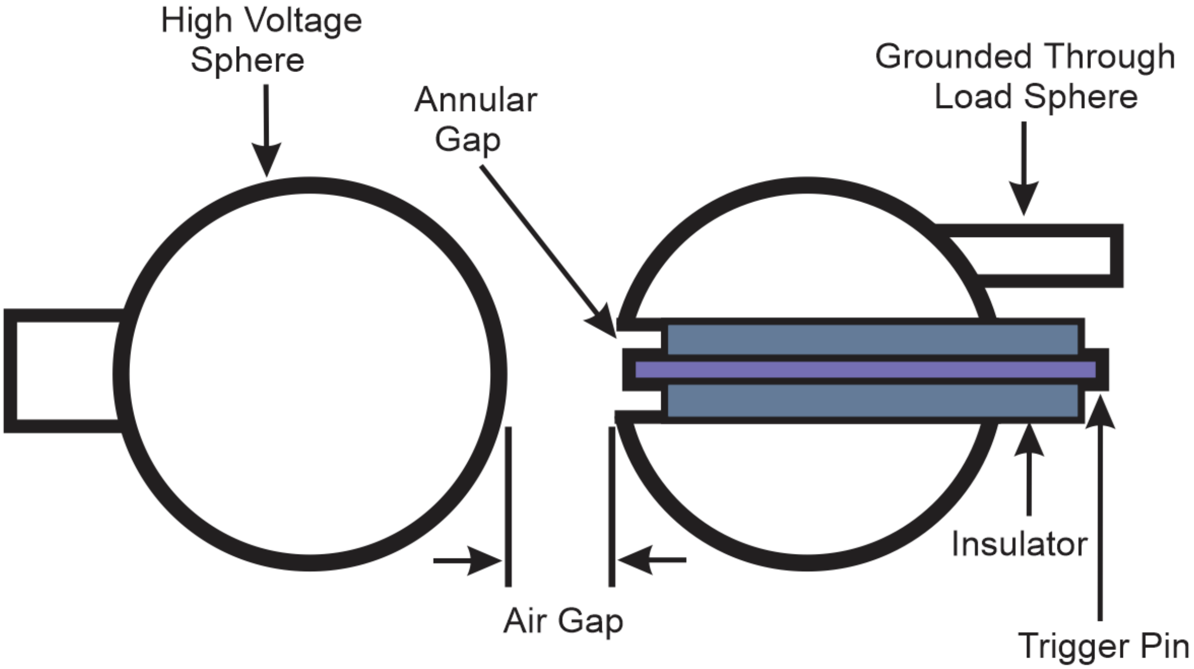

Figure 2.6: Trigatron diagram

The basic operation of the Trigatron in the CGB circuit is as follows: The high voltage sphere is charged via charge circuit (Figure 2.4) and held at 25 kV. This is achieved by having the Air Gap at a self=break voltage of 26 kV (measurement). A separate trigger circuit is on the trigger pin line, that consists of a trigger unit (5 kV) and reverse current diode protection. The trigger unit is pulsed and a high voltage breakdown occurs between the trigger pin and metal annular gap, this pulsed breakdown ionizes a portion of the gap causing the high voltage sphere to close the air gap and sends current into the chamber.

2.3.2 Water Resistors

In order to achieve the pulse shape and rise time in the design parameters section (Figure 2.5) the resistor R2 in the charging circuit diagram (Figure 2.4) needs to be 14 ohms. A water resistor is used here because it is easy to assemble at a relatively cheap price and can absorb large amounts of energy. In addition it adds no inductance to the circuit. With dionized water the resistor would have a resistance around 2-3 mega ohms, in order to decrease the resistance chemical solutions can be mixed into the dionized water. Figure 2.7, courtesy of Ness Engineering incorporated, shows the resistivity of water resistor solutions based on salt concentration, it is immediately seen that to achieve the lowest resistance, mixing a moderate amount of Ammonium Chloride into the dionized water is the best choice.

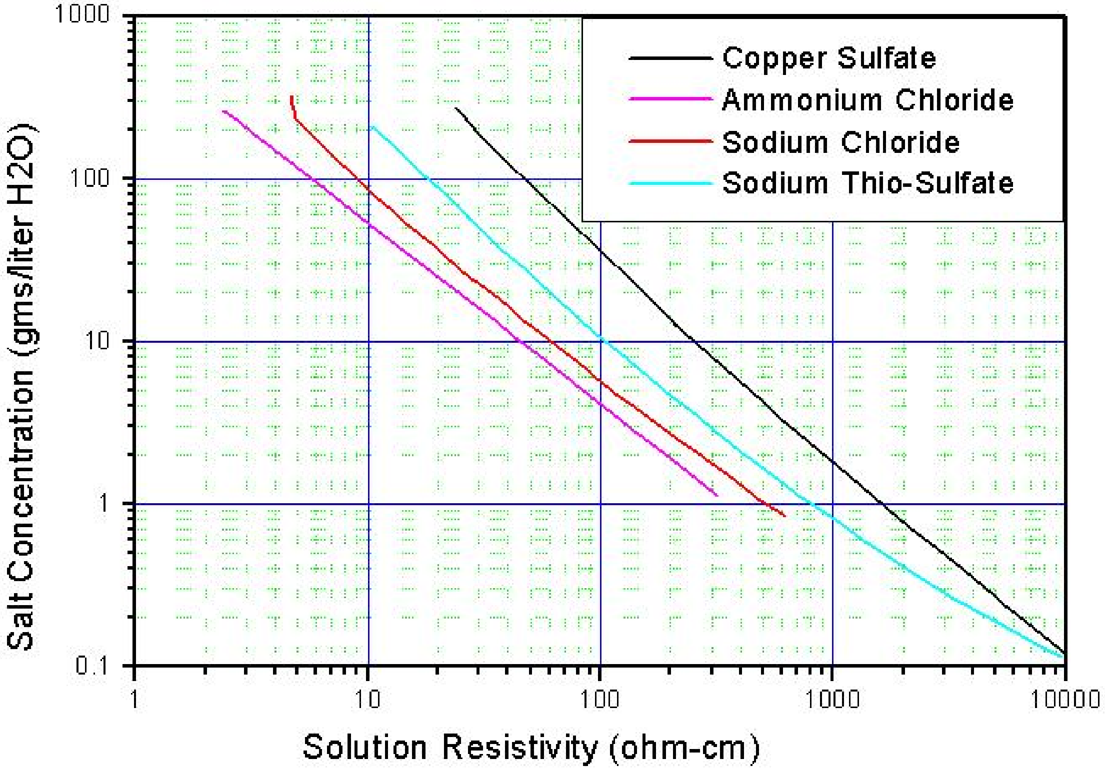

Figure 2.7: Resistivity of chemical solutions based on salt concentration

2.4 Master Control Tower

To generate statistically relevant data, the CGB machine was upgraded from a single shot manual push machine to a repetition rated machine that fires and collects data at 0.076 Hz (1 shot/13 seconds). To do this all of the components required to trigger and collect data in the system were consolidated into one tower, hence forth known as the Master Control Program (MCP) Tower, Figure 2.8). The tower consists of: Two oscilloscopes (16 total channels), Glassman Highvoltage powersupply (up to 35 kV), high voltage signal generator, two relay switches, three DG535 signal delay generators, two linked computers. I then linked all of the components to fully automate the firing and data collection through a custom java program that integrates control and communication programs such as: IEEE Signal Express to get data from scopes, in-house custom HP oscilloscope data collection software, as well as a custom XP printer port 5V TTL triggering program.

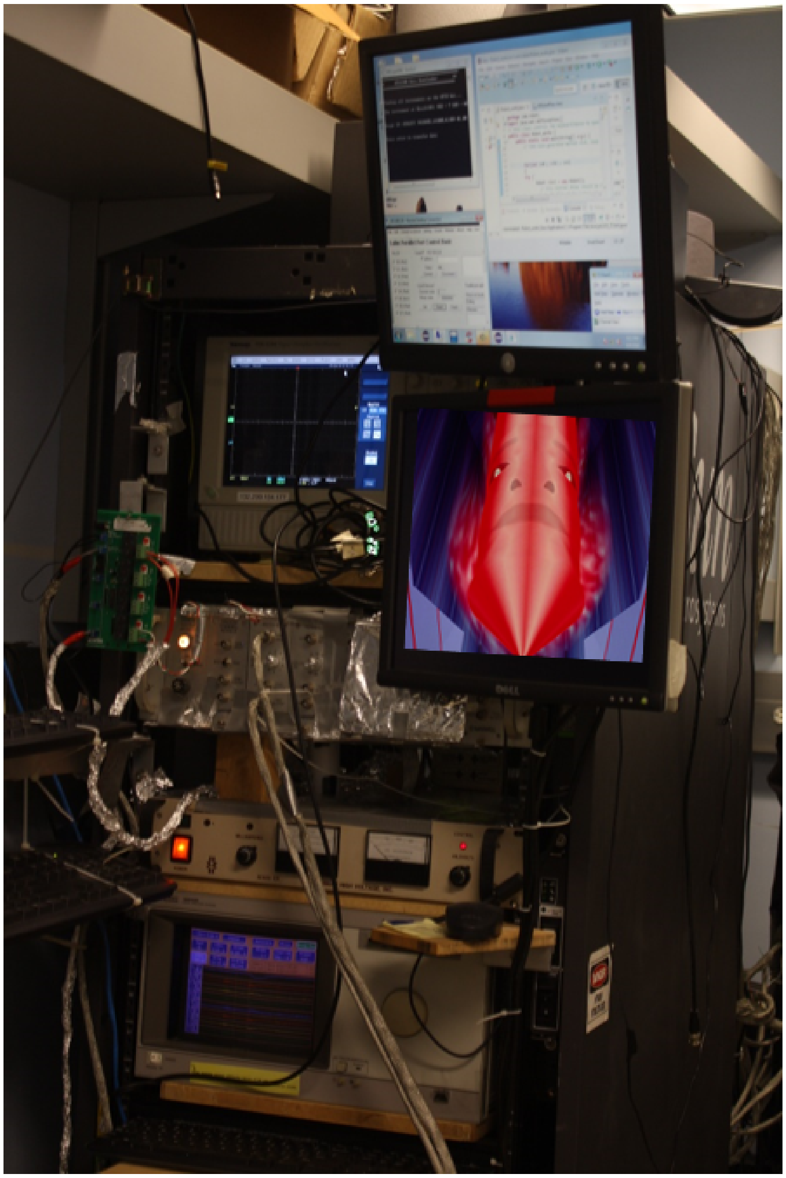

Figure 2.8: Master Control Program (MCP) tower for automation

2.5 The Vacuum Chamber

2.6 Electrode Geometry and Design

With many pulsed power systems using a coaxial vacuum gap such as transmission lines, and large pulsed power machines, we designed a very simple coaxial gap for ease of access and diagnosing of the vacuum gap.

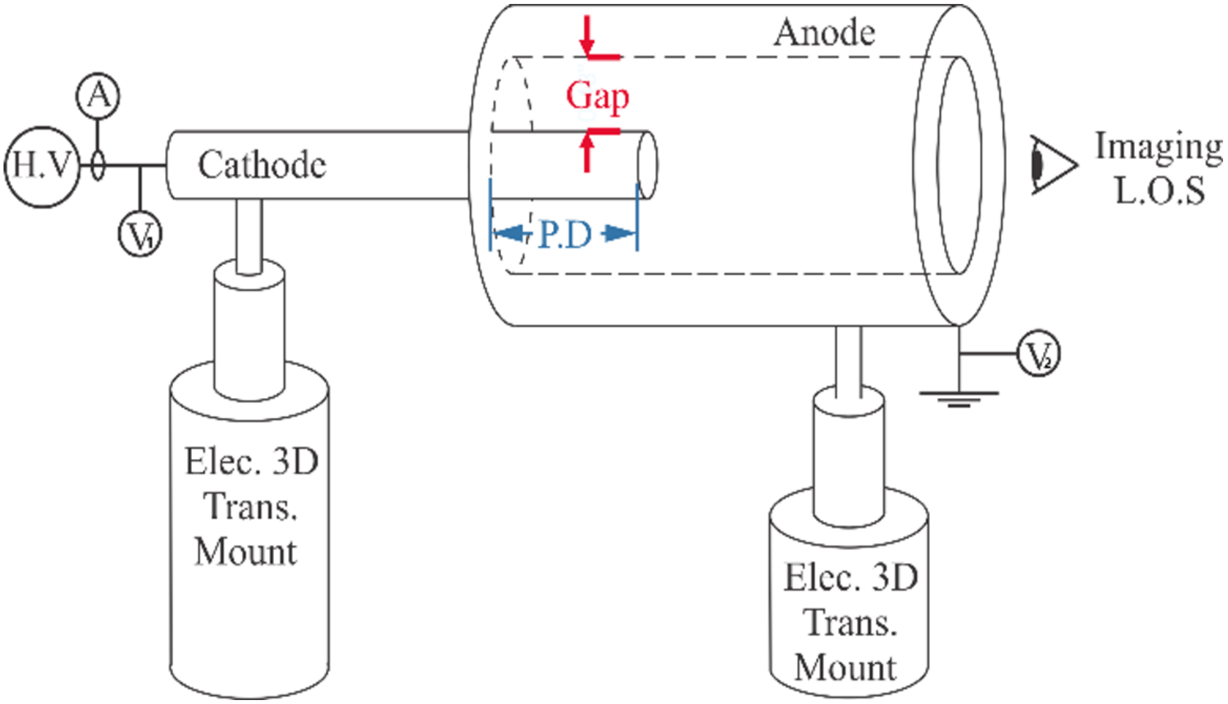

Figure 2.9: Diagram of electrode geometry of the CGB machine. Electrodes are 46 mm in length and vary in radius to form the gap as labeled in red. Blue is the penetration depth (P.D) which varies from 1.5 mm to 8.5 mm. The electrodes are monitored by current (A) and voltage (V_1 & V_2) probes and mounted on electrical 3D translational mounts. Time gated optical imaging is along the imaging line of sight as denoted by the eye.

For this reason the Coaxial Gap Breakdown (CGB) machine, consists of two aluminium alloy (5056) electrodes; a hollow cylinder of fixed inner diameter (18.5mm) with an inserted solid cylinder. Both are attached to electrical 3-D translational mounts to ensure the electrodes are parallel to one another, and to control their relative positions (Figure 2.9). This coupled with electrical continuity testing after alignment and breakdown position distribution calculations ensures that electrodes are centered with a defined gap. It is important to note, that the 3-D translational mounts allow for alignment under vacuum. Electrodes can be readily machined to create any azimuthal gap required in the coaxial geometry, 25 μm to several millimeters and penetration depths of the central conductor into the hollow (outer) electrode from 1.5 mm to 8.5 mm. The typical surface roughness of the in-house machined anode and cathodes (Figure 4.16)

2.7 Diagnostics

The CGB Machine (Figure 2.10) is monitored electrically by Pearson coil (model 6585, 1.5 ns rise time), and by a pair of high voltage probes (Pintek-HVP-39pro, 1.6 ns rise time,V_1 & V_2) located at the high voltage and ground sides of the electrodes (Figure 2.9). Optically, the gap is monitored via time integrated digital SLR camera (DSLR) that takes an image of the coaxial gap (20 μm – spatial resolution) along the imaging line of sight for each shot. In addition, the current density is monitored by an array of magnetic field probes.

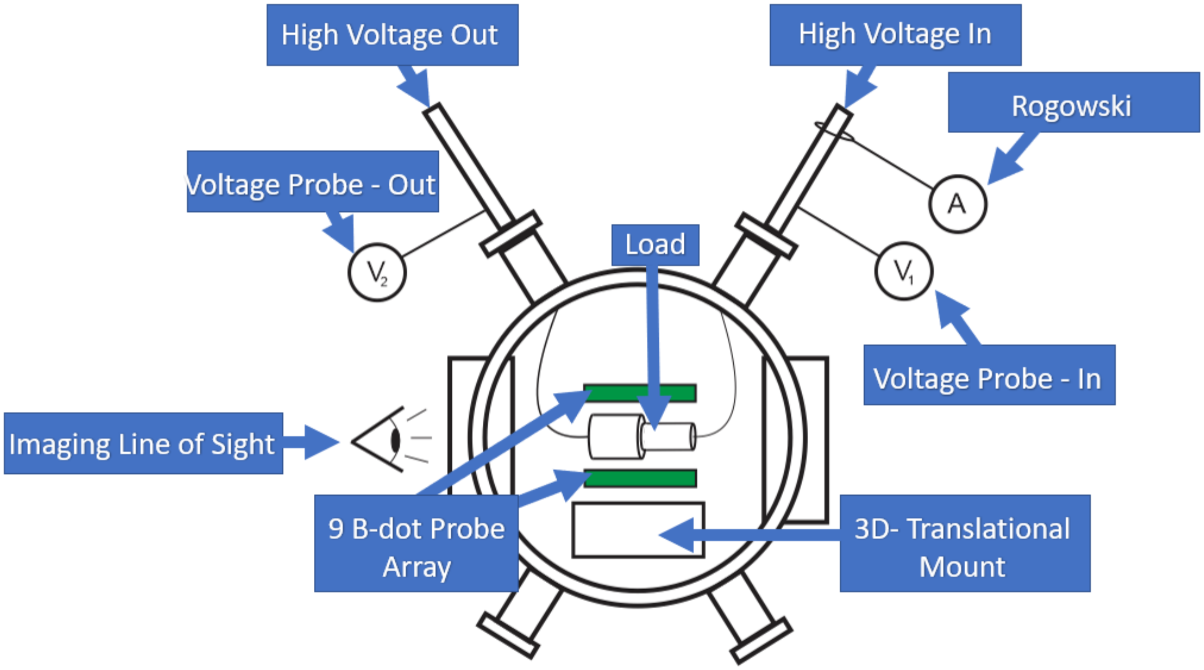

Figure 2.10: Top down drawing of the CGB Machine with diagnostics labeled.

2.7.1 Determining The Electrode Alignment

With the recovered time integrated optical imaging, we can determine the location of breakdowns that occur in each shot and at each penetration depth. This is done by converting the image of the coaxial gap (Figure 2.11a) to grey scale and performing a circular lineout (Figure 2.11b). The highest intensity peaks of the lineout correspond to a breakdown and its location about the azimuth (Figure 2.11c). Overlapping this information for 50 shots at a given penetration depth shows the azimuthal distribution of breakdown over the circumference of the vacuum gap. A spread in azimuthal distribution correlates to electrodes that are centered, and a gap that is well defined and uniform. Alternatively, if the distribution is clustered in a single spot or quadrant in the degree range the electrodes are not centered, and the gap is not well defined. This is of particular interest for the smaller gap sizes where ensuring a centered, defined gap can be challenging.

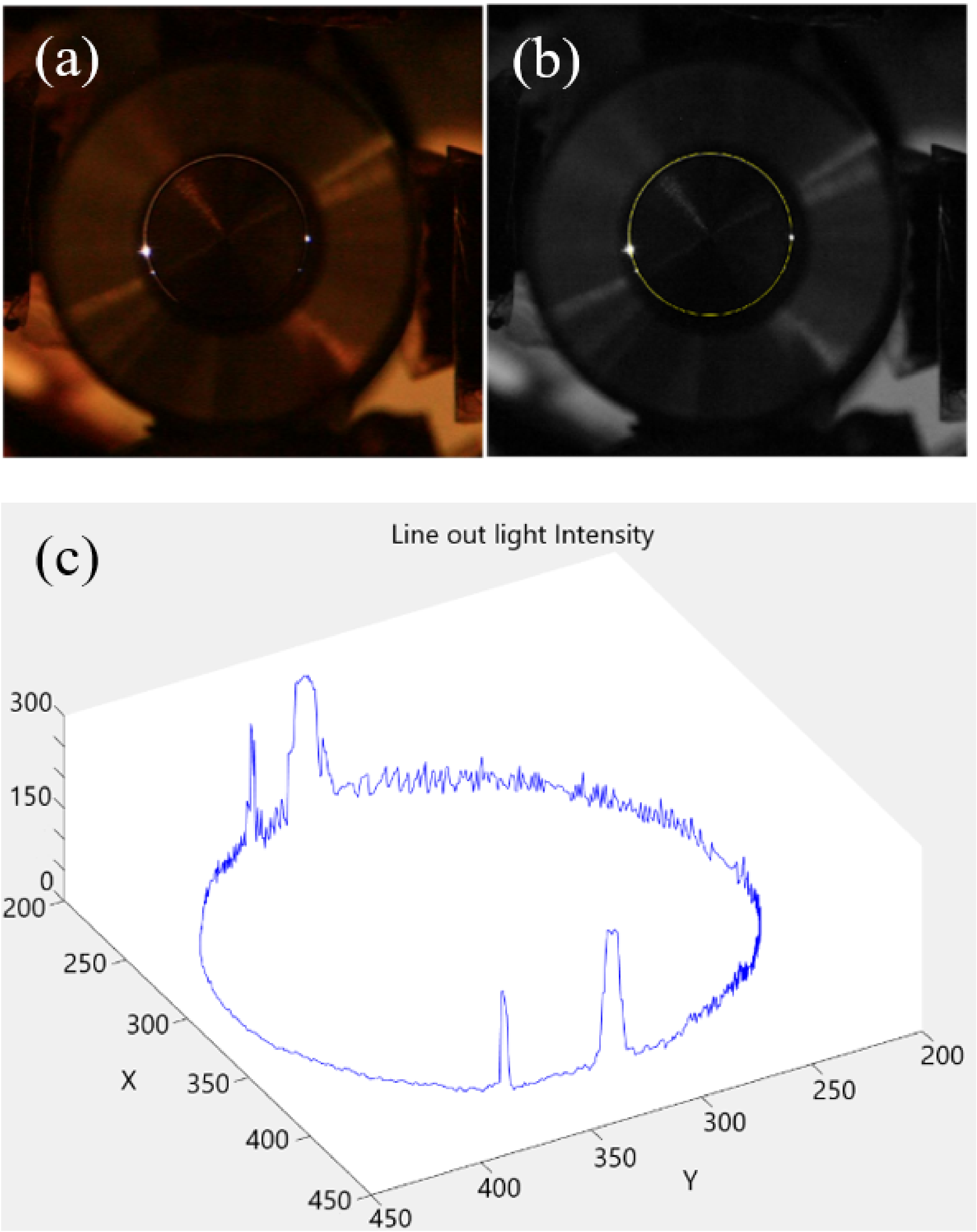

Figure 2.11: 150 μm gap, pd-8.5mm, (a) unaltered coaxial time integrated image of a single shot. (b) Grey-scaled version of (a) with a yellow circular lineout across the gap. (c) The intensity peaks and location of the breakdowns about the azimuth.

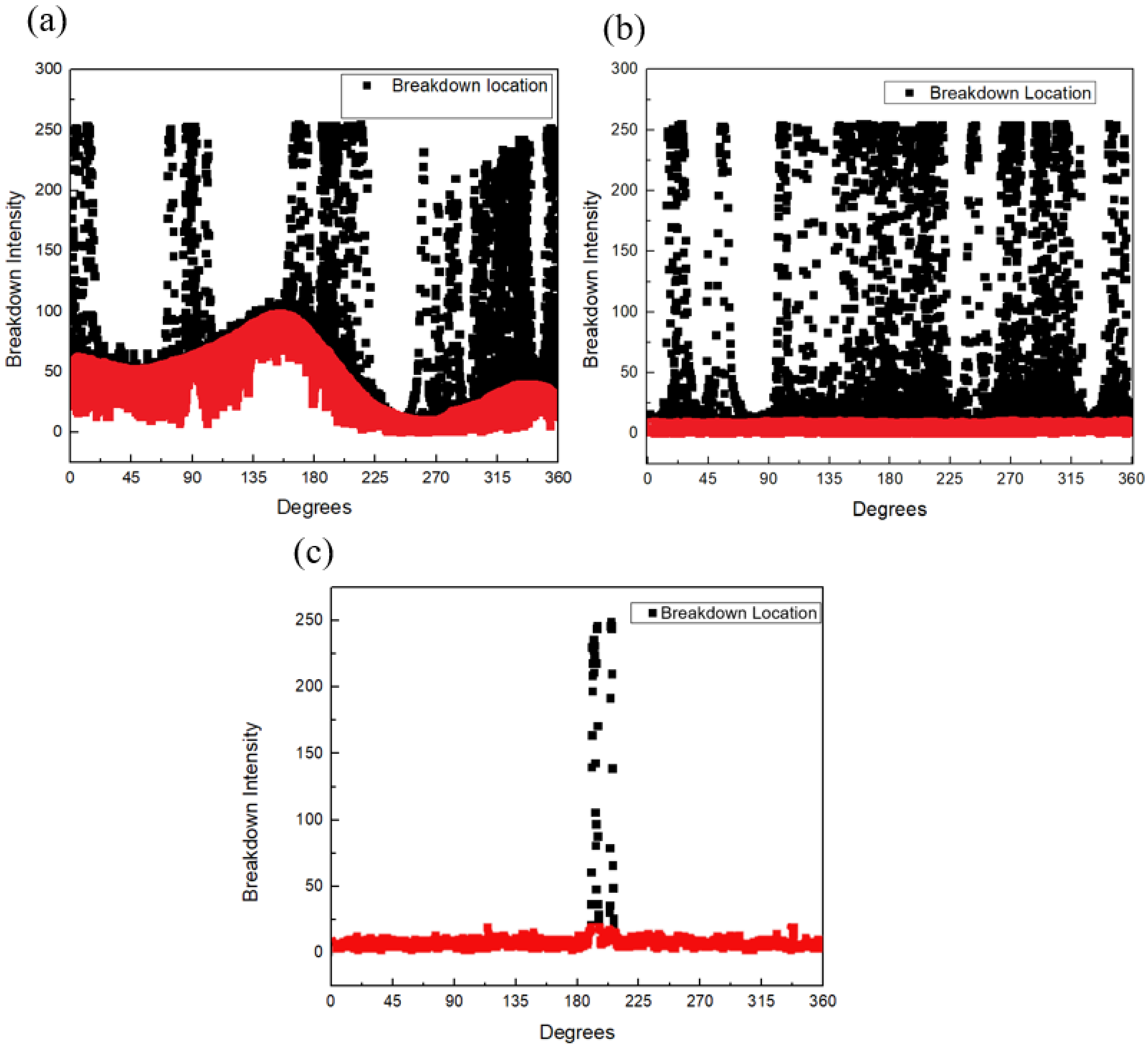

Figure 2.12: Breakdown intensity peak locations in degrees for (a) 100 μm gap, P.D-8.5 mm, 50 shots, (b) 50 μm gap, P.D-3.34 mm, 50 shots, and (c) 150 μm gap, P.D-8.5mm (Electrode offset from centered position by 70 μm 180°position). Red highlighted data are background light and are present in every shot. Black data are peak intensity values that each represent an individual breakdown location about the azimuth

Figures 2.12a,b show the azimuthal distribution for 50 shots at 100 μm at a penetration depth of 8.5 mm, and 50 μm at a penetration depth of 3.34 mm. The data are spread across all quadrants of the gap with small regions having no breakdowns, i.e. no preferred direction of breakdown indicating that the electrodes here are centered and well defined. Figure 2.12c shows an azimuthal distribution for a 150 μm gap at a penetration depth of 8.5mm (50 shots). The data are centered between 195°and 204°with no spread into the other quadrants of the gap, indicating that the cathode is offset in the anode. This qualitative method is used every shot series to ensure the data collected is from electrodes that are centered with a defined uniform gap.

2.7.2 Magnetic Field Probes

Throughout this document I will make reference to B-dots, this is the time rate of change of the magnetic field, dB/dt or $\dot{B}$ hence B-dot. A B-dot probe measures the time rate of change of the magnetic field that fluxes through the area of the probe, this induces a voltage in the probe as determined by Faraday's law, with the sign determined by Lenz's law. Or simply

$$\nabla \times E = -\frac{\partial B}{\partial t} \tag{2.1}$$

$$\oint E \cdot dl = -\frac{\partial}{\partial t} \int B \cdot dA \tag{2.2}$$

$$with, \frac{\partial A}{\partial t} = 0 \mapsto V = A\frac{\mathrm{d}B}{\mathrm{d}t} \tag{2.3}$$

where E is the electric field, B is the average magnetic field through the loop area A, t is time, dl is the loop segment length, and V the induced voltage in the probe. Figure 2.13 shows a cartoon of a probe in a magnetic field with fluxing B-field through the area, the orange portion is a solid coaxial cable and the loops (black) are made from the inner conductor. Only the dB/dt component normal to the loop will induce a voltage, therefore loop orientation within the changing field is important for good measurements, i.e if the probe in the cartoon were rotated 90°about its axis the field would no longer flux through the loop and no field would be measured. In the experiments presented probe loop orientation is held fixed through the use of optics mounting brackets.

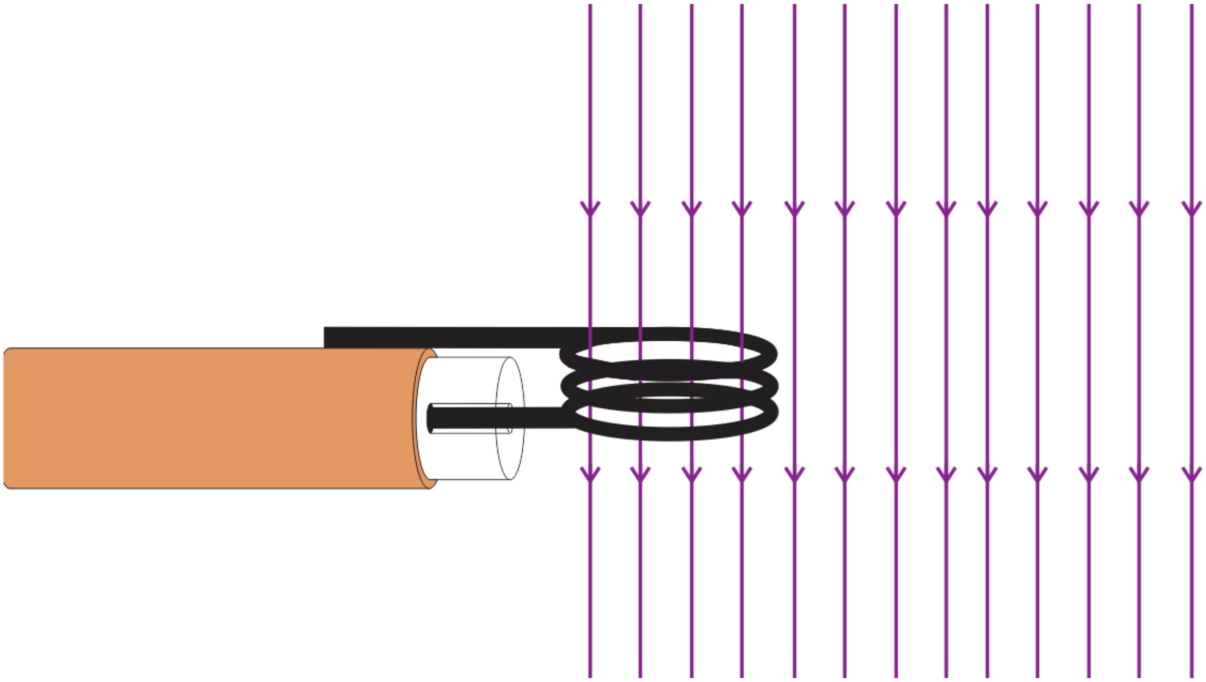

Figure 2.13: Magnetic Field probe with three loops placed in magnetic field.

Magnetic field probes are made in house using semi-rigid coaxial cable (rg405/u). The cable is cut to the dimensions in Figure 2.13. The inner wire of the coaxial cable is wrapped in a kapton tape layer to ensure that each loop does not touch and prevent any breakdown between them. The area of each loop is made in the same fashion by wrapping the loops around an uncut straight semi-rigid coaxial cable of diameter 3.56 mm. The number of loops on each probe is determined by the operating conditions of the experiment. In this case, it was determined that for the Coaxial Gap Breakdown machine (220 A, 25 kV, 130 ns) a three loop probe at a radial distance of 2-4 mm was the optimal setup. Furthermore, it is important that the connection of the loop to the outer shielding of the coaxial cable is sound as this reduces noise of the measured magnetic field signal. Probes used in the megaampere experiments described later in this document are an order of magnitude smaller in loop area and coaxial wire diameter as the fields measured for those experiment range from 1-20 Tesla, and are calibrated on the UCSD B-dot pulser (see Appendix B).

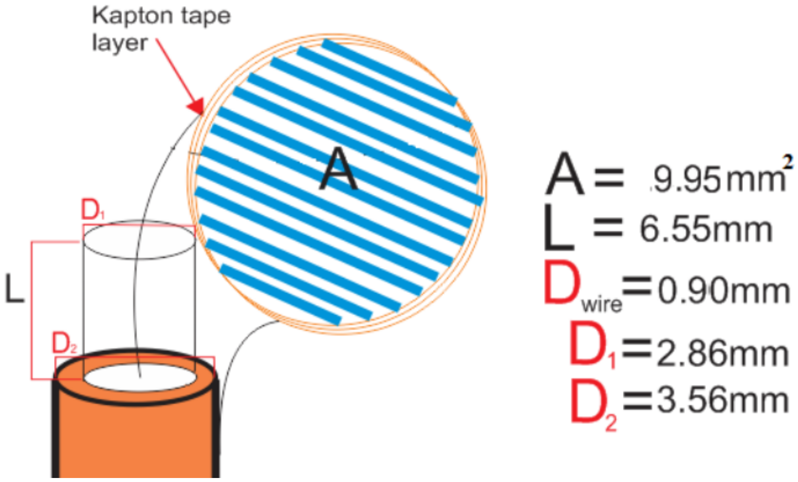

Figure 2.14: CGB machine B-dot probe dimensions

The CGB B-dots are calibrated through direct area measurement of the coils on each probe, with final sensitivity of each probe determined by a short circuit shot on the CGB machine in which the machine is fired into a solid aluminium rod. Starting with a known short circuit current pulse and a known location of the B-dot probes with respect to the center of the electrode setup before the shot, we can then calculate the expected magnetic field signal for each probe. Comparing the expected to measured signals (Figure 2.15) we find that, generally, the measured signals match closely with both the short circuit trace and the expected signals. Upon inspection, we find that the percent difference away from expected values of each probe is less than five percent. This percent difference is then added to the calculated calibration factor of each probe to ensure a complete and accurate calibration for all probes in question. Furthermore since the B-dot probes follow the current pulse so closely the response time is similar to that of the current monitor 1.5 ns. Finally, through the use of magnetic field probes we can monitor the current distribution in the load in space and time, this is discussed in full in Chapter 4.

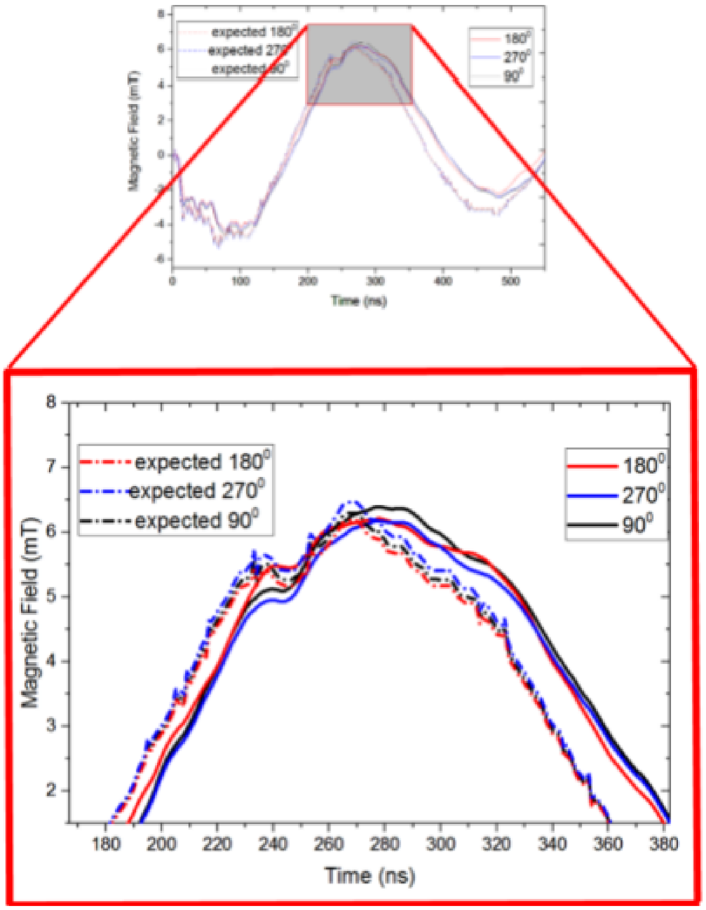

Figure 2.15: Typical measured short circuit current and magnetic field calibration signals.

2.7.3 Rogowski

The CGB machine current is monitored via Pearson Coil (model 6585, 1.5 ns rise time), this is just a mass produced Rogowski coil. A Rogowski coil is a helically wound wire, that is essentially a many turn B-dot probe, that is placed outside of and around the high voltage line in to the load. Figure shows a cartoon schematic of a Rogoswki coil taken from Luque Alfredo [66].

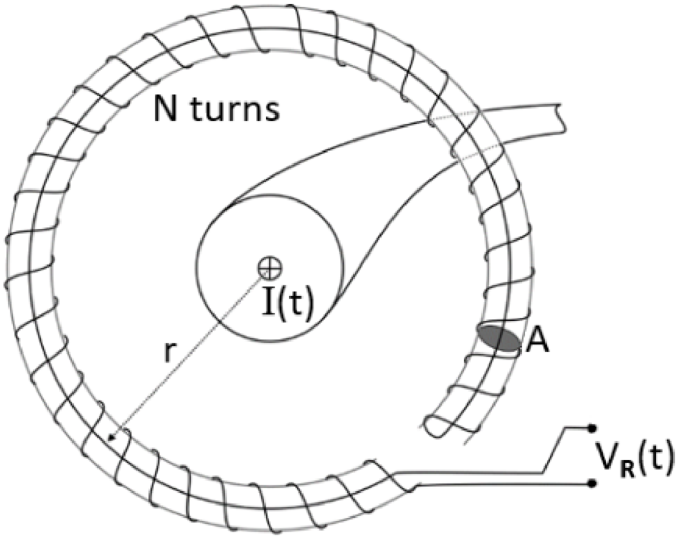

Figure 2.16: Diagram of Rogowski coil

The Rogowski coil voltage is given by,

$$V_R(t) = \frac{\mathrm{d}I}{\mathrm{d}t}\frac{\mu_0 NA}{2\pi r} \tag{2.4}$$

with I being the current in the load, μ_0 is the permeability of free space, N is the number turns in the coil, A is the area of each loop, r is the tadius from the center of current to coil. It is important to note that the total current measured is independent of the distribution of the current inside the major radius of the coil.

2.7.4 Voltage Probe

The vacuum gap is monitored by two Pintek-HVP-39pro voltage probes placed on high voltage lines before and after the load. This is a high voltage 1000:1 probe, filled with inert gas to protect the inner parts. The probe has a rise time of 1.6 ns, an impedance of 900 megaohm. These probes allow us to measure the voltage before and after breakdown of the vacuum gap. This is of great importance in the Fowler-Nordheim analysis. Typical voltage signals for the CGB machine are shown in Figure 2.3.

2.8 COBRA Pulser

Many of the experiments that are presented in this thesis were performed at the Laboratory of Plasma Studies at Cornell University, on their in-house pulser power generator the Cornell Beam Research Accelerator (COBRA)[33]. COBRA delivers a 1 MA peak current in 100 ns zero-to-peak rise time or a long pulse about 200 ns (Figure 2.17). This is achieved by the use of pulse compression from two Marx capacitor banks that are connected to a set of intermediate storage capacitors. The storage capacitors connect to main switches which connect to four coaxial transmission pulse forming lines. The pulse forming lines connect to four output switches that connect to a triplate transmission line into a coaxial magnetically insulated transmission line (MITL), and then to the load chamber. Figure 2.18 shows a design drawing of the COBRA pulser with main components labeled and to relative scale. For an in depth machine explanation I direct the reader to the machine paper by John Greenly [33] or any of the theses out of the Laboratory of Plasma Studies at Cornell University since 2008.

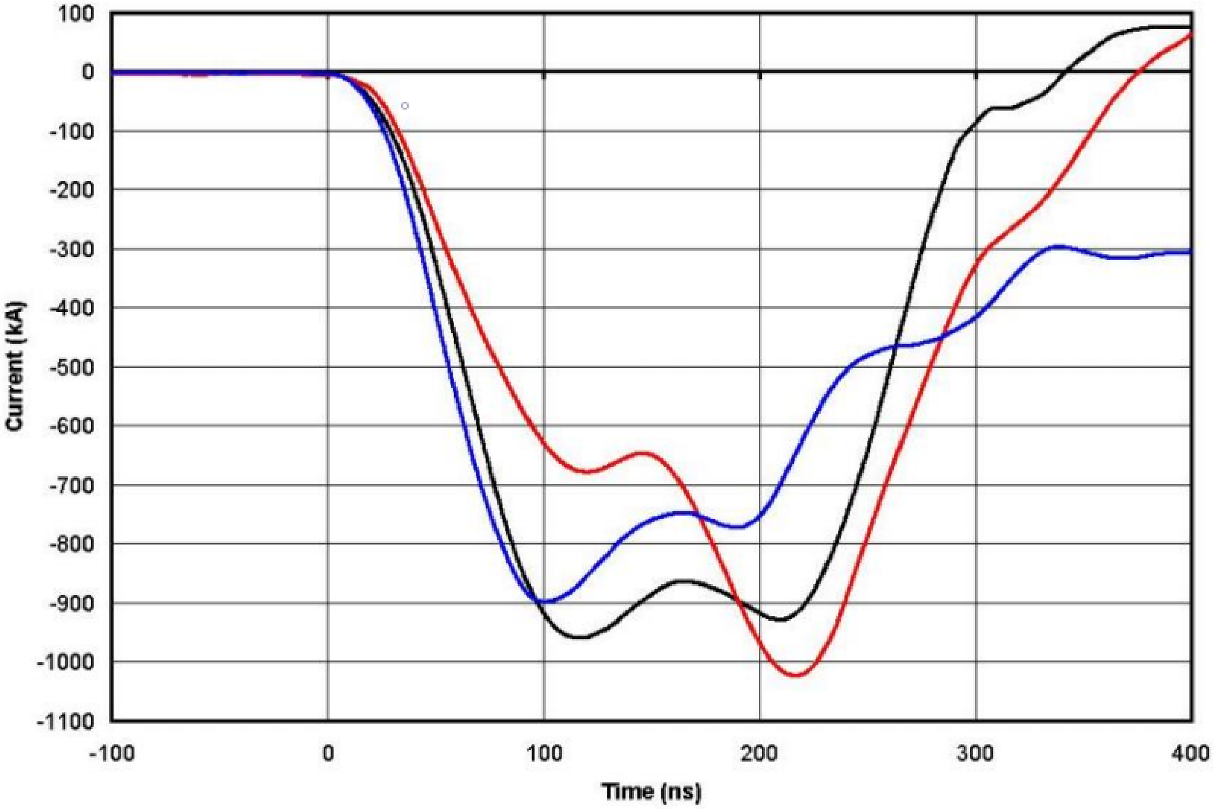

Figure 2.17: Typical operating current COBRA, short pulse labeled in blue and black, long rise pulse in red.

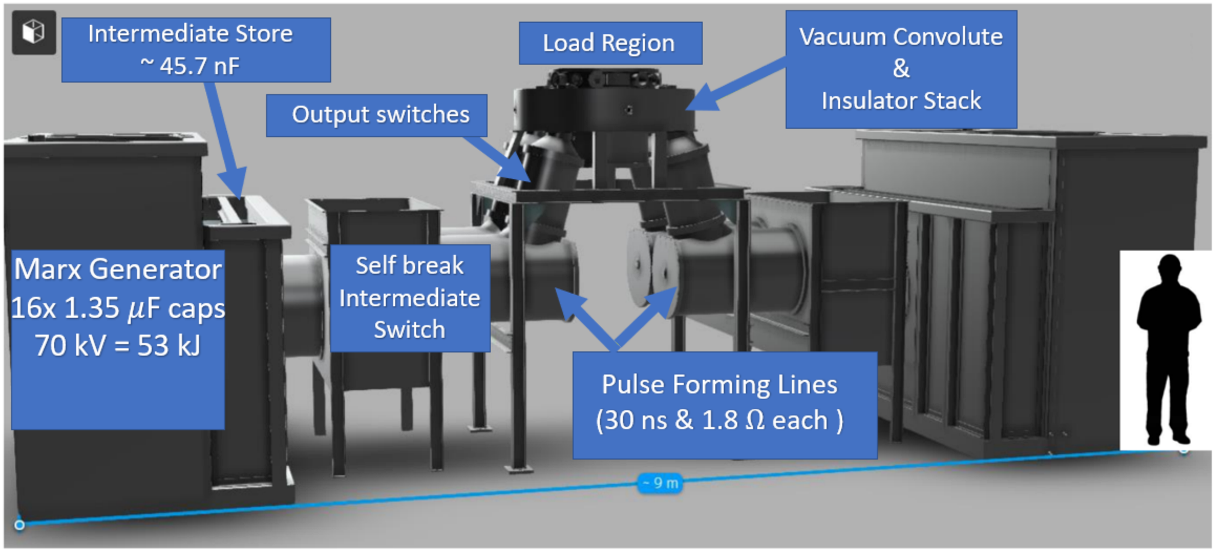

Figure 2.18: COBRA Design diagram with components labeled and human for scale.

2.8.1 12 Frame Camera

On COBRA we are able to image plasma self emission in the optical range ($\sim$1-3 eV) using a high speed multiframe ICCD (Invisible Vision Ultra UHSi 12/24). The camera is able to set an exposure limit of as low as 5 ns, with time between sequential frames 5 ns. The camera can also fire up to 12 frames in sequence per experimental shot, this allows us to image plasma emission for potentially the entire current rise (zero to peak). The camera works by splitting incoming optical emission into 12 independent Microchannel plate (MCP) detectors. In addition, the MCPs are not accurately cross-calibrated, so absolute emission measurements between frames is not possible. For the experiments presented in this document the diagnostic is set to view the vacuum gap from the top down, to image breakdown formation as the current rises, and set to 10 ns steps, a typical camera set up is shown in Figure 2.19.

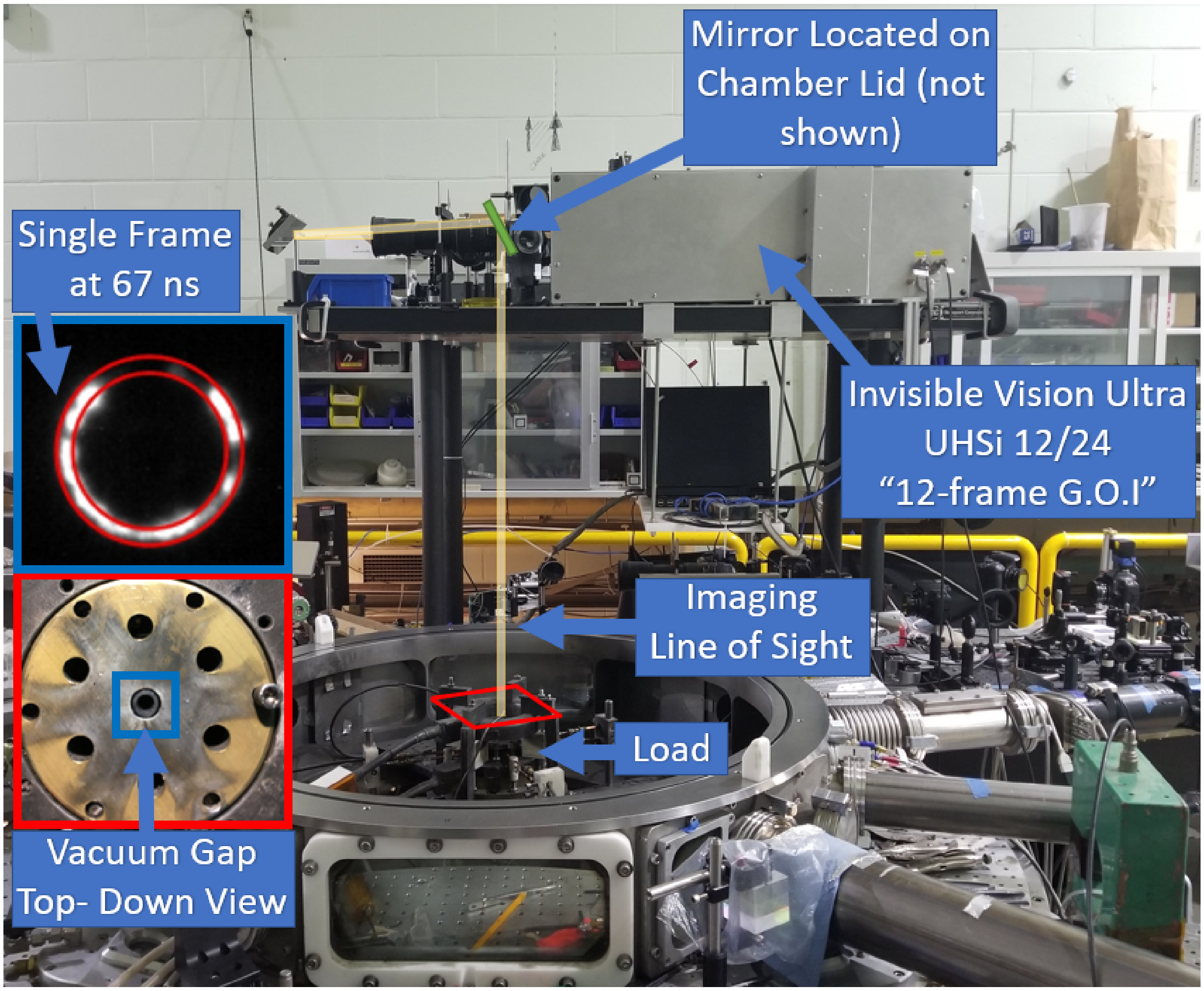

Figure 2.19: COBRA chamber with optical line of sight shown for 12-frame gated optical imaging camera, red square shows the top-down view of the vacuum gap with a single frame at 67 ns shown in blue.

2.8.2 Helmholtz Pair

On COBRA a Helmholtz coil is pulsed independently from the main current drive, and provides a uniform axial magnetic field from 0 to $\sim$2 Tesla just over the load region over the experimental timescale (300 ns). The coil has a rise time of 140-150 μs, and long rise time allows the field to penetrate through thin hardware in the experiment. Eddy currents generated in the load hardware prevent full penetration, this can be alleviated by either increasing the coil rise time or putting slots in the solid return structures to allow the field to penetrate (see chapter 4 external b-field experiments). Figure 2.20 shows the Helmholtz pair used in experiments presented in this document.

Figure 2.20: Experimental setup for Helmholtz coil pair

The Cornell Helmholtz pair consists of two circular solenoids oriented along the same axis as shown in the above image. A Coil pair is used to allow diagnostic access along the radial and axial view. The distance between the pairs equals the radius of the pair loops. When a current flows in the same direction in the top and bottom pair, the magnetic field at the midpoint is given by,

$$B = \frac{8}{5\sqrt{5}} \frac{\mu_0 N I}{a} \tag{2.5}$$

where μ_0 is the permeability of free space, N is the number of turns in the coils in each pair, I is the current through the coils, a is the radius of the pairs ($\sim$0.06 m). This generated magnetic field is uniform [71] between center of the pair and fringing outside of it, this can be seen in Figure 2.21 that shows a cartoon image of the uniform magnetic field overlaid atop the Helmholtz pair. If the magnetic field deviated significantly from results would be hard to interpret as the magnetic field would now have additional component values. More information about the construction and design parameters of the Cornell Helmholtz pair can be found in T.Byvank 2018 [18]

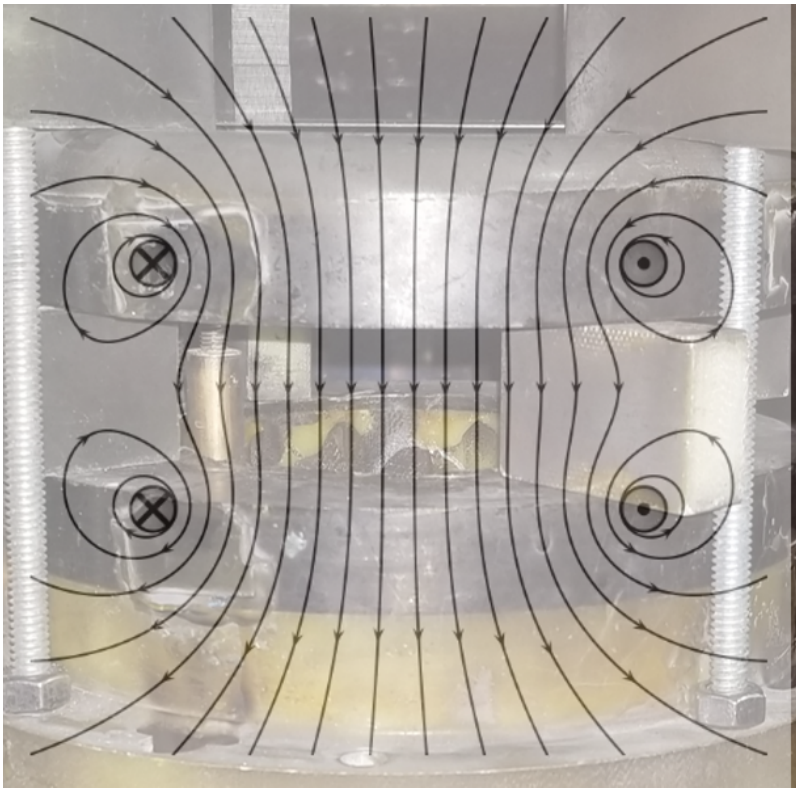

.

Figure 2.21: Experimental setup for Helmholtz coil with a cartoon of the produced magnetic field flux cross section overlaid

Chapter 3

Breakdown Physics Theory

”Don’t do what you can’t undo, until you’ve considered what you can’t do once you’ve done it.” - The Fool.

3.1 General Breakdown Physics

The physics of breakdown has been studied for over 100 years and many of the processes are well understood and documented [36][48][60][47][1], though there are still many unanswered questions on the behaviors driving observations. As diagnostics get better these questions begin to be answered. In general, Breakdown is described by Field Emission, Thermionic Emission or a combination of the two. This chapter will focus on existing Breakdown theory to have an analytical framework to better understand the results discussed in Chapter 4.

3.2 Field Emission

Field emission [28][73][26] occurs when electrons are drawn out of a metal surface by a high electrostatic field. At the surface of a metal electrode, a strong electric field can modify the potential barrier at the surface to such a level that electrons in an upper level close to the

Fermi level will have a probability of passing through the vacuum barrier. This is known as tunneling, and is experimentally seen as a breakdown. In order to achieve tunneling the electric field required needs to be on the order of $\sim 10^7$ V/cm. These large fields are often seen at the points of surface imperfections on the surface of the electrode. Physically a breakdown occurs when the electric field on the surface of a material drives a small current on the surface of the cathode, this causes electrons to release which stream into the gap (tunneling), after a time the region in the gap becomes ionized and the voltage drops leading to the formation of a plasma channel that carries a current that closes the gap.

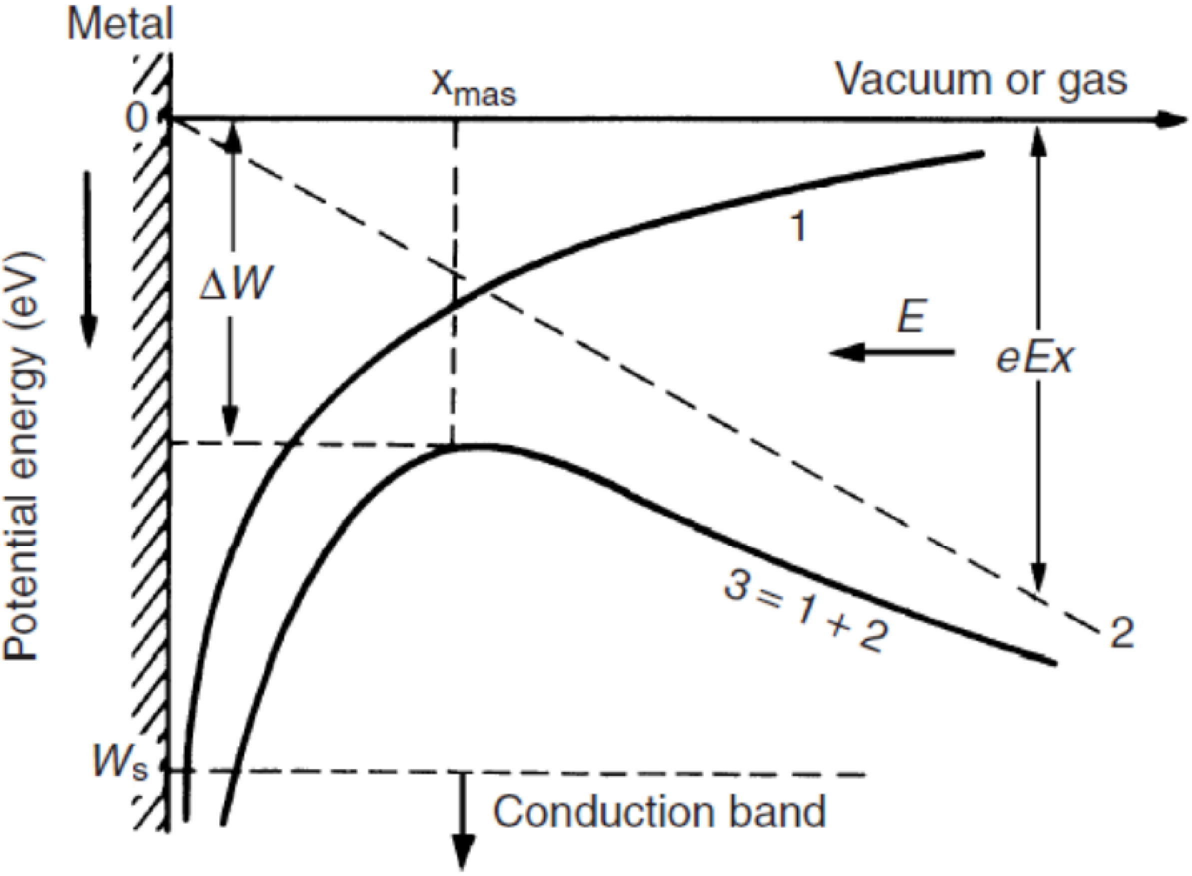

Figure 3.1: Breakdown emission diagram, which depicts the lowering of the potential barrier by an external electric field. The curve 1 represents the energy of the system without a field, curve 2 represents the energy due to the field, and curve 3 represents the total energy of the system in the presence of the external electric field (E). x_{max} is the distance at which the change in work done (ΔW) is zero.

The breakdown emission current can be derived if we consider a simple analytical model of an electron moving from the metal electrode surface in the $+x$ direction (Figure 3.1). The electric field can be approximated as a point charge and an equipotential planar surface (denoted as the metal surface). If we follow convention we can see field lines are the same as those when a test charge(+q) exists at a distance of -x on the oppose side of the metal surface. Using Coulomb's Law,

$$F(x) = -\frac{e^2}{4\pi\varepsilon_0(2x)^2} \tag{3.1}$$

thus the potential energy at any distance x is found as,

$$W_{e1} = \int_{\infty}^{x} F(x)dx = -\frac{e^2}{16\pi\varepsilon_0 x} \tag{3.2}$$

Equation 3.2 is plotted on Figure 3.1 as a curve one. If the external field is applied at right angles to the metal surface, the potential energy given to the electron,

$$W_E = -eE_x \tag{3.3}$$

Equation 3.3 is plotted on Figure 3.1 and is shown as a straight line (curve 2). From this we can then find the total energy of the system W_T;

$$W_T = W_{e1} + W_E \tag{3.4}$$

Equation 3.4 is the total energy of the system and is graphed on Figure 3.1 as the resultant curve of W_E and W_{e1} (curve 3). This change in energy results in a reduction of the barrier. We can then find the value at which W_T is maximized by determining where the change in work done is zero (turning point curve 3),

$$\frac{\mathrm{d}W_T}{\mathrm{d}x} = \frac{e^2}{16\pi\varepsilon_0 x_{max}^2} - eE = 0$$

$$x_{max} = \sqrt{\frac{e}{16\pi\varepsilon_0 E}}$$

$$W_T(x_{max}) = -e\sqrt{\frac{eE}{4\pi\varepsilon_0}}$$

From this we can find that the effective work function is,

$$\begin{gathered} W_{eff} = W_s - W_T(x_{max}) \\ W_s : Work\ function \end{gathered} \tag{3.5}$$

At this point we can then determine the emission current density based on the effective work function Equation 3.5. This current density is related to the temperature of the emitter by the Richardson relation [67] for themionically emitted current,

$$J_s = \frac{4\pi mek^2}{h^3} T^3 exp[-\frac{W_s}{kT}] \tag{3.6}$$

Where e is the electron charge, m is the mass of an electron, T is the absolute temperature.

In a general summary of the Thermionic Emission equation above; Heating a metal increases the energy of valence electrons within the metal, and electrons with sufficient energy have a probability of escaping the surface of the metal. A positively charged anode can be placed at some distance away x to draw away escaped electrons. For sufficiently large electric field (10^8V/m) between the cathode and anode, the emission current can be considered independent of voltage and scales with temperature only.

With this we are able to combine our effective work function equation and the current density equation above for a modified current density due to electron emission,

$$J_s = \frac{4\pi mek^2}{h^3} T^3 exp[-\frac{e}{kT}(W_s - \sqrt{\frac{eE}{4\pi\varepsilon_0}})] \tag{3.7}$$

The above equation is dependent mainly on the temperature of the electrode, electric field, and the work function of the metal. This is known as the Schottky's equation [70].

3.3 Cold Field Approximation

For the experimental regime of the CGB machine the temperature of our electrodes is considered room temperature, due to our short current pulse (150 ns) and our current and voltage is relatively low (240 Amperes, 25 kilovolts). Thus, an emission current density equation that is based on the temperature of the electrode is not ideal. To address this we turned to the Cold Field approximation.

This theory was first derived in 1928 by Folwer and Nordheim, and it relates the electric field, the work function of the metal and the current density of the emitted electrons for a low temperature metal ($\sim$0 K) [30] . The derivation of which was closely related to work being done simultaneously by Oppenheimer [61] on the emission of electrons from the hydrogen atom influenced by a high external electric field.

Consider the emission through a potential barrier, electrons will attempt to tunnel through the potential barrier shown in Figure 3.2. The dotted line is the assumed step function version of the potential energy of the electrons, with the curved line denoting a rounding of the potential energy at sharp points due to the mirror image potential effect. Below this rounding of the potential, which alters the emission coefficients for any non-zero external electric field whose incident energy is about equal to the kinetic energy of the electron motion normal to the emitter surface, is insignificant in a strong field emission at room temperature.

This is done by solving the wave equation through a potential energy step which is denoted as a dotted line in Figure 3.2

Figure 3.2: Potential Barrier example.

$$\frac{\partial^2\psi}{\partial x^2} + k^2(W - C + Fx)\psi = 0, x > 0 \tag{3.8}$$

$$\frac{\partial^2\psi}{\partial x^2} + k^2 W\psi = 0, x < 0 \tag{3.9}$$

where $k^2 = 8\pi^2 m/h^2$. And the above equations are under the following conditions; (1): ψ and $\frac{\partial\psi}{\partial x}$ are continuous at x = 0. (2): X>0 stream of electrons to the right only.

At low temperatures, nearly all electrons are distributed such that W < C such that we pass through a zero of the coefficient of ψ. With W being the energy incident to the left on a surface, and C is the increase in potential energy. We can then substitute the following into our wave equation,

$$(-\frac{C-W}{F} + x)(k^2F)^{1/2} = y$$

$$\Rightarrow \frac{\partial^2\psi}{\partial x^2} + y\psi = 0$$

This is just the basic wave equation which has solutions in terms of Bessel functions (O 1/3) [72],

$$\psi = \sqrt{y}J_{\pm 1/3}(\frac{2}{3}y^{\frac{8}{2}}) \tag{3.10}$$

After much work solving the above equation leads us to,

$$I = \frac{\varepsilon}{2\pi h}\frac{\mu^{\frac{1}{2}}}{(\chi + \mu)\chi^{\frac{1}{2}}}F^2 e^{-\frac{4\kappa\chi^{\frac{3}{2}}}{3F}} \tag{3.11}$$

With $\chi = C - \mu$, where χ is the thermionic work function [30] that corresponds to the metal surface properties. The equation above can be rearranged in terms of current density J, by dividing the current by the emitting surface area A/cm^2, the work function in terms of electron volts, F in terms of V/cm. Thus,

$$J = 6.2 \times 10^{-6} \frac{\mu^{\frac{1}{2}}}{(\chi + \mu)\chi^{\frac{1}{2}}} F^2 e^{-\frac{6.8\times10^7\chi^{\frac{3}{2}}}{F}} \tag{3.12}$$

Historical experimental results [29] suggest electron emission and external field is accounted for in equation 3.22. We can further rearrange equation 3.12 into a more readily used form [27]

$$J = a\phi^{-1}E^2 P_F \exp\left(-\frac{b\phi^{\frac{3}{2}}}{E}\right) \tag{3.13}$$

$$P_F = \frac{4\phi^{\frac{1}{2}}\mu^{\frac{1}{2}}}{\phi + \mu}$$

$$a \sim 1.54 \times 10^{-6} \mathrm{AeV} V^{-2}$$

$$b \sim 6.83 \mathrm{eV}^{-\frac{3}{2}} \mathrm{Vnm}^{-1}$$

Where ϕ is the work function and E is the electric field, and P_F is known as the tunneling factor. The tunneling factor is usually of order unity and often ignored.

The following is a consolidation of all assumptions made in the above derivation for easy reference later.

Assumptions:

1. The temperature of the emitting metal surface is taken to be 0K, such that no electrons with energies above the Fermi energy exist in the metal, and that the Fermi level will be the top most filled level with electrons. Its electronic charge distribution in the metal given by the Fermi-Dirac statistics.

2. Electron-Ion and Electron-Electron interactions are neglected. Known as the free electron

approximation.

3. The emitting surface is taken to be rather smooth, such that irregularities are small compared to the width of the potential barrier (i.e. the size of the gap). Quantum Mechanical Tunneling [70] [61] across the barrier occurs only if the uncertainty in the position, δx, of the electron is of order the barrier width i.e. $x = \phi/Ee$.
4. The potential barrier near the surface in the vacuum region consists of a potential due to the applied electric field, known as an image potential. This potential exerts an image force by the Coulomb attraction towards the surface of an electron outside, due to the induced charge inside of the metal.

Again, a general description of the Field emission is given here; Where thermionic emission relies on the electrons energy within the metal, in field emission an applied electric field reduces the effective work function to give a field emission current.

3.4 Fowler Nordheim Analysis

Equation 3.23 determines the total number of electrons that tunnel through the potential barrier at the surface per unit area, better known as emission current density. In order to use this analytical function experimentally, we again rearrange the terms slightly. We will return to our original convention of current rather than current density, and change our electric field strength coefficient to something that is measurable.

$$F = \beta V$$

$$I = JA$$

Where A is the emitting surface area, and β is the field enhancement factor and characterizes the surface roughness, V is the anode-cathode voltage. Substituting into equation 3.23,

$$I = a\phi^{-1}\beta^2 V^2 P_F \exp\left(-\frac{b\phi^{\frac{3}{2}}}{\beta V}\right) \tag{3.14}$$

taking the log of both sides and rearranging further,

$$log(\frac{I}{V^2}) = -\frac{2.9669x10^7\phi^{3/2}}{\beta V} + log(a\frac{\beta^2}{\phi})$$

a curve is obtained by plotting $log(I/V^2)$ versus $10000/V$ which typically yields a straight line, known as a Fowler-Nordheim (FN) plot. Taking the slope of this line give,

$$m = -\frac{2.9669x10^3\phi^{\frac{1}{2}}}{\beta} \tag{3.15}$$

The slope is now dependent only on the work function (known- NIST database), and the enhancement factor. This means that the enhancement factor and thus surface information can be calculated experimentally.

3.5 Explosive Electron Emission

It is widely accepted that breakdown is caused by field emission from microstructures on the surface of the cathode that are accompanied by explosive destruction of said structures [54], [55],[53] known as Explosive Electron Emission (EEE), the general idea will be outlined in this section.

The surface of any electrode is characterized by microstructures, known as microprotrusions. These generally appear after mechanical processing and come in many forms; inclusions or holes/bumps, oxide films, absorbed layers of vapors or gasses (sweat or anything on your hands), chemical impurities within the grains of the electrode material, or any foreign particle. From SEM images later presented in this document, the majority of imperfections on the electrode surface for experiments at UCSD and Cornell are those that are a result of the machining groves and cracks in the electrode. These are often simplified as sharp points. Once current is passed into the cathode, current density increases the temperature (ohmic heating) of the microprotrusion and the applied electric field of the gap at the protrusion tip (10^{7-8}V/m) sends electrons across the gap to strike the anode plate (which can in turn be heated and evaporate. Eventually the temperature of the protrusion rises to such a point that it melts and ionizes, creating one or more cathode spots. In principle, this reduces to the following relation,

$$j_{sp}^2 t_{ex} = C_{ex} \tag{3.16}$$

where j_{sp} is the current density through the spike and t_{ex} is the characteristic explosion time of the protrusion, and C_{ex} is an experimental constant that is generally 10^9 and explosions occur when the current density is about $10^9 A/cm^2$ which occurs on protrusions thanks to Field Enhancement Emission described above. With the time of explosions, t_{ex} on the order of $10^{-9} s$ [39].

A portion of the microprotrusion remains in the melt stage [50],[53] in a crater below the cathode spot. The cathode spot exerts a pressure on the liquid pool of material such that,

$$F = \frac{(M_i v)}{[2t_{cycle}(1-\alpha)]}$$

is the force acting on the liquid pool, with M being the Mass of the liquid material, t_{cycle} is the duration of the cathode spot, α is an experimental parameter determined by the radius of the crater, and v is the ion velocity ($\sim 10^6$ cm/s for aluminium)[3]. With this the pressure can be approximated as,

$$P = \frac{F}{\pi r^2}$$

where r is the radius of the blast crater. For low current (200-500 ampere) experiments [25] it has been shown the pressure exerted on the molten pool is $\sim 10^8$Pa, in addition the jet of material that results from the explosive emission has a velocity that was estimated from to be on the order of 10^4 cm/s

This pressure then explosively propels the molten material into the gap and across the cathode surface creating additional microprotrusions and leaving behind a crater in the cathode surface, the crater may have a height which varies either above or below the original cathode surface level [25], effectively becoming another microprotrusion. The cathode spot that remains will expand for a brief time, accelerating high energy ions towards the anode [46]. In addition a narrow electron jet forms, causing further cathode erosion [65] and the new spots form below the existing cathode spot aiding in its spread. As the spot spreads, local protrusions in the neighborhood of the spread begin to emit and form cathode spots (baring enough current and cathode material). The process occurs at all breakdown positions on the cathode, evidence of which can be imaged via SEM which will be shown and discussed in Chapter 4.

A very simple cartoon drawing of the EEE process has been included for the reader to keep in mind while results are being discussed in Chapter 4.

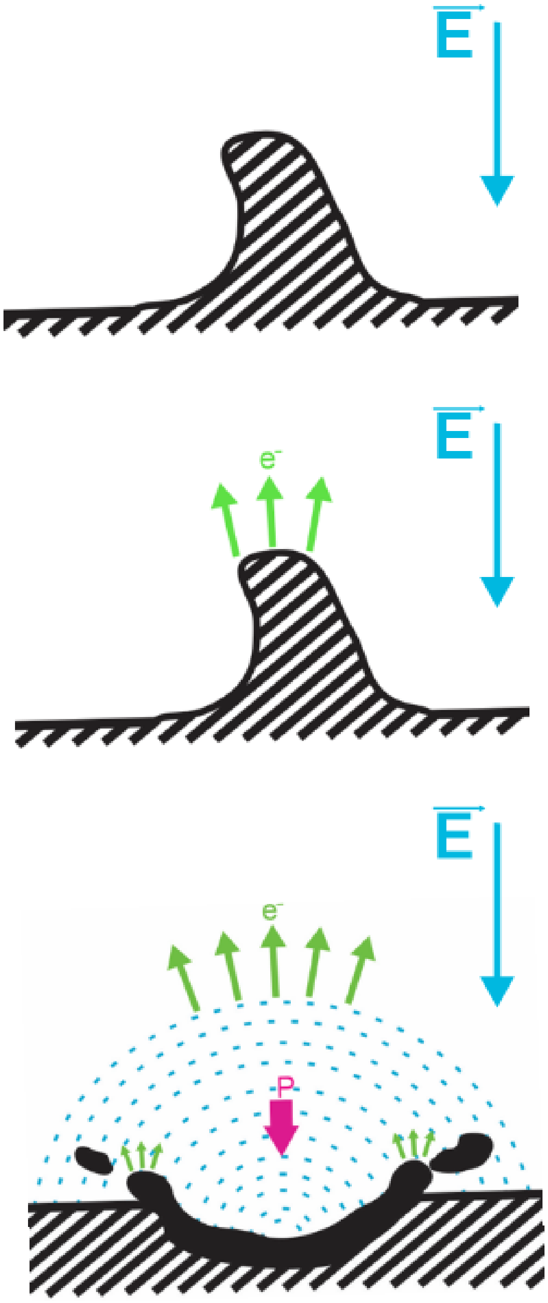

Figure 3.3: Explosive Electron Emission cartoon, from top down shows a microprotrusion that is heating up and releasing electrons, melts and explodes.

3.6 Breakdown Initiation From Surface Impacts Of Microparticles

It is possible to initiate breakdown by accelerating particle material with an electric field to a high energy and striking the surface of one of the electrodes [76] [21]. Experimental results suggest some minimum requirements on particle diameter, velocity, and impact energy for which values below breakdown will not occur due to impact. Various authors ([75], [10],[17] show that for aluminium, the minimum particle diameter is 0.3 - 5 μm, the minimum velocity 0.32 km/s, and minimum energy of $4x10^{-8}$J at 15 kV charge at the gap. These values of energy increase by 4 orders of magnitude and particle size increase 2 fold for anode breakdown initiation, but also decrease when the voltage at the gap is increased. The minimum energy is required so that when the particle strikes the surface of the electrode, a cloud of gas will be produced and subsequently ionized to form a cathode or anode spot, with the majority of the kinetic energy of the accelerating particle going into the heating of the particle and the target to melting/evaporating temperatures. In addition, if the velocities are sufficiently high ($5v_{min}$) the particle will deform the target on impact, forming a crater and subsequent microprotrusions that will heat up and undergo EEE. For velocities $> 5v_{min}$, both the particle and a portion of the surface will vaporize followed by plasma formation and EEE. This is an incredibly efficient form of initiating breakdown, as for instance V=25 kV, with a gap size of 2mm the minimum energy is 10^{-8}J for to strike the cathode and 10^{-4}j for the anode. These minimum values will be referenced in Chapter 4.

In a more general sense these particles, which could be electrode particles or impurities that are loosely attached to the electrode surface can be accelerated under the action of the voltage applied to the gap, or even as a result of explosive emission hitting the opposite electrode–heating and evaporating the particle, potentially deforming the surface, and thus initiating breakdown. In addition, as the particle approaches the opposite electrode, breakdown can be initiated by triggering a discharge between conductive particle and the opposite plate. Furthermore as particles are sent into the gap they can be ionized in the gap by field emission current (much like a trigger spark). The particle charge can be estimated with [42]

$$Q = \frac{2}{3}\pi_3 \varepsilon_0 r^2 E \tag{3.17}$$

The kinetic energy (Q_k)of the charged accelerated microparticles under the applied voltage in the vacuum gap can be estimated simply [23] as,

$$Q_k = mv^2/2 = qV \tag{3.18}$$

where v is the velocity of the microparticle at impact, m is the mass of the particle, q is the charge crossing the gap, with applied voltage V. If the particle has cross sectional area S, we can calculate the energy density,

$$Q_k/S = qV/S \tag{3.19}$$

where q/S is the charge density of the particle which is proportional to the electric field E. Thus,

$$W_k/S = CVE \tag{3.20}$$

where C is a constant and in the case of parallel plates $E = V/d$

With this we can have an upper estimate of the velocity of ejected particles across the vacuum gap that can initiate breakdown. This will be explored in Chapter 4 when talking about the coating electrode experiments on COBRA.

3.7 Expansion Velocity Of Plasma in a Vacuum Gap with an External Magnetic Field

3.7.1 Cathode Spot Plasma Jet

As we have described above, plasma is generated on the cathode surface by microprotrusion explosion, and vaporization of the cathode material. But this description is only useful in the initiation process and not the processes that occur immediately after.

After EEE initiation, a column of plasma is generated by the cathode spot and is accelerated across the gap towards the anode, this process is shown schematically in Figure 3.4. The cathode spot region is where the net of erosion of the cathode mass is formed [8] [19], as well as the zone in which the plasma is generated through ionization, this is also typically treated through the use of kinetic theory. The expansion zone (purple) is where a hydrodynamic flow of plasma occurs through the formation of a plasma jet. The remainder of this section will focus exclusively on the dynamics of the expansion zone, though it is important to note that there is extensive theory on the kinetic dynamics of the cathode spot region [5] [19].

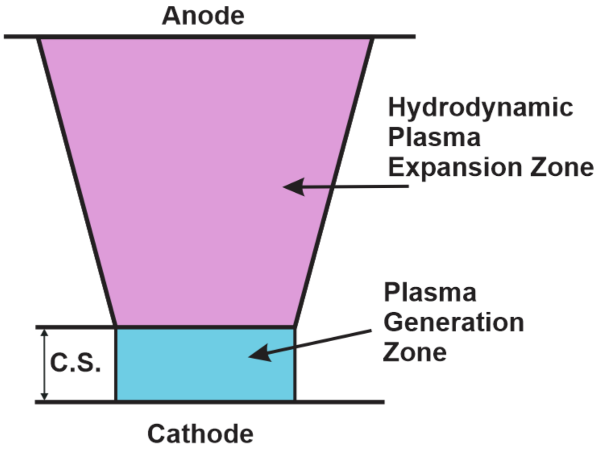

Figure 3.4: Two Dimensional schematic description of the plasma column emitted from a cathode spot(C.S.).

With the above schematic diagram, we can treat the cathode spot as a source of plasma for a high-velocity plasma jet. Within the EEE model for initiation, high energy dissipation takes place at the cathode surface, resulting in a high pressure at the surface. From our schematic we will say that because the plasma generation zone (where energy dissipation occurs) is smaller than the radius of the cathode spot, a force is generated perpendicular to the cathode surface. If we then say the cathode spot that forms is circular, then within the spot the radial plasma gradient is smaller than the perpendicular gradient. Thus, a flow of eroded material is formed at some distance of a few spot radii from the cathode surface, this is known as a plasma jet. As the distance from the cathode increases the plasma expands due to the plasma pressure, and the velocity of the plasma increases. Several mechanisms are responsible for the acceleration of the plasma;

- The pressure of the heavy particles near the cathode surface.
- Electron pressure due to a difference in electron and ion temperature.
- Energy acquired by electrons in the electric field that are then transferred to heavy particles via elastic collisions.

With the above, a complex system of equations to describe in detail the structure of the plasma jet can be found, if the reader is interested I recommend following the derivation in full in Beilis 2003 [7]. I will only be considering the general characteristics of the flow structure, and thus only considered with the integral equations of particle momentum and energy [9];

Momentum Conservation:

$$p_{bl}F_{bl} + Gv_{bl} = p(x)F(x) + Gv(x) \tag{3.21}$$

Energy Conservation;

$$Gv_{bl}^2 + 3I\frac{T_{ebl}}{e} = Gv(x)^2 + 2I\frac{T_e(x)}{e} + Iu_{pl} \tag{3.22}$$

Ohm's law:

$$u_{pl} = \frac{I}{2\pi\sigma_{e1}} \tag{3.23}$$

Where the subscript bl denotes that the equations are on the external side of the cathode spot region, F is the cross section of the jet, U_{pl} is the jet voltage, σ_{el} is the electrical conductivity, and P(x),v(x), and $T_e(x)$ are the pressure, velocity and electron temperature at the jet boundary at a distance x. Equation (3.22) is the solution to Laplace's equation for the potential in the quasi-neutral ($n_i = Zn_e$) region of the near cathode plasma, with the assumption that the electrical conductivity is a weak function of x, and that the current in the spot (radius r_s) is uniformly distributed. Thus, when pressure and electron temperature of the ambient plasma is known the jet parameters v(x) and U_{pl} can be estimated.

Chapter 4

Experimental Results

”*screaming*....*crying*....*laughter*” - Natalia Y. Cordaro (4 months)

4.1 Initial Results

Preliminary work by Dr. Simon Bott-Suzuki on the effects of a power feed vacuum gap for z-scale liners at 1 MA [12] showed in optical emission images (Figure 4.1) an asymmetry in plasma formation when a gap is present, with plasma being more abundant on the left hand side than the right hand side.

The above set of results led to the development of the CGB machine at UCSD to study the effects of a gap at the cathode power feed in a table top environment (see Chapter 2). Initial data collected on the CGB Machine showed asymmetric plasma formation about the azimuth of a coaxial vacuum gap in six consecutive end-on images 4.2

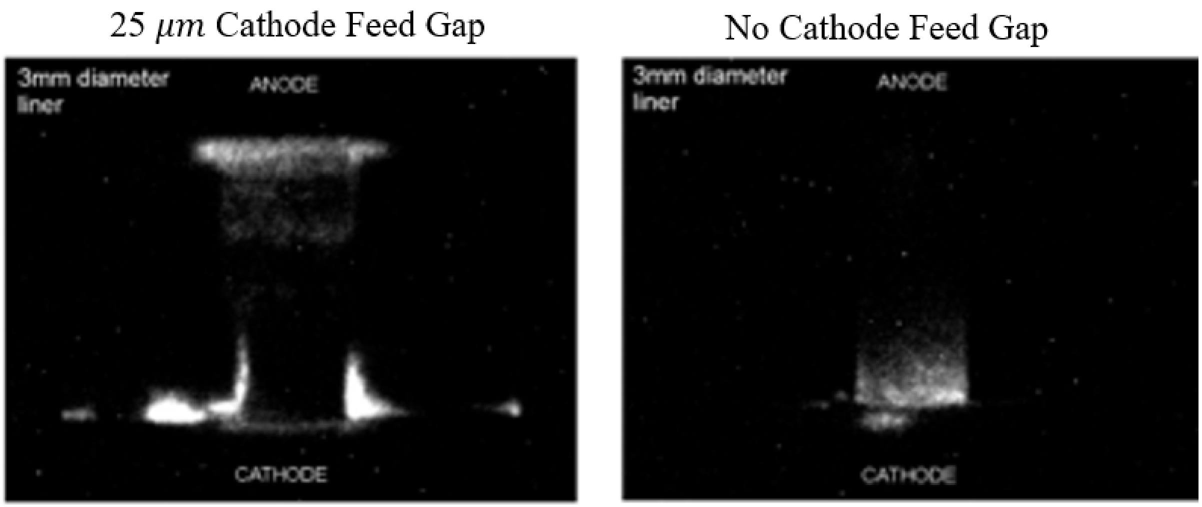

Figure 4.1: Gated optical images (10ns exposure) of Z-scale liners (300μm thick, 6.3mm OD and 10mm tall)with a gap at the cathode power feed (LHS) and without (RHS).

4.1.1 Triangulation and Current Density Measurements

3 Probe Triangulation

To investigate the asymmetric distribution of breakdown observed in the initial results 4.2 a comprehensive method to determine the exact location of a breakdown in a coaxial gap was developed using an array of magnetic field (B-dot) probes. To triangulate the location of breakdown we first calculate the magnetic field at peak current, by use of the following equation,

$$V_{gen} = -N\frac{d\phi}{dt} \rightarrow B = \frac{1}{AN}\int V_{gen}dt \tag{4.1}$$

where V is the measured voltage generated by the magnetic field flux through a loop of area A, and N is the number of loops. With this we can then take the calculated magnetic field for each B-dot probe in the array, and use it to calculate the distance away (R) the breakdown occurred from the probe by use of the following equation at peak measured current (I),

$$\oint B \cdot dL = I_{enc} \rightarrow R = \frac{\mu I_{enc}}{2\pi B} \tag{4.2}$$

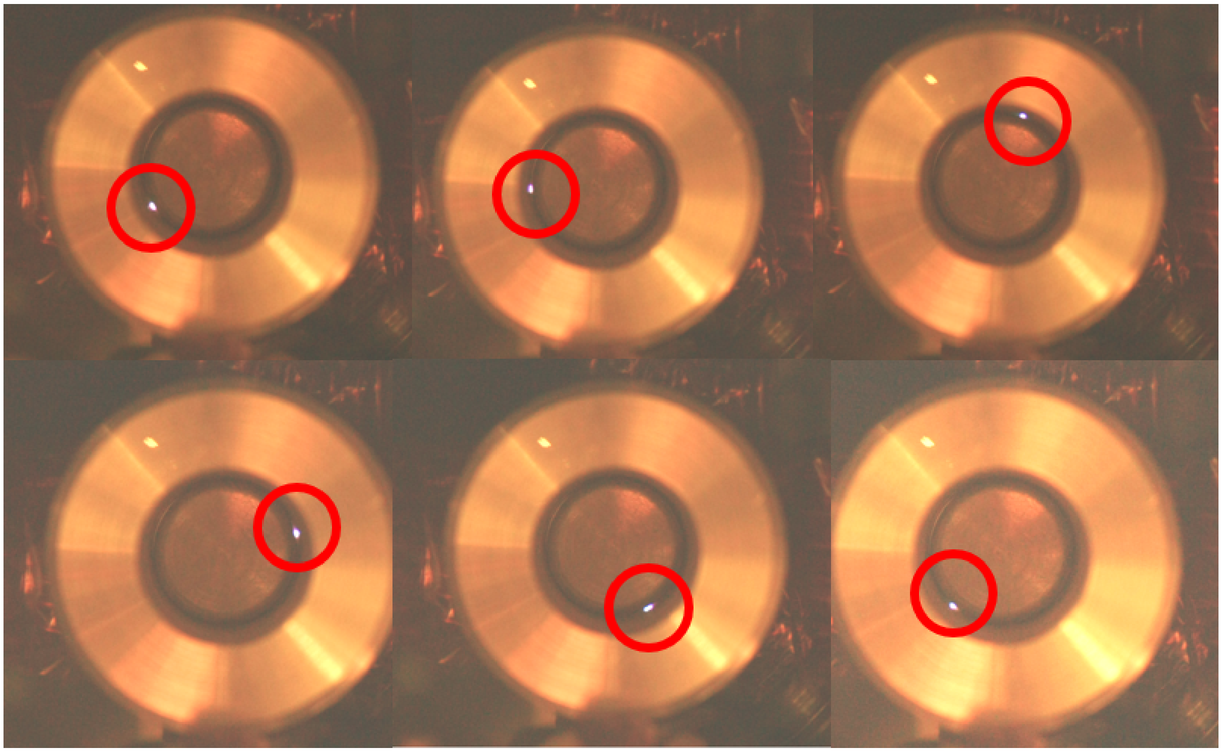

Figure 4.2: Time integrated optical images, 900 μm gap. Breakdown positions circled in red.

If we then generate a circle with the origin located in the center of the corresponding B-dot loop of each probe in the array, and radii corresponding to the different distance away from breakdown (R) for each probe, the intersection of these circles can be observed and thus triangulate the absolute position at which the breakdown has occurred (Figure 4.3). When the triangulation data are overlaid on corresponding time integrated end on optical images, it is observed that the triangulation method determines the exact position that the breakdown has occurred. The accuracy of the 3 probe triangulation method means that the technique can be used to determine the exact position of a single breakdown in a coaxial gap even when axial optical emission imaging is not possible. This is particularly interesting for large machines and transforming lines that are hard to diagnose because of a lack of line of sight.

In order to maximize the effective mapping area of a coaxial vacuum gap, a minimum of three B-dot probes placed at 90°intervals around the circumference of the anode is needed.

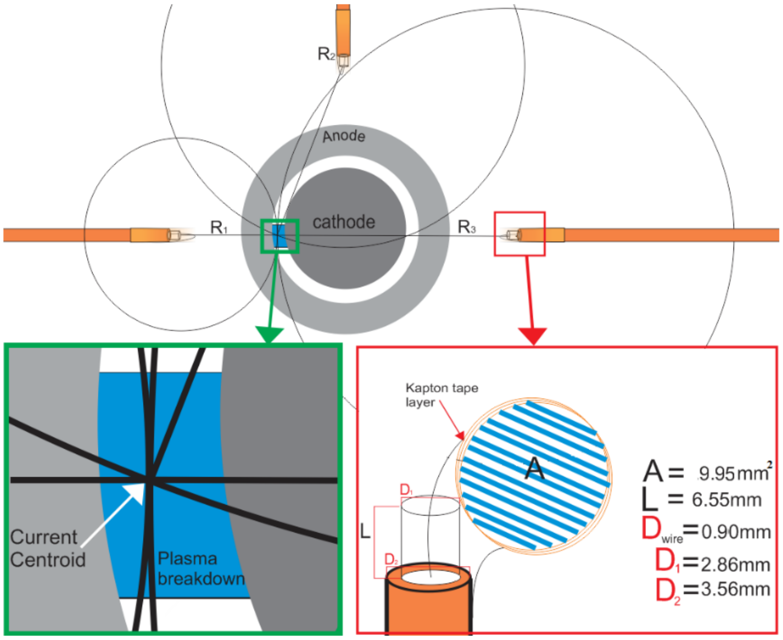

Figure 4.3: Experimental setup diagram..

The distance away from the anode each probe is placed is determined by the experiment and the sensitivity of the probes. Due to the location of the B-dot probes with respect to the vacuum gap, the probes do not read magnetic field signals generated by the radial current vectors of the breakdown.

To illustrate this consider an analytical calculation of the triangulation method on a single breakdown occurring at 90°as in Figure 4.6 with probes placed at 90°, 180°, and 270°. Here we will assume that each of the three probes is set with the same R value way from the center of the inner electrode, and that all of the current is distributed through the single breakdown point only. To simulate a current pulse from the CGB, an approximation fit was performed on a typical operating current trace. With this, the peak magnetic field was calculated using the peak current value and distances the probe was located from the middle of the breakdown (Figure 4.1). The calculated magnetic field values were then used to simulate a trace from each corresponding probe (Figure 4.4).

From Figure 4.4, it can be seen that the 90°probe has the largest magnitude of magnetic

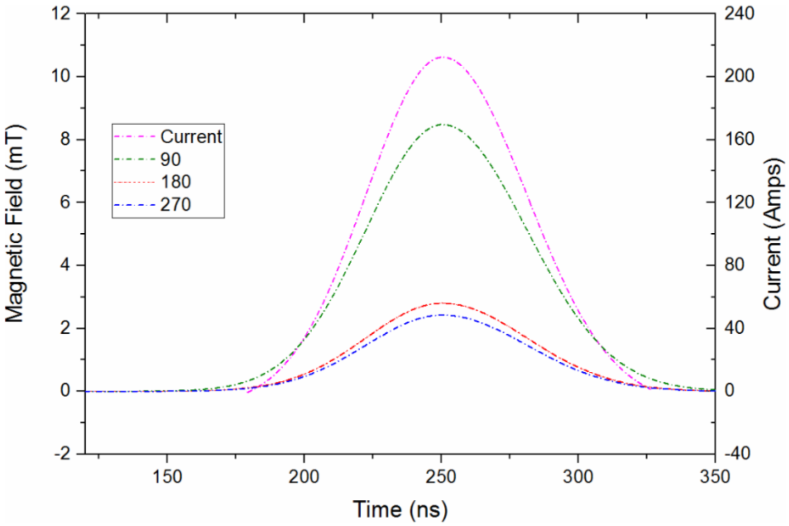

Figure 4.4: Analytical curves for a breakdown at the 90°position.

field followed by the 180°and 270°probes. If we then overlay analytical probe readings atop experimental probe readings from shot no.34 in which breakdown occurred at the 90°position (Figure 4.6b). The resulting figure shows signals that are within a maximum 13% error of one another.

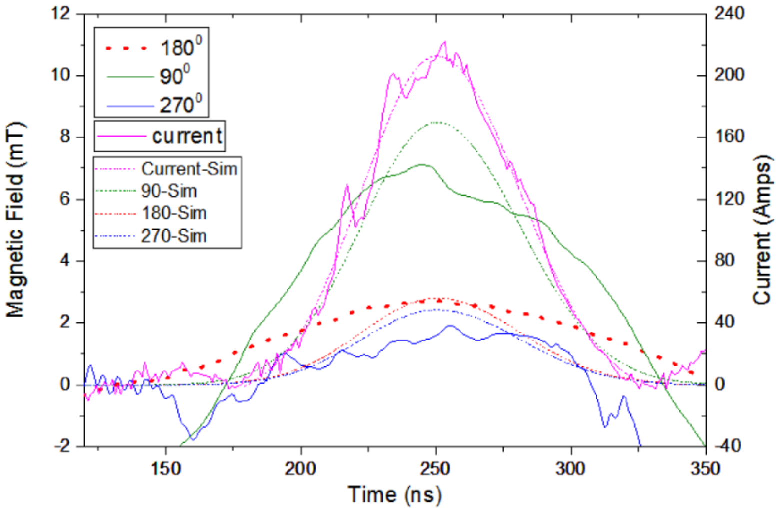

Figure 4.5: Experimental vs. analytical magnetic field and current, shot no. 34.

We can then perform the triangulation technique on the measured signals corresponding to shot no.34, with the calculated distance away from breakdown values in Table 4.1. The resultant

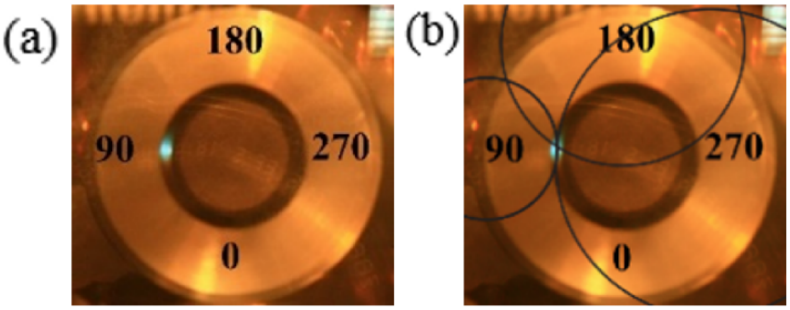

Figure 4.6: Visualization of breakdown triangulation shot no. 34.

circles are then overlaid atop time resolved optical images (Figure 4.6), with the intersection of the three circles lining up with the exact position at which breakdown occurred. Differences in distance and peak magnetic field seen in Table 1 are not an issue if probe placement is known from either careful placement or optical imaging before the shot. Furthermore, distances are a known quantity and thus the probe placement about the azimuth is irrelevant as it does not affect the triangulation technique, though if probes are placed closer than 30°from one another the resultant image is challenging to interpret.

Table 4.1: Analytical and measured values of shot no. 34

Probe	Analytical Magnetic field (mT) peak	Measured Magnetic Field (mT) peak	Calculated distance away (R)(mm)	Analytical distance away (R)(mm)
90	8.48	2.71	16.2	15.13
180	2.80	7.12	6.17	5.0
270	2.42	1.83	24.02	17.52

We can then apply the technique to shot no.45, in which a breakdown occurs between 90°and 180°(Figure 4.8a). The corresponding B-dot signals (Figure 4.7) show the 90°and 180°probe are greater than the 270°probe. The triangulation technique is then applied to the measured peak magnetic field values, and we can then find the corresponding distances away from breakdown that each probe is located Table 4.2. With these values we can now generate three corresponding circles and overlay them atop their corresponding probe centers in the shot specific time integrated optical image (Figure 4.8b). The resultant image accurately shows the centroid of the breakdown.

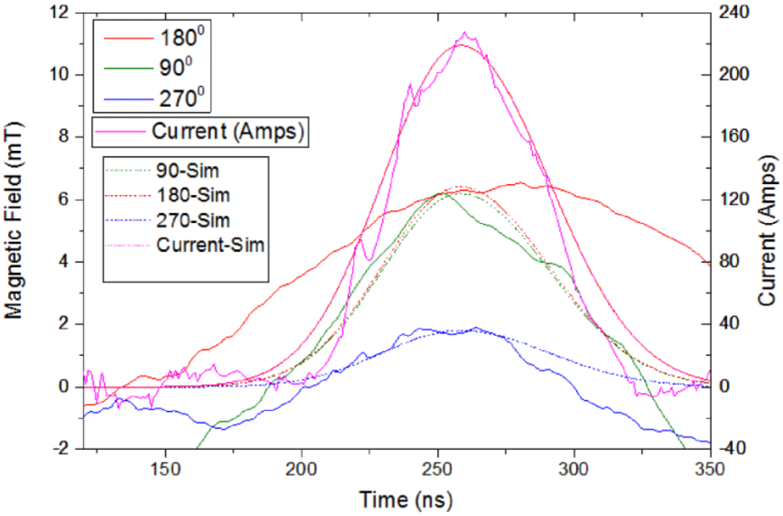

Figure 4.7: Experimental vs. analytical magnetic field and current, shot no. 41.

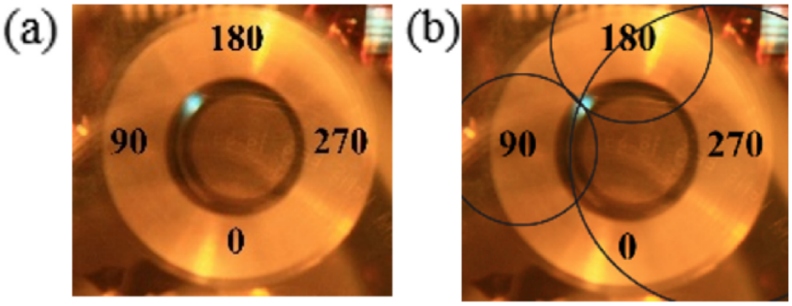

Figure 4.8: Visualization of breakdown triangulation shot no. 41.

Table 4.2: Analytical and measured values of shot no. 41

Probe	Analytical Magnetic field (mT) peak	Measured Magnetic Field (mT) peak	Calculated distance away (R)(mm)	Analytical distance away (R)(mm)
90	6.19	6.21	7.11	7.08
180	6.4	6.41	6.86	7.04
270	1.81	1.81	24.3	24.3

A series of experiments were then carried out on COBRA (1.1 MA, 100ns) at Cornell University, the first such attempt to determine how the triangulation technique scales with current. The load in this experiment was an inverted z-scale aluminium liner (for top down imaging) with gap sizes analogous to those use don the CGB experiments (Figure 4.9). The technique used the same probes used on the CGB but with only a single loop. The entire loop of the probe was wrapped in kapton tape and coated in epoxy to ensure survival in such a harsh environment, similar to the probes [34] made at Cornell University. Analogous to the set up on CGB, probes are placed at 90°intervals around the A-K gap of the COBRA machine 4.9, with each probe position away from the load region of the experiment determined by pre-shot optical imaging (Figure 4.12). Due to the large amount of debris, the probes were replaced with identically calibrated probes after each shot. The probes were calibrated using the Cornell B-dot calibration pulser (3 kA, 100 ns) prior to each shot. The shot series was monitored by axial gated imaging with a 12-frame high speed camera (10 ns exposure, Invisible Vision- Ultra UHSI 12/14) in order to monitor the load for the duration of the current rise to peak (100 ns).

An initial test of the scaling of the technique was performed using a 250 μm aluminium wire offset towards the 90°probe in order to ensure the centroid of the current is in a known location to test the calibration of the probes. Figure 4.11a shows the corresponding magnetic field traces for the off-set wire (Figure 4.10), with the largest magnetic field signal being that of the 90°probe indicating the location of the centroid is off-set in that direction. This is then confirmed when the triangulation technique is used and circles are generated and overlaid atop

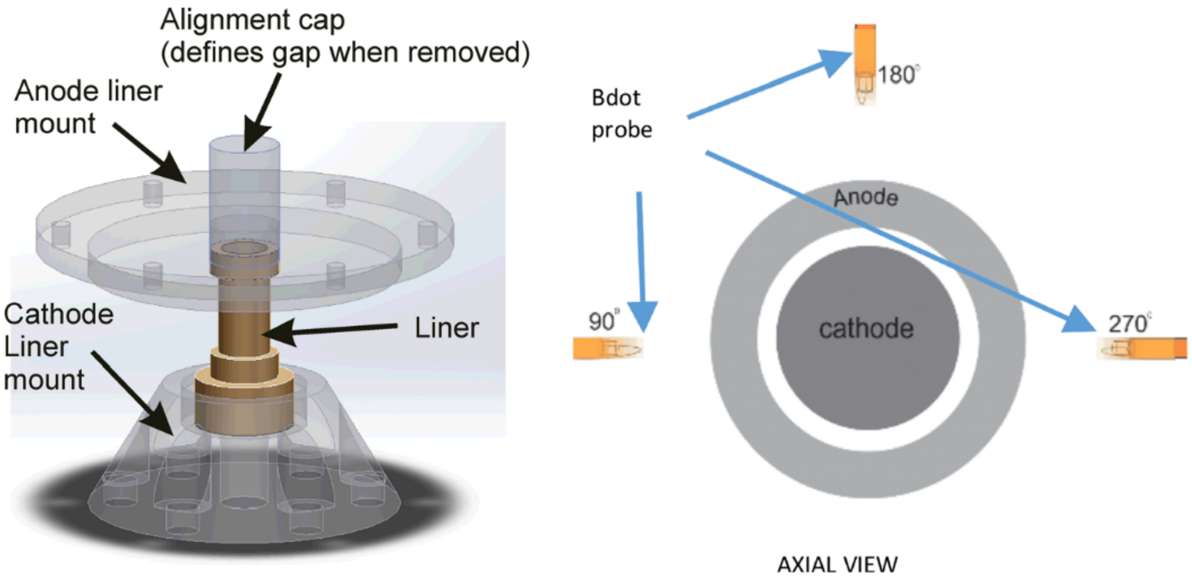

Figure 4.9: Experimental setup on COBRA for Anode power feed gap experiments, showing the axial view of the gap and generic magnetic field probe arrangement.

preshot optical imaging and compared to the axially aligned 12 frame optical imaging (Figure 4.12a).

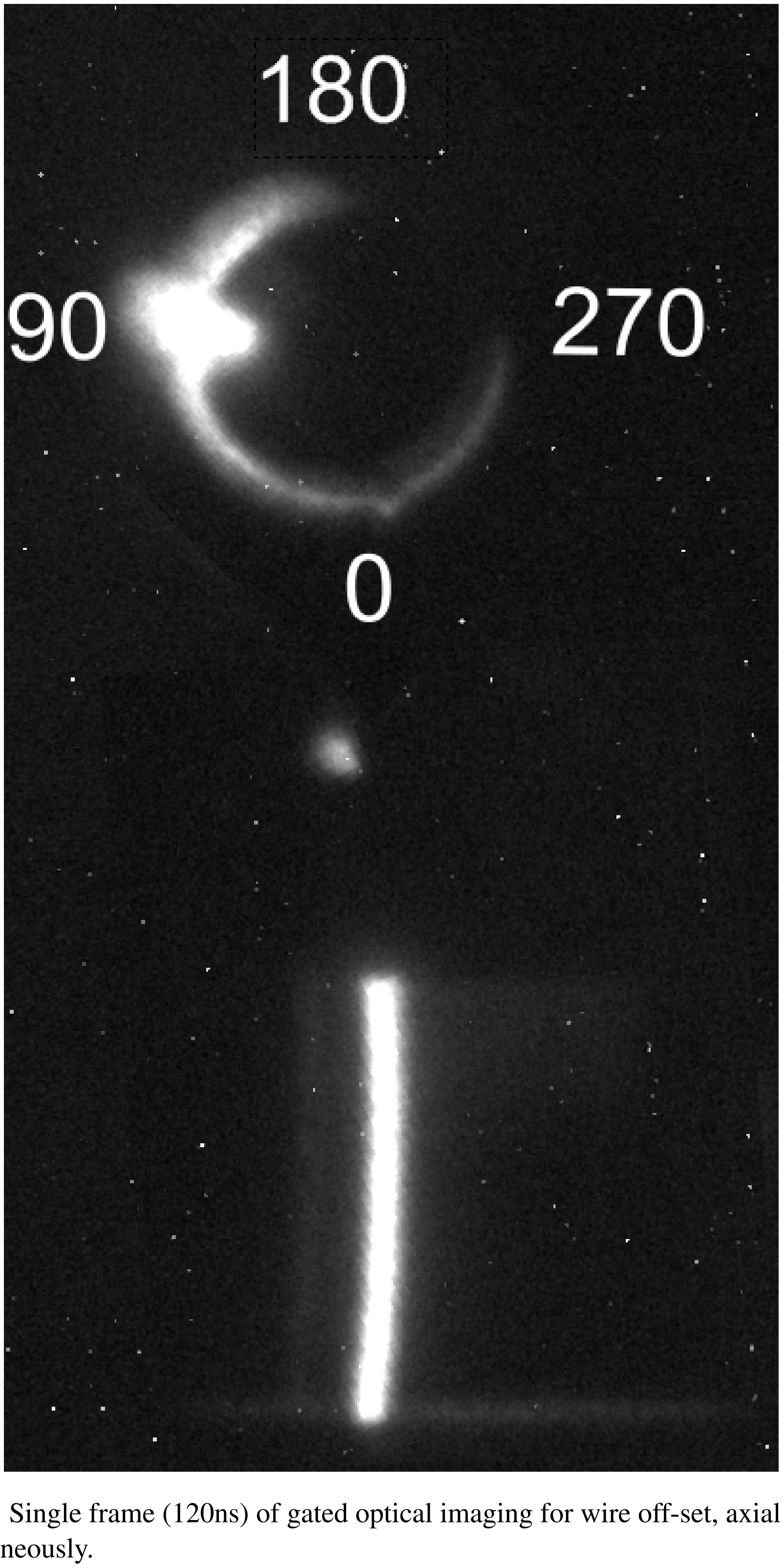

Figure 4.10: Single frame (120ns) of gated optical imaging for wire off-set, axial and radial view simultaneously.

Of particular interest in this series is a shot in which an aluminium liner (400 μm gap) was offset to touch the edge nearest the 180°probe side. Figure 4.11b shows the corresponding magnetic field signals. Again, the triangulation technique was applied and generated circles overlaid atop preshot optical imaging and compared to the axially aligned 12 frame optical imaging (Figure 4.12b). It can be seen that the centroid of the current is located again at the contact point of the liner at the 180°probe side. The red circle in the triangulation shot represents the actual position of the liner when the imaging angle is corrected.

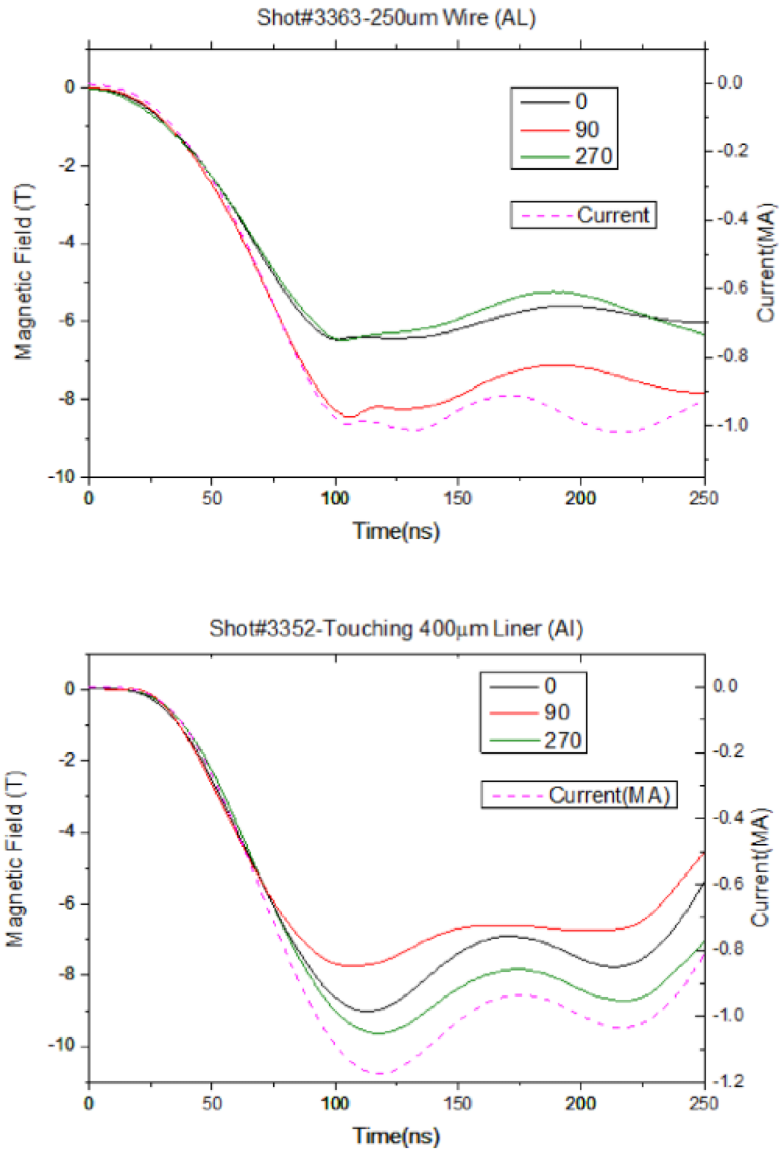

Figure 4.11: COBRA magnetic field and current signals. interest.

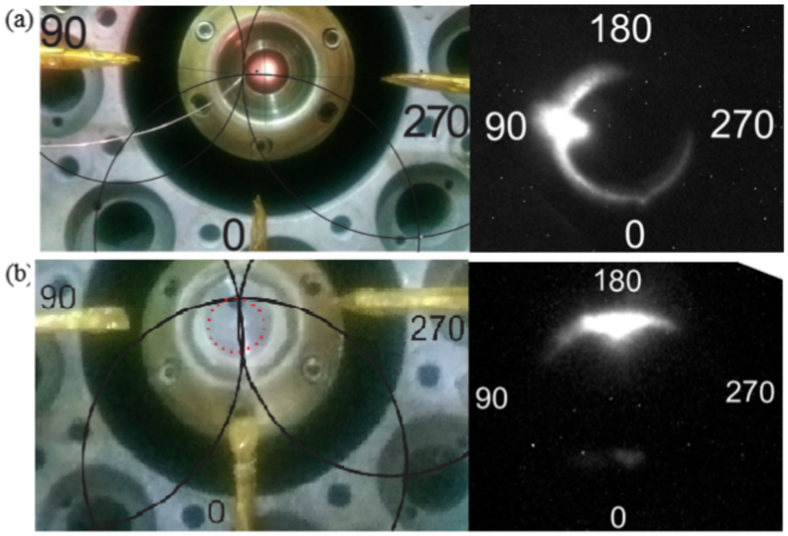

Figure 4.12: Triangulation visualization Cornell experiment.

With the above we have shown that with the use of three B-dot probes, at a minimum, one can determine the exact location at which a breakdown has occurred within a coaxial gap by use of the triangulation technique. This technique is very effective and scales well to larger devices.

Note, however, that the three probe triangulation accuracy diminishes when multiple breakdowns occur, changing from an exact location to an effective area at which breakdown occurs. For instance, when the depth into the plane of the gap is long ($L >> 5$ mm) the 2-D triangulation technique cannot accurately detect variations of the magnetic field corresponding to breakdowns about the length of the electrode.

9 Probe Array Current Density Measurements

The methodology to determine the azimuthal symmetry of breakdown and how it influences the current density described in the previous section were then expanded upon to include two additional axial positions along the length of the electrodes, each with three probes to give a total of nine probes reporting the azimuthal current density symmetry at 3 different axial positions [22].In the initial study, we examined two azimuthal gap sizes 400 μm and 900 μm, and penetration depths (PDs) of the central conductor into the hollow (outer) electrode from 3.72 mm to 9.88 mm. The array geometry used for this case is given in 4.13. With each set of three probes spaced at 120°around the azimuth and separated by 30 mm along the axial direction.

The exact location of each probe relative to the electrodes is recorded via spatially calibrated optical images. The zones are labeled Zone 1 (close to high voltage connection), Zone 2 (at the position of the coaxial vacuum gap) and Zone 3 (close to the ground connection). We can then use the triangulation technique for each zone and subsequently map the evolution of the current density over the duration of the current pulse, and as the pulse travels along the length of the electrodes.

To illustrate this, we consider shot.01 where a breakdown occurs at the 270°position of a 400 μm gap (Figure 4.14). Shown in Figure 4.15 are the raw magnetic field probe data for all

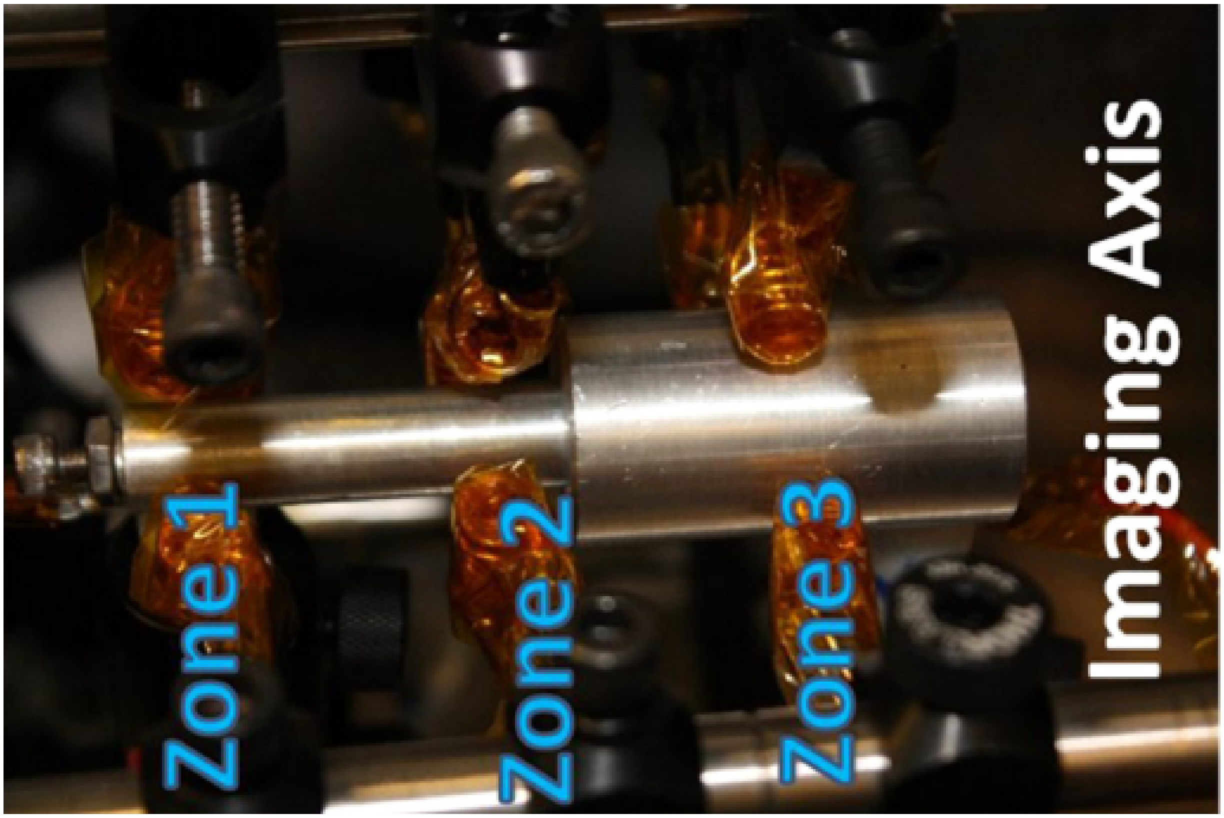

Figure 4.13: Electrodes with 9 probe b-dot array zones labeled.

probes in all zones, along with the current pulse. The magnetic field signals generally follow the trend of the current as expected, but with different measured magnitudes observed between the probes at different azimuthal locations.

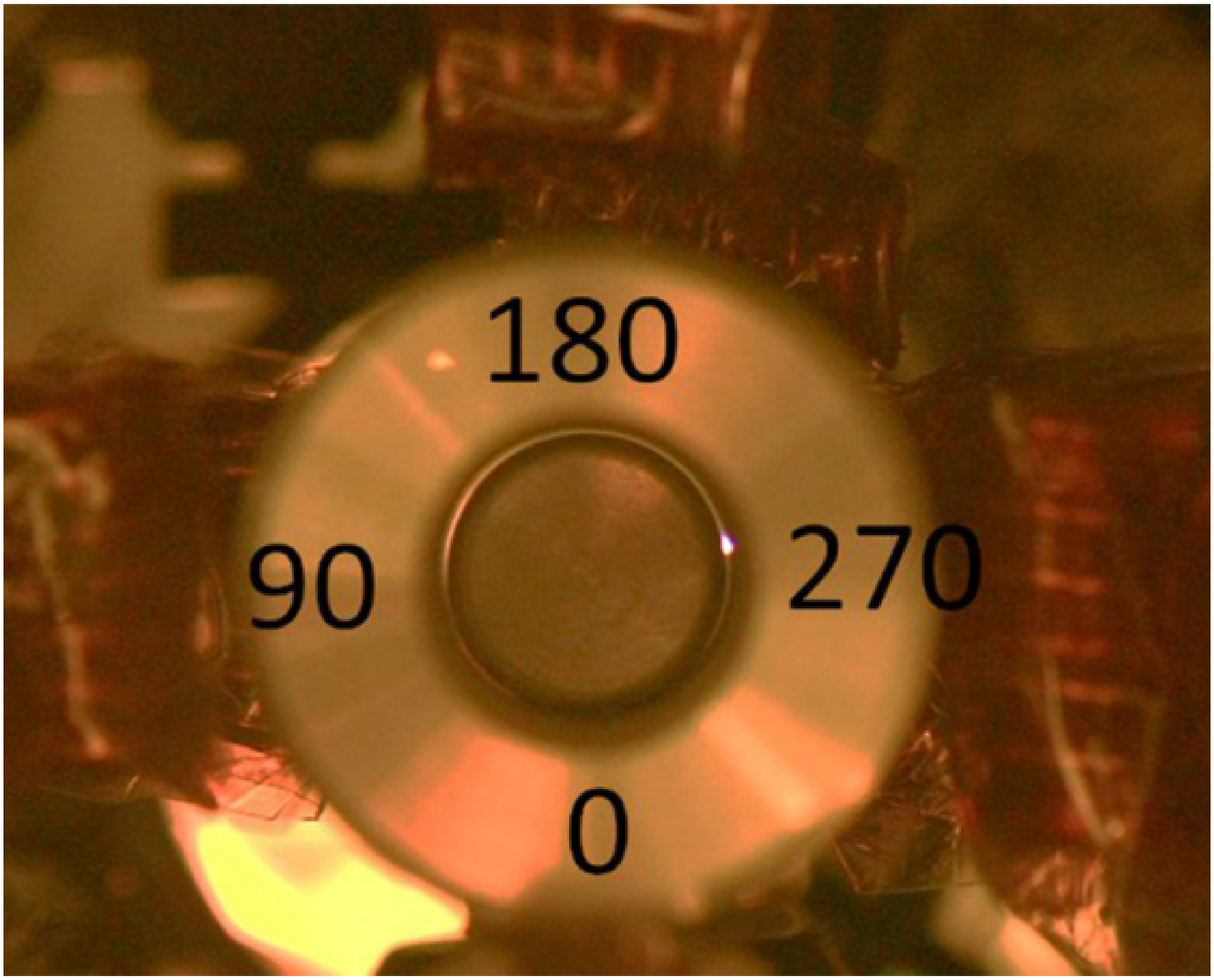

Figure 4.14: Time-integrated optical image of vacuum gap breakdown for a 400 μm gap, showing the location of the breakdown at 270°.

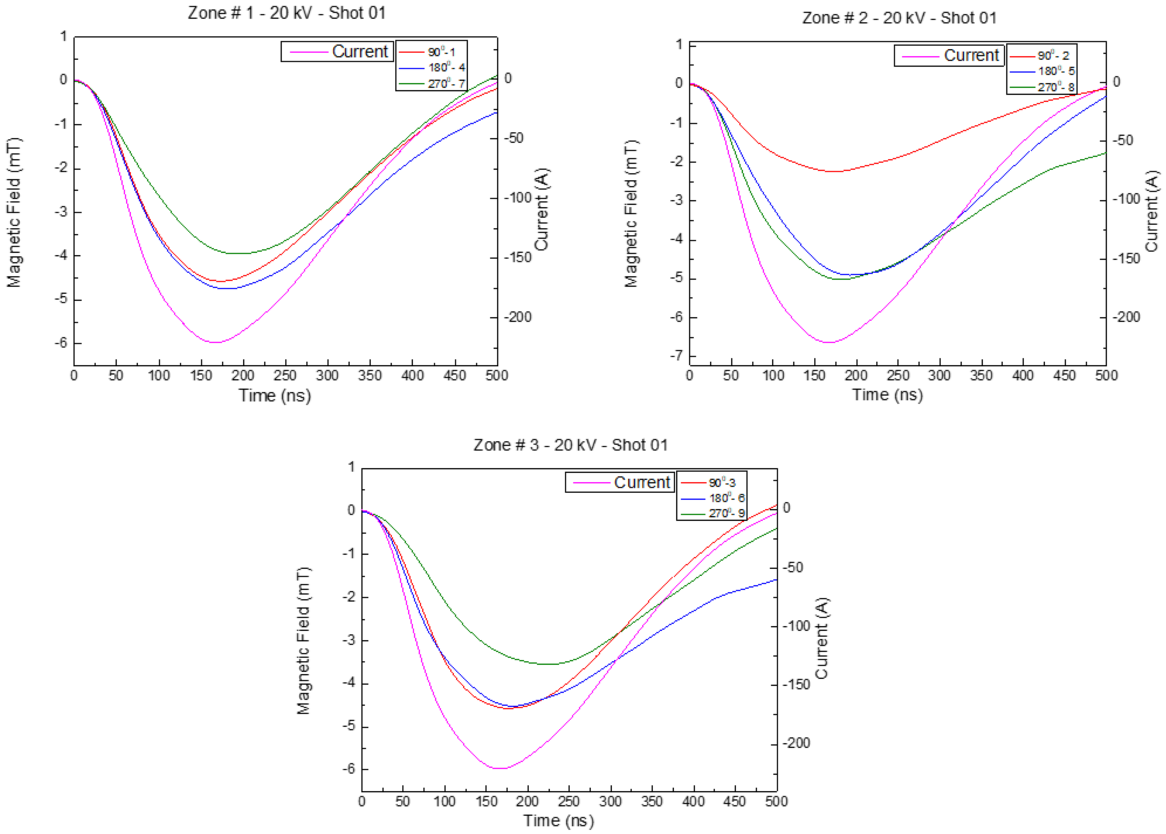

Figure 4.15: Magnetic field traces, 400 μm gap, Al linear-breakdown at 270°.

Analysis of the probe data for each zone is carried out using a data analysis program I wrote in MATLAB, which uses the probe location and measured signals to construct a circle of a radius consistent with the total current recorded and overlays this information atop corresponding time integrated optical image for the shot.

To simplify the analysis for all three zones, triangulation data were calculated every 10 ns starting at 100 ns into the current drive (Figure 4.16)

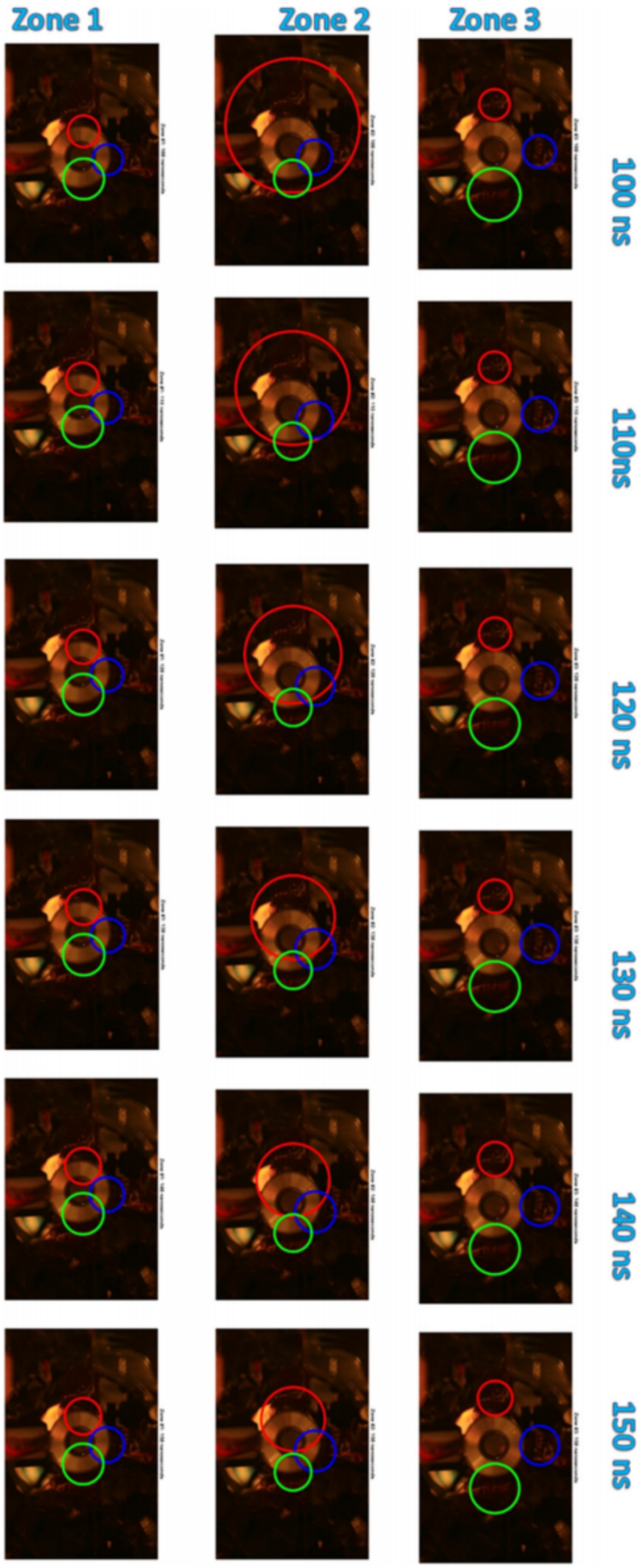

Figure 4.16: Triangulation matrix, the color of each zone corresponds to the azimuthal position, as in Fig. 3. Red-90°, Blue-180°, Green-270°.

The triangulation matrix shows distinct behaviors between each zone. In Zone 1, 100ns, the magnetic field probe indicates the current density is in the 90°- 180°region, this is shown optically in the matrix by the smaller red and blue circles compared to the larger green circle. In Zone 2, during the same time, the current density has shifted towards the breakdown location 270°, again this is seen in the triangulation matrix with blue and green circles being small and the red one being larger. These circles eventually overlap near 140 ns and accurately locate the single position of breakdown. In Zone 3, the current density shifts back to 90°- 180°region seen in Zone 1 images. These offsets are distinct and remain throughout the 50 ns duration of the current pulse as seen in the triangulation matrix images. It is important to note, however, that often the location is only an approximation. Still, this technique highlights significant motion and persistent non-uniformity for the duration of the current pulse along the length of the electrodes.

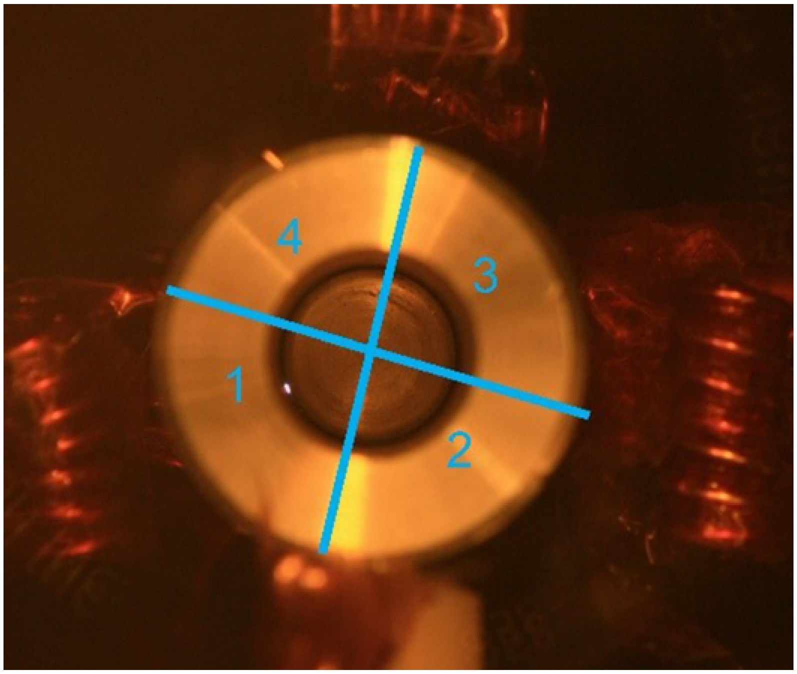

Figure 4.17: Coaxial gap quadrant overlay; 400 μm, PD-3.03mm, 25 kV .

To better understand how the magnetic field evolves from shot to shot, a method was devised in which the time integrated optical image of the coaxial gap is broken into a standard quadrant system with Quadrant 1 always centered on the position of breakdown (Figure 4.17).

If we then combine the data from the triangulation method with the quadrant system, the result is a quadrant map of the magnetic field evolution within the quadrant system, taken at 10 ns steps during the current drive starting at 100 ns (Figure 4.18). In Figure 4.18 we have done this for a single breakdown in a 400 μm gap that occurred near 90°. Here Zone 2 is the location of the breakdown across the gap and is defined as Quadrant 1, therefore Zone 2 stays at Quadrant 1 for the duration of the experiment. In Zone 1, the current density remains in Quadrant 2 from 100 ns to 150 ns. While in Zone 3, a transition of the current density is observed from Quadrant 3 to Quadrant 4 between 130 ns and 140 ns (denoted by the horizontal line). From this individual Quadrant map, a persistent offset in current density is observed in the presence of an azimuthally asymmetric breakdown in the gap. The motion of the current density about the electrode is observed, and the current density locations up- and down- stream of the breakdown do not correspond to the azimuthal breakdown location. With this simplification the discussion hence forth will focus on highlighting large motions of average current density position throughout the current drive timescale for multiple shots at various gap sizes and penetration depths.

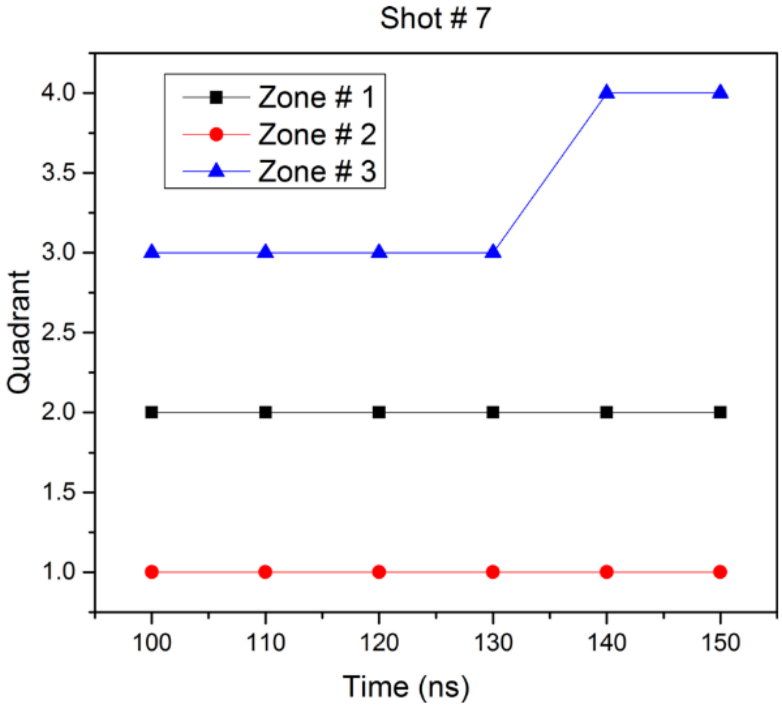

Figure 4.18: Quadrant mapping of a 400 μm, PD-3.03mm, 25 kV breakdown near 90°.

The Quadrant mapping technique was then applied to 50 shots each for 4 geometries: a 400 μm gap with penetration depths 3.03 mm and 6.33 mm and a 900 μm gap with penetration depths 3.72 mm and 9.88 mm. Figure 4.19 shows the Quadrant mapping resulting from the change in penetration depth from 3.03 mm and 6.33 mm for a 400 μm gap, each comprised of 50 shots. At a penetration depth of 3.03 mm, the current density can occupy any of the 4 Quadrants in both Zone 1 and Zone 3. There was also limited motion observed between Quadrants during the experiment. It is immediately noticeable that the current density does not look uniform at any time for these 50 shots. When the penetration depth is increased to 6.33 mm, there is a distinct change in behavior. Most notably being the transitions observed in Zone 3 and Zone 1. These transitions are constrained to Quadrants 3 and 4 in Zone 4, and then to Quadrants 3, 2 and 1 after 100 ns in Zone 1. Again, we have observed a persistent changing non-uniformity on either side of the asymmetric azimuthal breakdown over 50 shots and across the length of the electrodes and tens of nanoseconds.

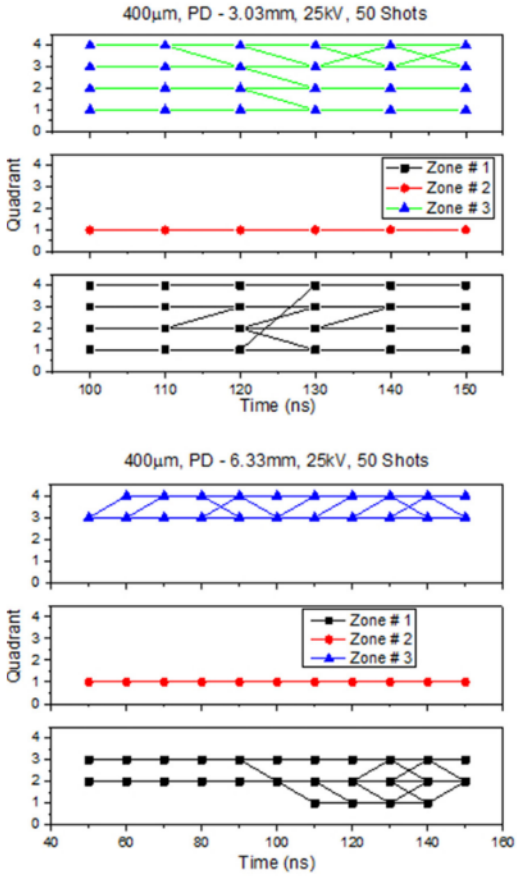

Figure 4.19: Quadrant mapping of a 400 μm, PD-3.03mm,PD-6.33 mm, 25 kV, 50 shots each.

The resultant Quadrant map for the 900 μm gap shot series is show in Figure 4.20. Several interesting features are observed. Firstly, there are now vertical lines for all times examined in both Zones 1 and 3, this denotes that for many shots, the current density was distributed around the electrode; i.e., occupying all 4 Quadrants at the same time. This behavior was not observed in the 400 μm gap size. In addition, there are more transitions occurring, as the current density moves around the electrode (horizontal lines). For the 3.72 mm penetration depth, these transitions occur almost entirely from Quadrant 4 to Quadrant 1, and it would appear that the current density is either uniform (located in all four Quadrants) or off-set close to the position of breakdown in Quadrant 1. For the 9.88 mm penetration depth, whilst uniform current density is observed at all times plotted, there is also significantly more motion of the current density between all Quadrants. This increased movement would suggest that the position of breakdowns has less effect in influencing the offset of the current density for an increased penetration depth.

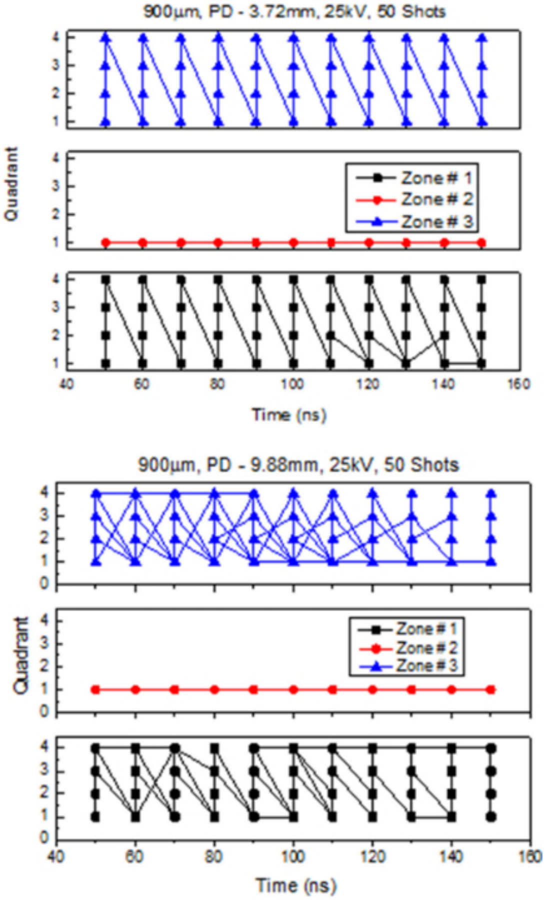

Figure 4.20: Quadrant mapping of a 900 μm, PD-3.72mm,PD-9.88 mm, 25 kV, 50 shots each.

Much like before and in the rest of the presented work, the above experiment to measure the current density along the length of electrodes through the duration of the current pulse was modified and scaled to be performed at 1 MA (120 ns) on Z-scale aluminium liners at COBRA, with 12 magnetic field probes placed in four azimuthal locations and three places along the length of the liner (Figure 4.21) [13] Unlike in previous experiments the B-dot probes in this series survived all 15 shots taken due to the outer kapton layer shield.

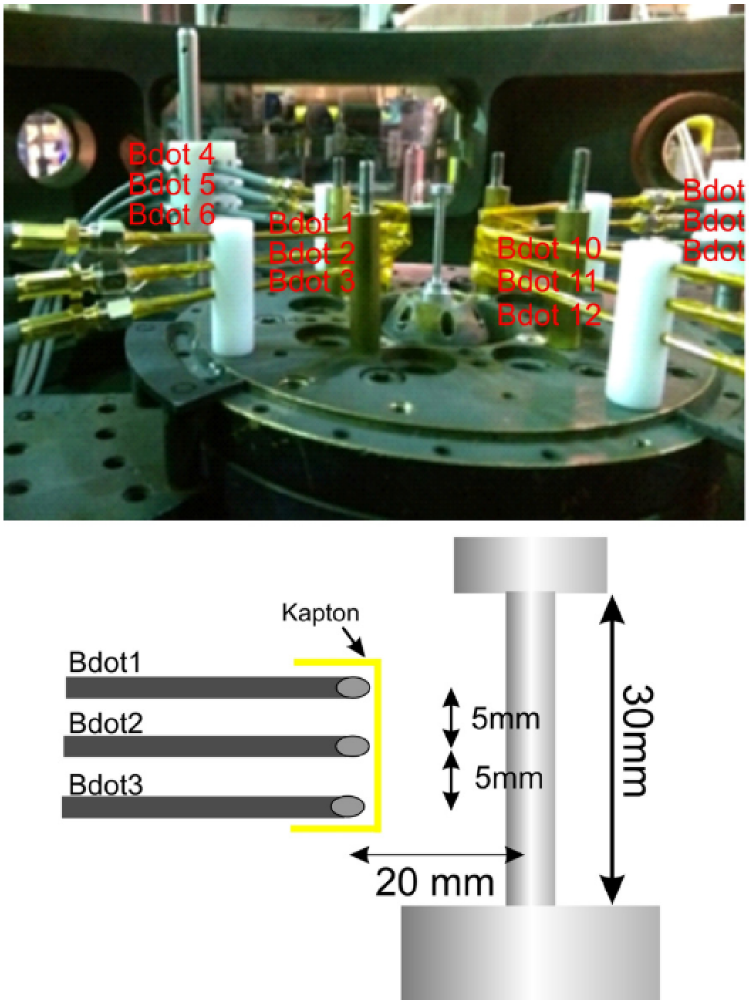

Figure 4.21: Optical image and schematic of magnetic field probe array for 30mm tall liners on COBRA. Probes 1, 2, and 3 are at 0°, probes 4, 5, and 6 at 90°, 7, 8, and 9 at 180°, and 10, 11, and 12 at 270°. Probes are shielded with inner and outer kapton layer.

The following experimental data is from aluminium liners with the following specifications; 150 μm wall thickness, 30 mm in length, and a 200 μm uniform gap. In addition to the 12 B-dot array, the gap was monitored by a top-down high speed 12 frame gated optical camera.

Figure 4.22 shows a single emission frame taken at 50 ns into the current rise and the corresponding triangulation plots for the three axial positions of the B-dot probe array (Top, Middle, Bottom). It can be seen in the top position, the closest to the imaging location and the gap, the probe circles overlap at the center of the liner, this indicates that the current centroid is centered on the liner. This does not indicate a uniform current distribution in the entirety of the liner, especially when comparing this to the gated optical emission image that shows a localized non-uniformed emission region in the gap. The middle probe position, 5 mm below the top probe, triangulation shows an offset towards the 0°and 90°probes. This means that the magnetic field measured by probes 2 and 11 has increased, which indicates a movement in the current centroid towards the bottom right side of the liner (in the image). In the bottom position probes, probe 9 shows the largest magnetic field and thus smallest circle, indicating an offset of the current towards the top of the liner (in the image). All these together show that the location of the current in the liner differs with axial position at a single point in time (50 ns). As mentioned above in the 3 probe triangulation at 1MA, when there are multiple breakdowns in the gap the triangulation accuracy goes from pinpointing a single location at which the centroid is located to an effective region the centroid is located in. This is further compounded when each breakdown is carrying some amount of current that equals the total drive current. Yet the fact still remains that there exists an axial and local variation in the current density.

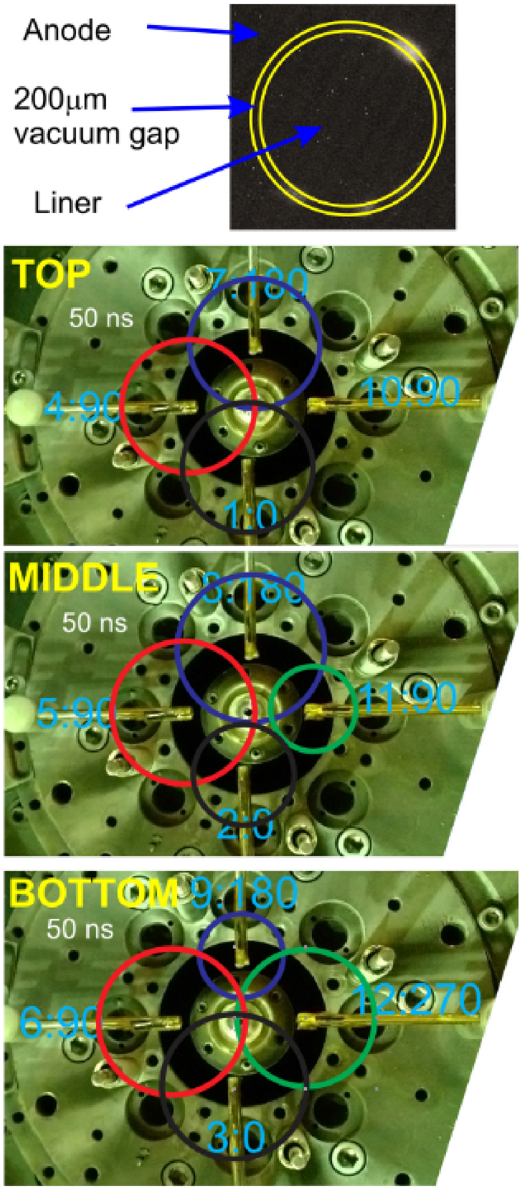

Figure 4.22: Gated optical image of aluminum liner experiment at 50 ns. Circles show triangulation of B-field signals for each probe position overlaid on digital optical top-down image of liner without anode plate present.

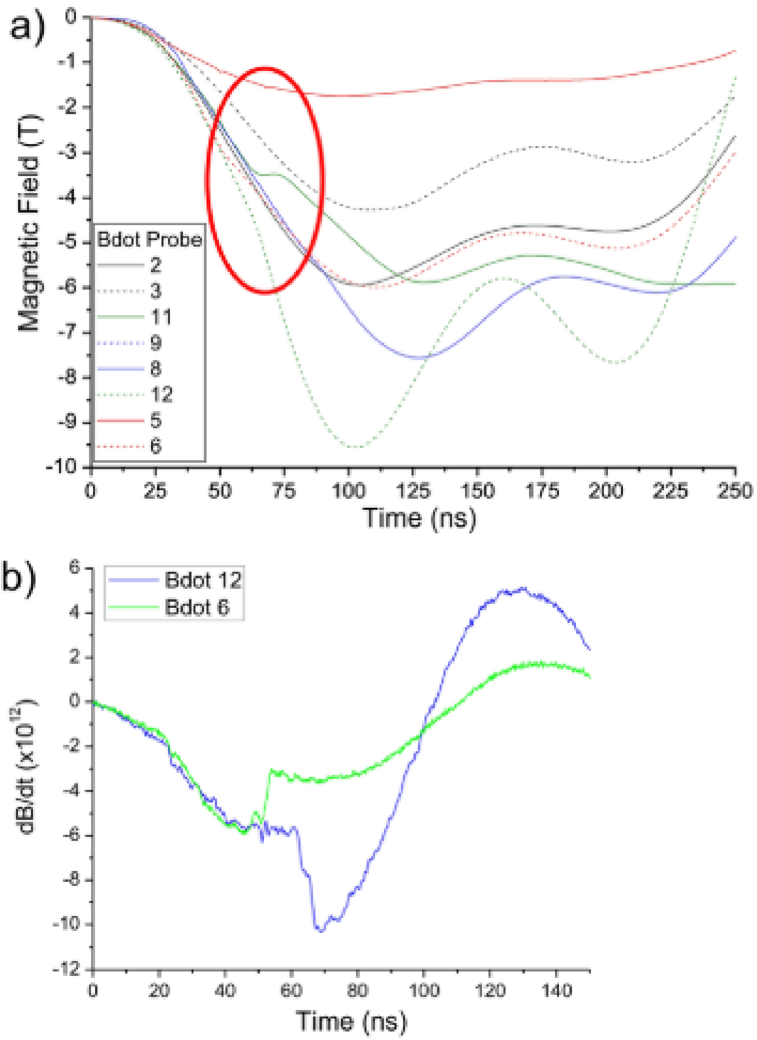

Figure 4.23: Magnetic field probe signals highlighting deviation of measured B-field from current trend indicating motion of the current density position in the liner.

If we then examine the integrated B signals and the raw dB/dt signals, (Figure 4.23) we can see that these axial variations persist through the duration of the current pulse. This is evident first in the fact that the magnetic field signals in the image do not all overlap for the duration of the pulse. In fact there are some very large movements that can be seen, specifically in Figure 4.23a in the red circle we see a large deviation in the gradient of probes 6, 11, and 12. This deviation indicates significant movement of the current about the liner. Where probe 6 and 12 change simultaneously at 50 ns. This deviation can be seen in more detail when looking at the raw dB/dt signals (Figure 4.23b), showing a sharp decrease in signal for probe 6 at 50 ns and a sharp increase for probe 12 at 60 ns, when before 50 ns the two signals overlapped perfectly. What is particularly significant about this is that these probes are in the same axial position, but opposite sides of the liner, which means between 50 ns and 60 ns the current moved from one side of the liner to the other. This movement is observed in all liner shots done at Cornell to date.

In this section we have shown that asymmetries in the azimuthal breakdown position have an influence on the asymmetric current distribution in time and space along the length of the electrode. These asymmetries in current density can be influenced by changes in the gap size and penetration depth, and have measured experimentally as a function of time and space. In addition, we have shown the technique to measure axial asymmetries and correlate them to azimuthal asymmetries scales to megaampere currents, and these asymmetries persist through the duration of the current pulse.

4.2 Fowler-Nordheim Analysis

This section will show the results of experiments that make use of the Fowler-Nordheim analysis outlined in Chapter 3.5. Using recovered electrical data from each shot on the rep-rated CGB machine we are able to investigate how the work function, the emitter geometry, and the field enhancement factor change with changing penetration depth and gap size.

4.2.1 Preliminary Results Link to Uniformity

In addition to the imaging analysis and triangulation outlined in the previous section, the recovery of electrical data on every shot allows for the characterization of the breakdown process through calculation of the Fowler- Nordheim (FN) enhancement factor [57] for each case. This describes the likely breakdown voltage of an electrode set over and above that, expected as a result of the material work function alone. Using the process outlined in Chapter 3.5 we can pull out and plot the enhancement factor with respect to penetration depth and correlate changes in enhancement factor and penetration depth with movement of current density from quadrant mapping.

We do this now for a 400 μm gap at two penetration depths, 3.03mm and 6.33 mm, the resultant graph (Figure 4.24) shows the variation in enhancement factor with penetration depth. Generally we see an increase in enhancement factor with increasing penetration depth for the 400 μm gap. If we then compare this to the Quadrant mapping (Figure 4.19) for all 50 shots of these two penetration depths we can see (abridged explanation from above in section 4.1.1) that as enhancement factor and penetration depth increases the amount of movement about the electrode increases.

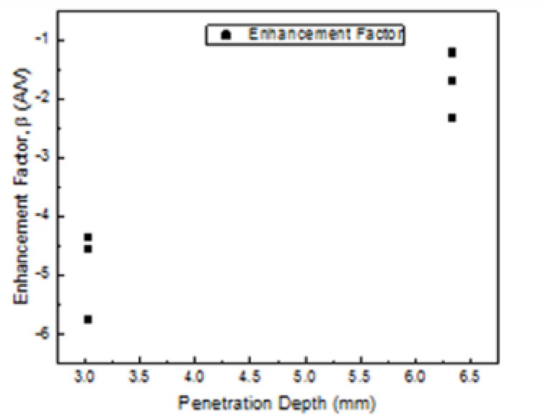

Figure 4.24: FN enhancement factor and quadrant maps for 400 μm gaps at dif- ferent penetration depths.

4.2.2 Gap Size and Surface Profile

Subsequent experiments on the CGB machine were performed using Fowler-Nordheim analysis on 2,000 shots for 5 azimuthal gap sizes (50, 100, 150, 300, 700 μm) and penetration depths from 1.5 mm to 8.5 mm. It is important to note that prior to changing penetration depth, the cathode is changed and the anode is cleaned. In addition following machining electrodes are cleaned with alcohol and not polished or treated further. The typical surface roughness of the anode and cathodes is 5-10 μm as determined by SEM imaging (Figure 4.25)

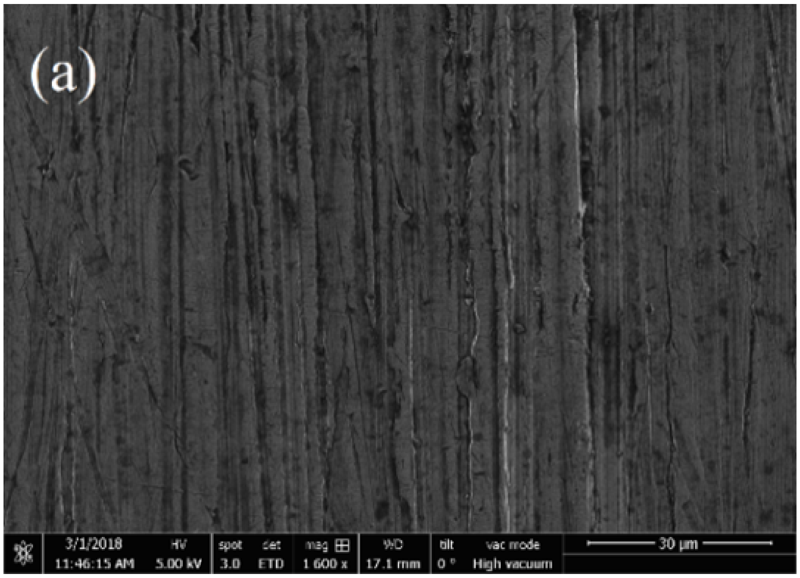

Figure 4.25: Surface roughness (30 μm scale – Vertical machining lines.

We then apply Fowler-Nordheim analysis to the 2,000 shots over 5 geometries at 9 penetration depths. In this experiment a single shot series for a given geometry and penetration depth consists of 50 shots whose enhancement factor (Chapter 3 equation - 3.15) is then averaged and plotted against penetration depth.

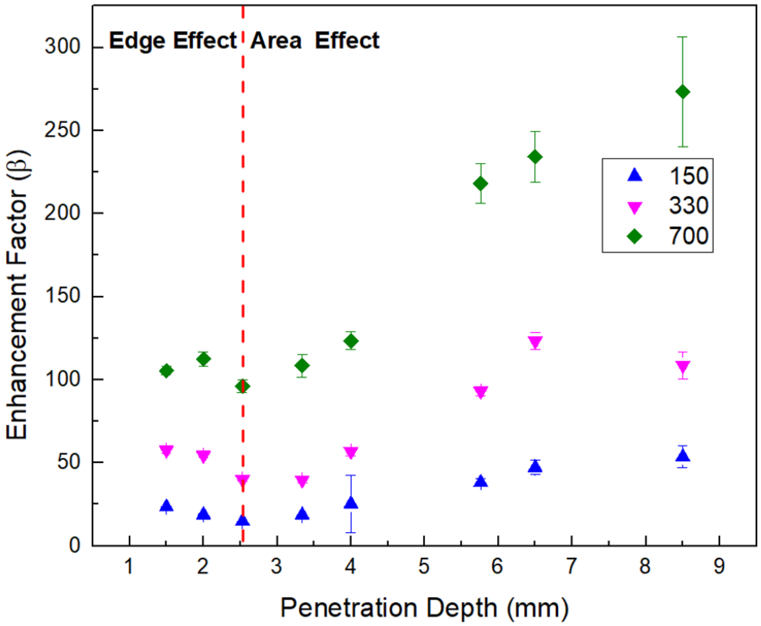

Figure 4.26: Average Enhancement Factor vs. Penetration Depth for 150,300, and 700 μm gaps. Increasing value with penetration depth.

Figure 4.26 shows the enhancement factor plotted over increasing penetration depth for 150 μm, 300 μm and 700 μm. At a penetration depth of 1.5 mm the enhancement factor for 150 μm is 20 and decreases to a value of 10 at a penetration depth of 2.53 mm. Once the penetration depth passes this point the enhancement factor increases with increasing penetration depth and area to a maximum value of 45 at 8.5 mm penetration depth. The initial decrease and subsequent increase seen here below 2.5 mm penetration depth is believed to be due to the dominance of the cathode edge in the gap, where at depths beyond 2.5 mm the geometry of the gap and area of the inserted cathode likely play the dominant role in the value of the enhancement factor. Similar behavior is seen in the 330 μm and 700 μm gap size electrodes tested.

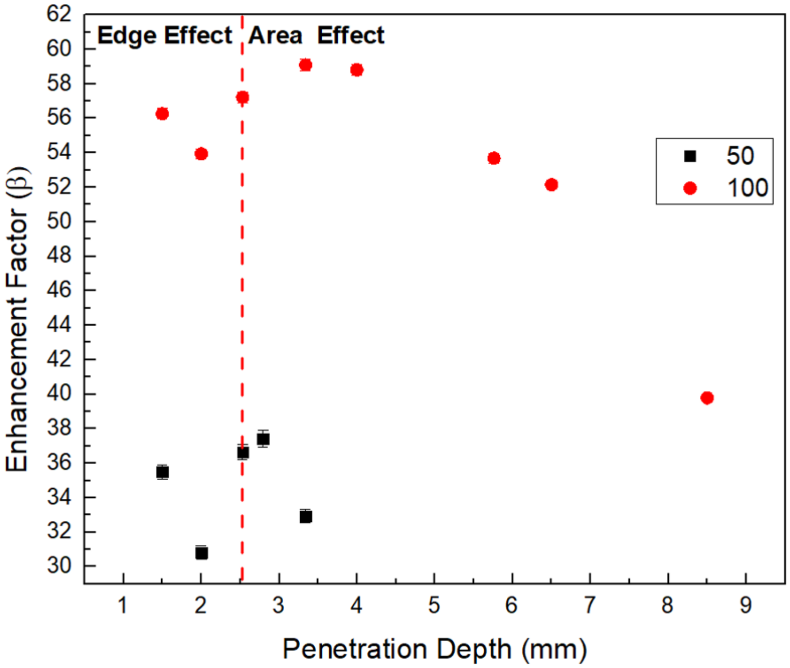

Figure 4.27: Average Enhancement Factor vs. Penetration Depth for 50, 100 μm gaps. Increasing value with penetration depth.

Figure 4.27 shows the average enhancement factor plotted against increasing penetration depth for 50 μm and 100 μm gaps tested. At 1.5 mm penetration depth for 100 μm the enhancement factor is 56. As the penetration depth increases to 2.0 mm the enhancement factor decreases to a value of 54. Increasing the penetration depth further to 3.44 mm we see a slight increase in enhancement factor to 60 before decreasing to a value of 40 at 8.5 mm. This initial trend appears to be similar to the initial trend seen in the 150, 330, and 700 μm gaps. Again, this is likely due to the edge effect of the cathode. However, this decreasing trend continues for all remaining penetration depths past 3.34 mm in the 100 μm gap, and after 2.79 mm for the 50 μm gap. It is important to point out the limited number of data points for the 50 μm gap, which is due to difficulty in ensuring a centered gap at large penetration depths.

To better understand the behavior observed in the plots above, we look to the electrode surface before and after breakdown events. Described in greater detail in Chapter 3, electrode surfaces before and after breakdown events are enhanced by the presence microprotrusions (emitters). Figure 4.28 shows a simple diagram of a microprotrusion [53], with the dotted line representing the protrusion height (r) before current is passed through the cathode and the solid line afterwards. Once current is passed into the cathode, current density increases the temperature of the microprotrusion, such that it eventually melts and ionizes the material. A portion of the microprotrusion remaining in the melt stage [50][56] is then explosively propelled into the gap and across the cathode surface in the form of a liquid metal jet, creating additional microprotrusions as it lands and cools leaving behind a crater in the cathode surface from the explosion origin. A crater may have a height which varies either above or below the original cathode surface level [25], effectively becoming another set of microprotrusions. The process above occurs at all breakdown positions on the cathode, evidence of this can be seen in the rest of this section in SEM images [37].

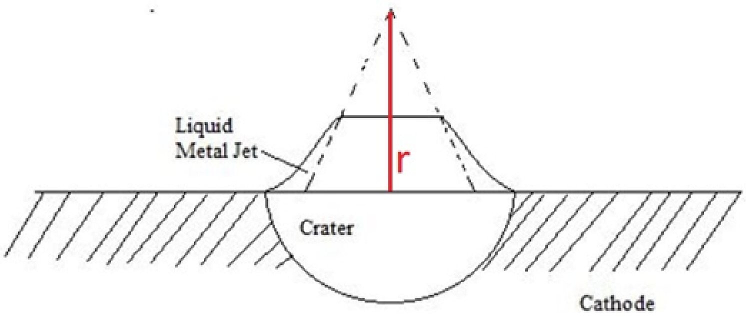

Figure 4.28: Microprotrusion transition to liquid jet and crater diagram

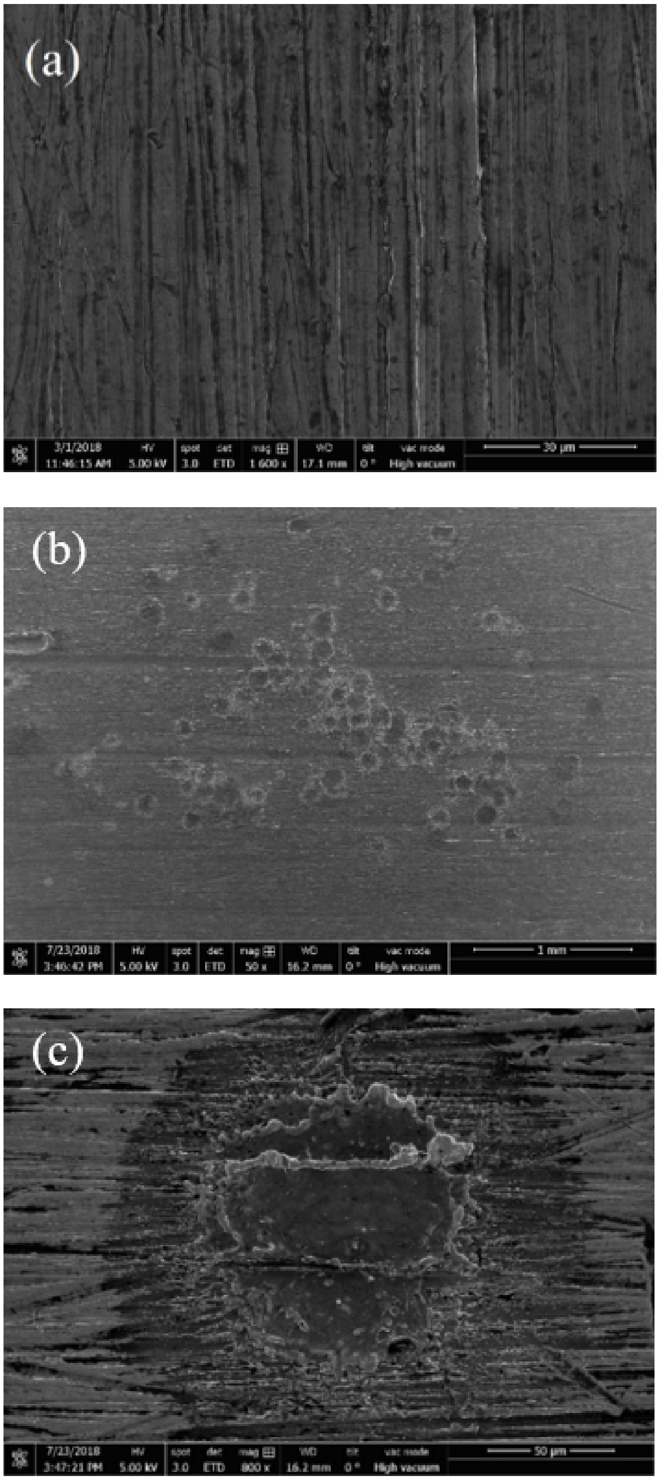

Figure 4.29: 700 μm gap (a) before plasma formation (30 μm scale – Vertical machining lines) and (b) after plasma formation (1 mm scale – Horizontal machining lines) as a result of 50 shots at a P.D-8.5 mm. (c) is a magnification of (b) to 50 μm scale (Horizontal machining lines).

Figure 4.29 shows SEM surface imaging for a 700 μm gap cathode. Figure 4.29a shows an off the lathe cathode at 30 μm scale, with surface imperfections of order 5-10 μm. Figure 4.29b is a post plasma formation image at the 1 mm scale. The image is characterized by large craters and clusters of craters resulting from plasma formation against a background of the original electrode surface profile. Figure 4.29c is an individual breakdown crater on the surface of the cathode at 50 μm scale. The blast crater seen in the image has nanometer roughness molten material in the center of the crater, and is surrounded by molten build up on the edge of the crater that forms microprotrusions on the order of 10-20 μm.

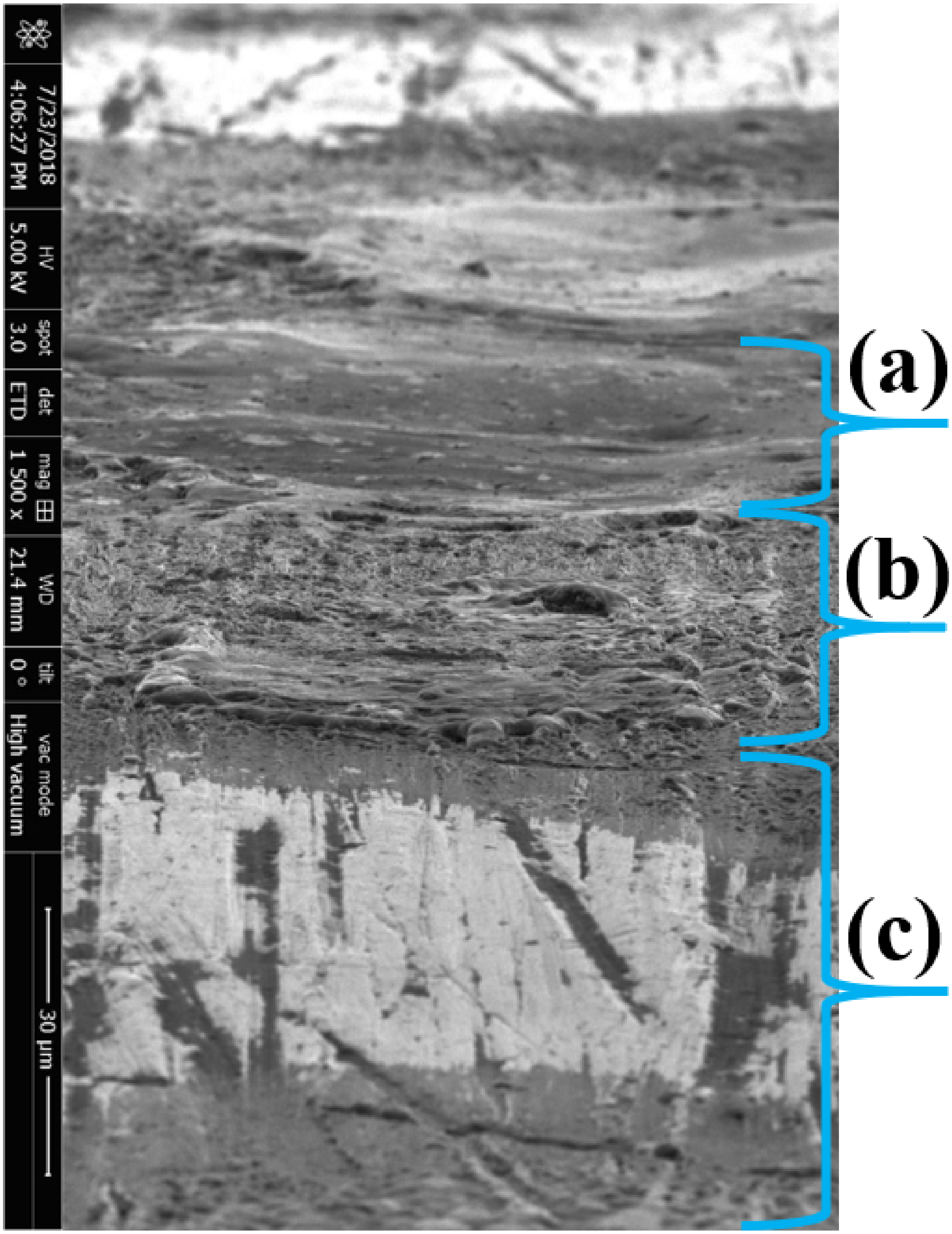

Figure 4.30: 700 μm gap side on and rotated x1500 magnification of a breakdown, with (a) smoothed crater zone, (b) molten splash created microprotrusions and (c) the undisturbed electrode surface.

Figure 4.30 shows an angled SEM image of the surface of the cathode centered on a breakdown crater for a 700 μm gap cathode. The image shows a detailed representation of the breakdown cartoon above. (a) Smooth molten crater that dips below the (b) explosive blast created microprotrusions, and (c) the undisturbed surface. From this image we can see that new microprotrusions can be formed by blast craters and molten blast buildup caused by plasma breakdown. Note, the craters shown in the SEM images may be the result of a single or large cluster [51] of microprotrusions exploding.

Using SEM imaging and the above description of explosive emission of microprotrusions we can investigate post-shot information of the surface of the electrodes used in the shot series to see how surface features change with changes in gap size. From Figure 4.30 we have measured post-shot microprotrusions that are of order 10-20 μm on both the anode and cathode, in height only. From this measurement we can estimate the percentage of the gap that is occupied by individual microprotrusions of this size, while not taking into account anything else about the geometry of the protrusions. Table 4.3 shows that for 150, 330, and 700 μm (large gaps) gap sizes the microprotrusion is a small percentage of the gap. For the 50, and 100 μm gaps sizes (small gaps) the percentage of the gap filled by the microprotrusions is significantly larger.

Table 4.3: Gap size compared to percentage of the gap that microprotrusions on the cathode and anode occupy. With a minimum protrusion size of 20 μm (10 μm on either side) and 40 μm (20 μm on either side).

20 μm Microprotrusions (Cathode + Anode)					
Gap size	50μm	100μm	150μm	330μm	700μm
Percentage of gap protrusion occupies	40%	20%	13%	6%	3%
40 μm Microprotrusions (Cathode + Anode)					
Percentage of gap protrusion occupies	80%m	40%m	27%	12%	6%

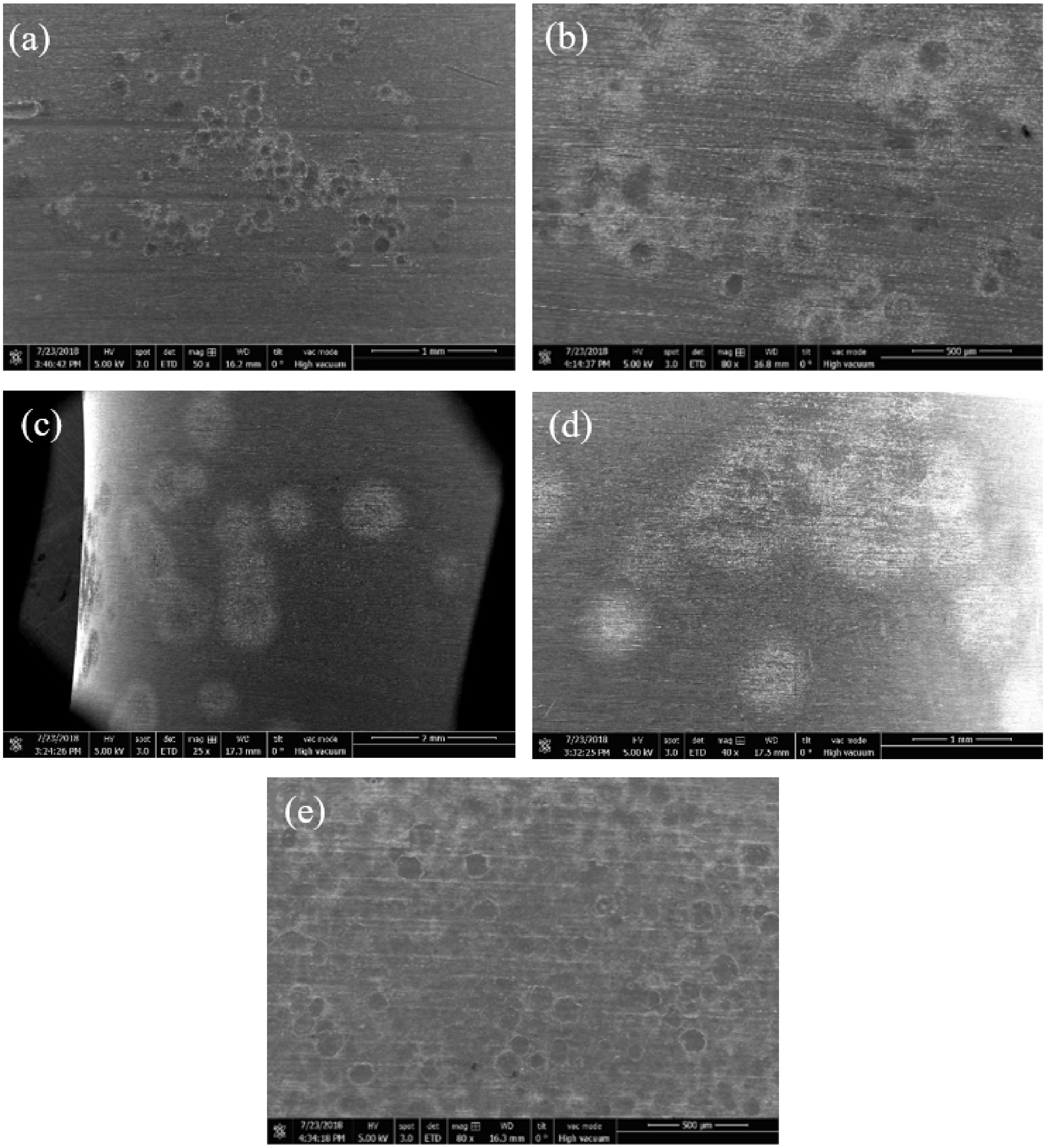

Figure 4.31: SEM imaging centered on blast regions for (a) 700 μm, (b) 330 μm, (c)150 μm, (d) 100 μm, and (e) 50 μm gaps. These are the results of 50 shots for each gap at P.D-8.5 mm (a-d) and 3.34 mm (e).

SEM imaging in Figure 4.31 shows a section of the electrode surface with breakdowns throughout for all gap size cathodes tested. From this we can use a simple in-house matlab code that I wrote to optically measure the diameter of each breakdown in the image and take an average, as well as estimate the number of breakdowns visible within the imaging area. Coupling this information we can then estimate on average what percentage of the total penetrated surface area the breakdown surface deformations cover (Figure 4.32).

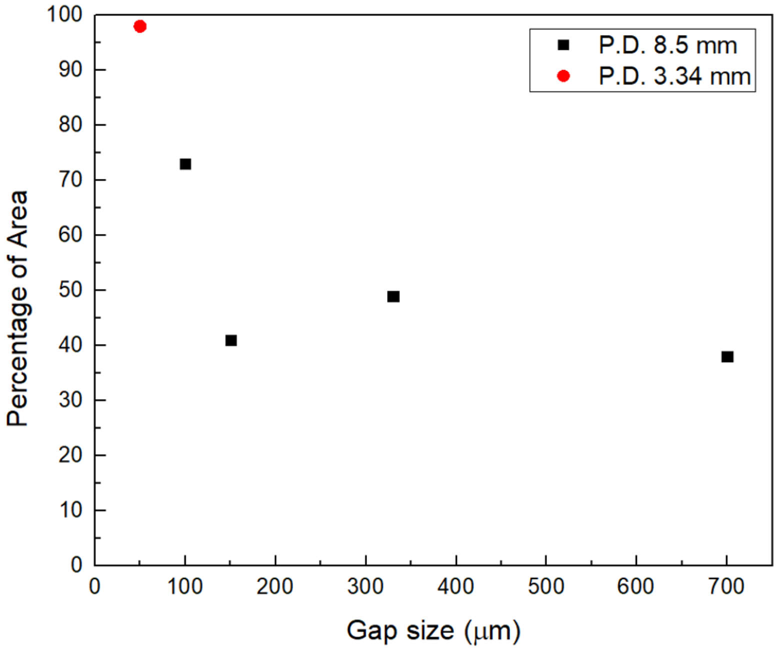

Figure 4.32: Average percent area occupied by breakdowns for all gap sizes tested. With black squares showing data collected at P.D-8.5 mm and the red square showing data collected at P.D-3.34 mm.

Figure 4.32 shows the average percent area occupied by breakdowns for all the gap sizes tested in the shot series. Note, for simplicity we are assuming that we have no overlap in our breakdown craters so the values presented are higher than would be the case for overlapping craters. The percent area occupied by the breakdowns for the large gaps is between 40-50%. The percentage of area occupied by the breakdown craters generally decreases with decreasing blast diameter and increasing gap size (Figure 4.31a-c). The microprotrusions that form in this case take up 3-27% of the gap (Table 4.3), with the remaining 50-60% of the surface area being occupied by off the lathe protrusions of 5-10 μm. For the small gaps tested the percentage of the area that the breakdown craters occupy increases significantly to 70% for the 100 μm gap and 97% for the 50 μm gap. The large increase is due to the increased number of breakdowns observed in SEM images of the cathode (Figure 4.31d-e). The microprotrusions that form occupy 20-80% of the gap (Table 4.3), with the remaining surface (3-30%) of the surface being off the lathe protrusions of 5-10 μm. Furthermore, the surface topology of the breakdowns in SEM imaging of the 100 μm (Figure 4.33) and 50 μm (Figure 4.34) cathodes are characterized by overlapping smoothed breakdown areas.

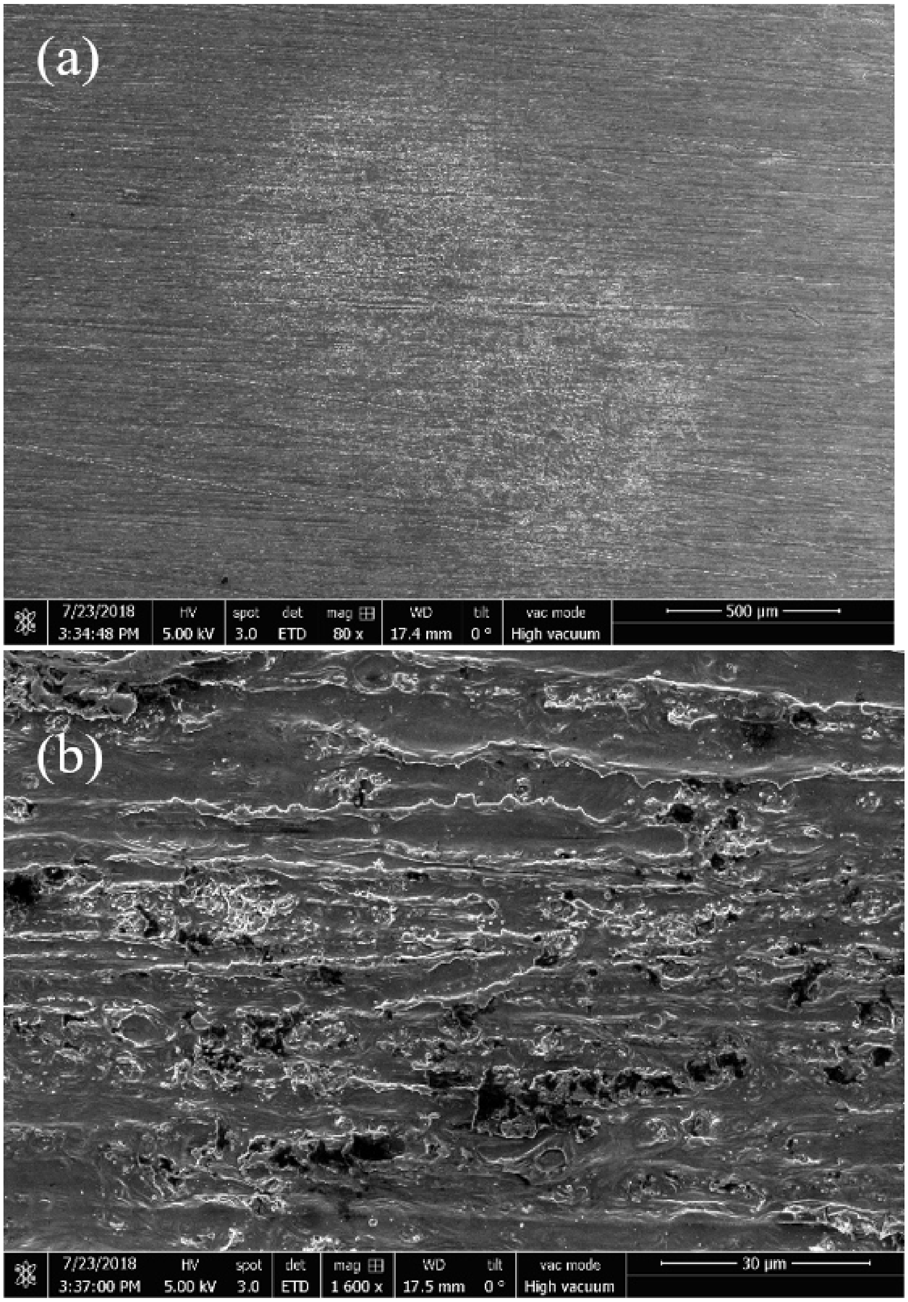

Figure 4.33: 100 μm gap centered on a large breakdown at scales of 500(a), 30(b) μm.

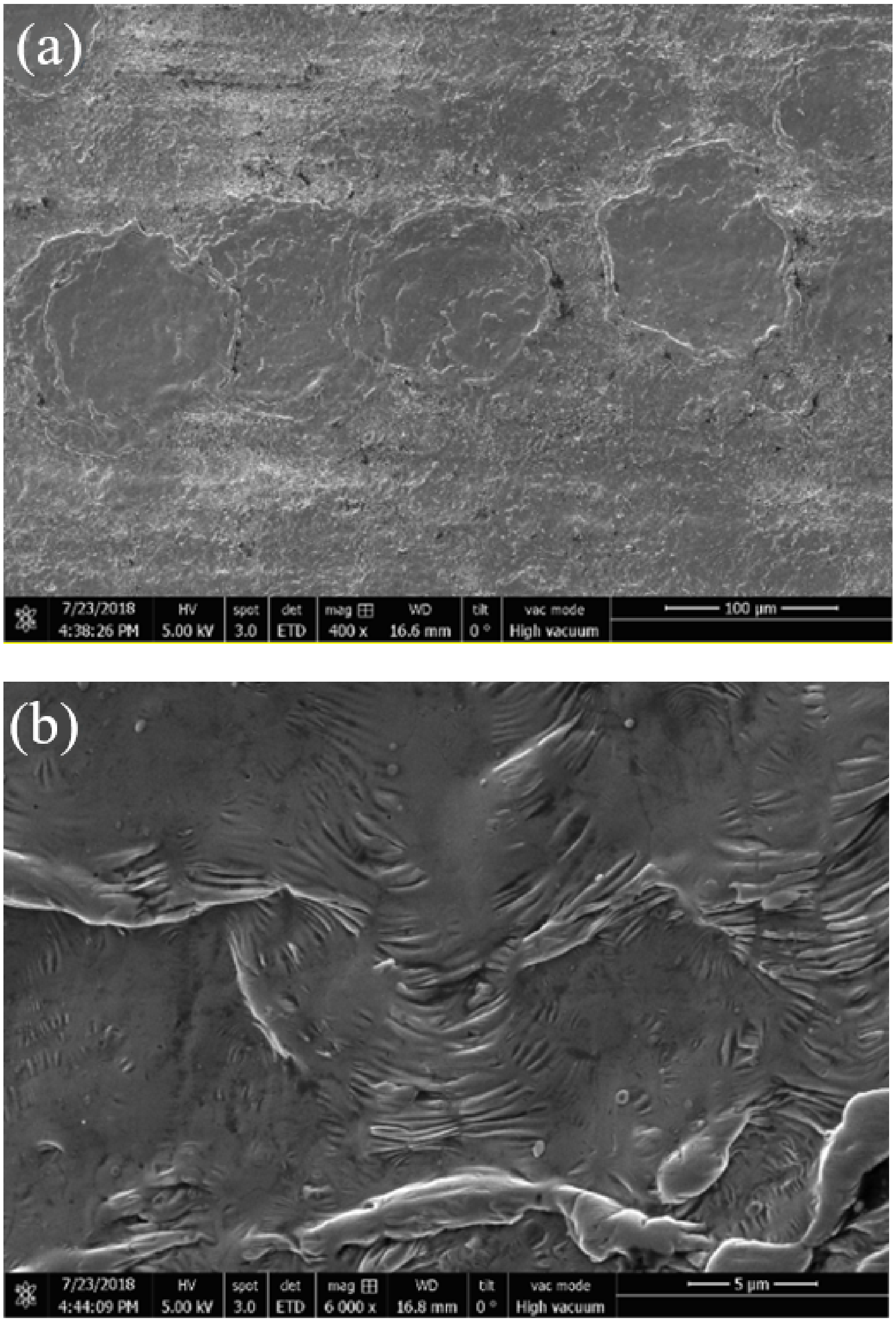

Figure 4.34: 50 μm gap centered on a large cluster of breakdown at scales of 100(a), 50(b) μm.

If we then compare the observed behavior at the surface, via our SEM imaging, for the gap sizes tested, we can then infer which factors are dominant in changing the enhancement factor and driving breakdown. For the large gap sizes tested we see from SEM imaging of the surface that the cathode surface is not dominated by the creation or destruction of microprotrusions, and protrusions that do form from explosive breakdowns take up only a small portion of the gap. This indicates that the increasing enhancement factor with increasing penetration depth is dominated by the increasing surface area of the electrode with increasing penetration depth that adds new protrusions to the gap. Physically for the large gap sizes tested, increasing enhancement is likely dominated by changes in geometry via changes in penetration depth rather than explosive breakdown induced changes to the surface. For the small gaps tested, SEM imaging shows that the surface is dominated by the creation and destruction of microprotrusions via explosive breakdowns, which results in a gap that is significantly altered, and a surface that is smoothing. This behavior is represented by the decreasing enhancement factor with penetration depth. Physically for a gap that is dominated by variations in microprotrusions, the introduction of new protrusions with increasing penetration depth does little to increase the enhancement factor is dominated by significant alterations of the surface created by many explosive breakdowns.

We can explore the relationship between surface area and enhancement factor by plotting the electrode surface area and enhancement factor versus the penetration depth for all gap sizes tested (Figure 4.35). As the gap size decreases, the change in surface area value is small compared to the other dimensions, while the enhancement factor trends vary significantly. The plots of surface area for each gap size are normalized to the enhancement factor at penetration depth of 2.5 mm, which is the region we have identified previously as ’area effect’. The slope represents the trend expected if the enhancement factor is dominated by the change in surface area.

When looking at the 700 μm gap (Figure 4.35a), the enhancement factor increases with penetration depth and follows the increasing surface area with penetration depth closely. As gap size decreases, the measured enhancement factor deviates further from the trend of the surface area (Figure 4.35b-e). This indicates that the surface area is a dominant driving factor for the enhancement factor for larger gaps, but plays an increasingly less significant role as the gaps become small. This is directly in line with the above observations and discussions.

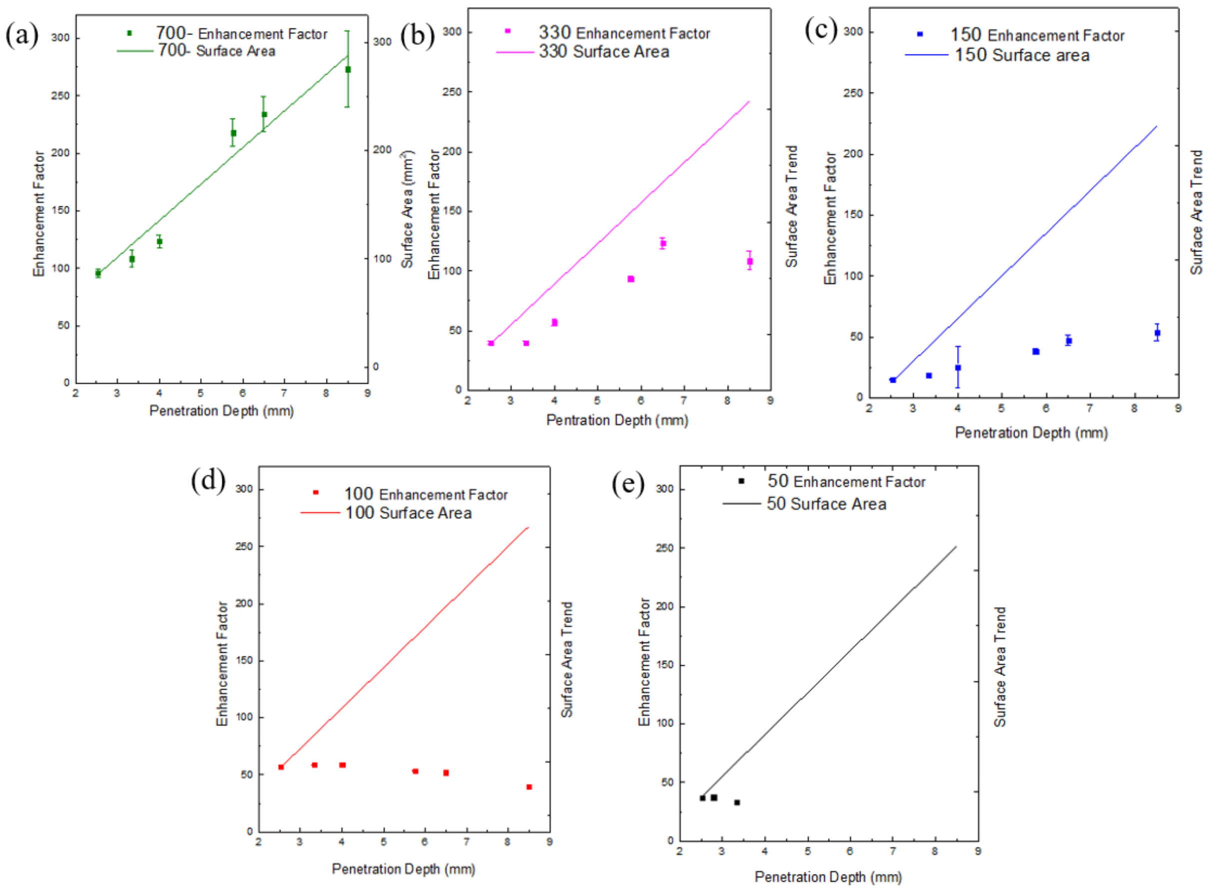

Figure 4.35: Electrode surface area and enhancement factor for (a) 700 μm, (b) 330 μm, (c)150 μm, (d) 100 μm, and (e) 50 μm gaps vs. Penetration Depth. With the solid lines representing the surface area of the penetrated electrode, and the solid square being the enhancement factor value

In this section we have shown that the enhancement factor for a coaxial gap changes with varying gap sizes and penetration depths. This change is likely dominated by the electrode geometry, area of the penetrating electrode and the creation and destruction of microprotrusions that are large compared to the cathode surface finish. It is important to note once more, these are not the exclusive driving forces in changing the average enhancement factor value. Asymmetric distribution of breakdown in individual shots, a slightly varying work function, and conditioning of the electrode during the 50 shots all play a role in the changing of the enhancement factor value. Furthermore, due to the rep-rated nature of these experiments, the results may not perfectly apply to single shot experiments.

For experiments on vacuum gaps of 150 μm, 330 μm, 700 μm, we see an initial edge effect in the average enhancement factor with increasing penetration depth, this is followed by an increase at depths greater than 2.53 mm. This increasing in average enhancement factor is caused by an increase in microprotrusions that are likely due to the geometry of the electrode and the increase in area for breakdowns to occur. Where microprotrusions created by the explosive nature of breakdown formation in the vacuum gap remain small compared to the gap size and take up 40-50% of the total surface area. For 50 μm and 100 μm gap sizes, we see first that the average enhancement factor for these two gap sizes is smaller than the larger gap sizes tested for higher penetration depths. Second, we see the same edge effect behavior at a penetration depth smaller than 2.5 mm, after which there is a brief increase followed by a decrease in average enhancement factor with penetration depth. This behavior is likely due to the increased number of breakdowns creating and destroying microprotrusions and occupying a majority of the total surface area of the electrode. These are significant topological changes to the surface that occupy a majority of the gap. In the region of these changes, the increased number of overlapping breakdowns cause the surface to smooth, which leads to a decrease in microprotrusion height and enhancement factor. These trends are substantiated by the presented imaging diagnostics.

4.3 Coating Experiments

In the previous section we have shown the influence the gap size, the penetration depth, the surface area, and the surface of a material have on breakdown characteristics using Fowler-Nordheim analysis. In this section we will investigate experiments geared towards understanding how the work function of a material influences breakdown in a coaxial gap.

4.3.1 Coating at 1 MA Comparison to Coating SEM Imaging

With the goal of investigating the influence on breakdown formation from the work function and surface profile of various metals, an experimental series was devised in which the head of Z-scale aluminium liners would be coated with materials of different work functions via dip coating and electroplating, fired at 1 MA on COBRA, and compared to non-coated results. COBRA current pulse (1 MA, 100 ns or 250 ns) is equivalent to the pre-pulse and 5-10 ns of the Z-current pulse (Figure 4.36) Figure 4.37 shows a simple diagram of the load region and the coating of the head of the liner.

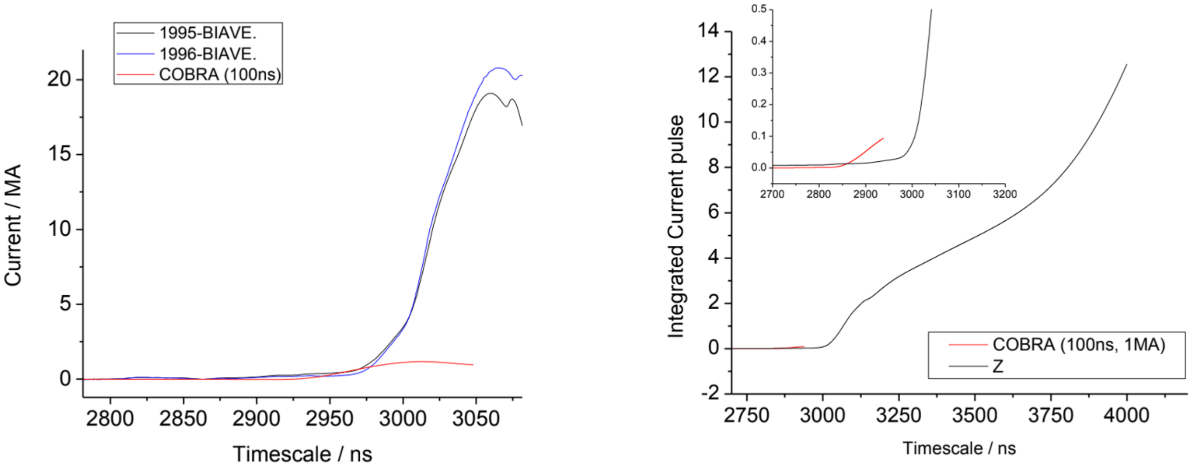

Figure 4.36: Plot of comparison of Z and COBRA (left) drive current and (right) integral curves of the drive current

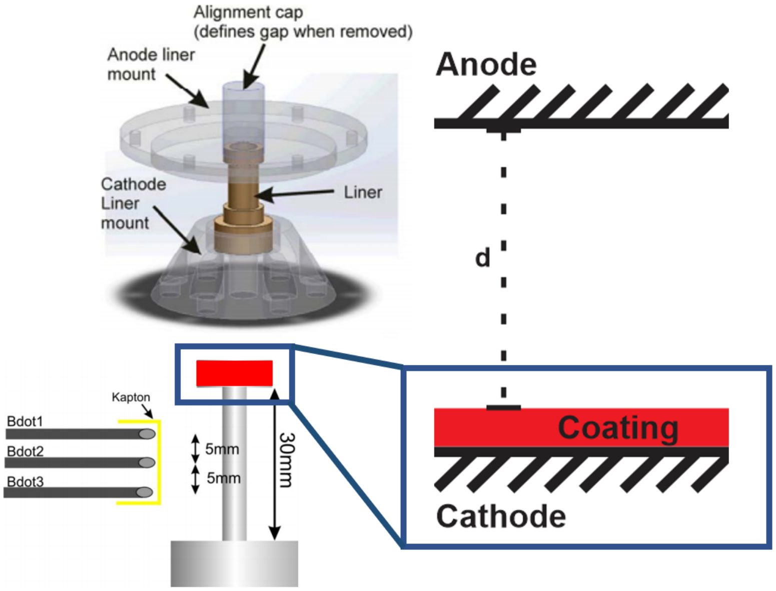

Figure 4.37: COBRA load with liner specifications and coating diagram

All targets were machined at Cornell using aluminium alloy and coated with thicknesses on the order of 10 μm so as to not affect the gap size. No special polishing was applied to the outer surface after machining. The targets' dimensions and design mimic the Z-targets, having an an outer diameter of 8.16 mm, a thickness of 300 μm, and a height of 40 mm. The targets connect at the cathode and form a 200 μm radial gap with the anode plate. The cathode gap is held at 200 μm for the duration of the shot series, and is achieved through the us of an alignment cap (Figure 4.37). Targets have a surface finish of 5-10 μm as seen in SEM surface imaging of a non-coated aluminium liner head (Figure 4.38a). Subsequent SEM images show the surface finish when a coating is applied through electroplating and dipping various metals to the machined electrodes.

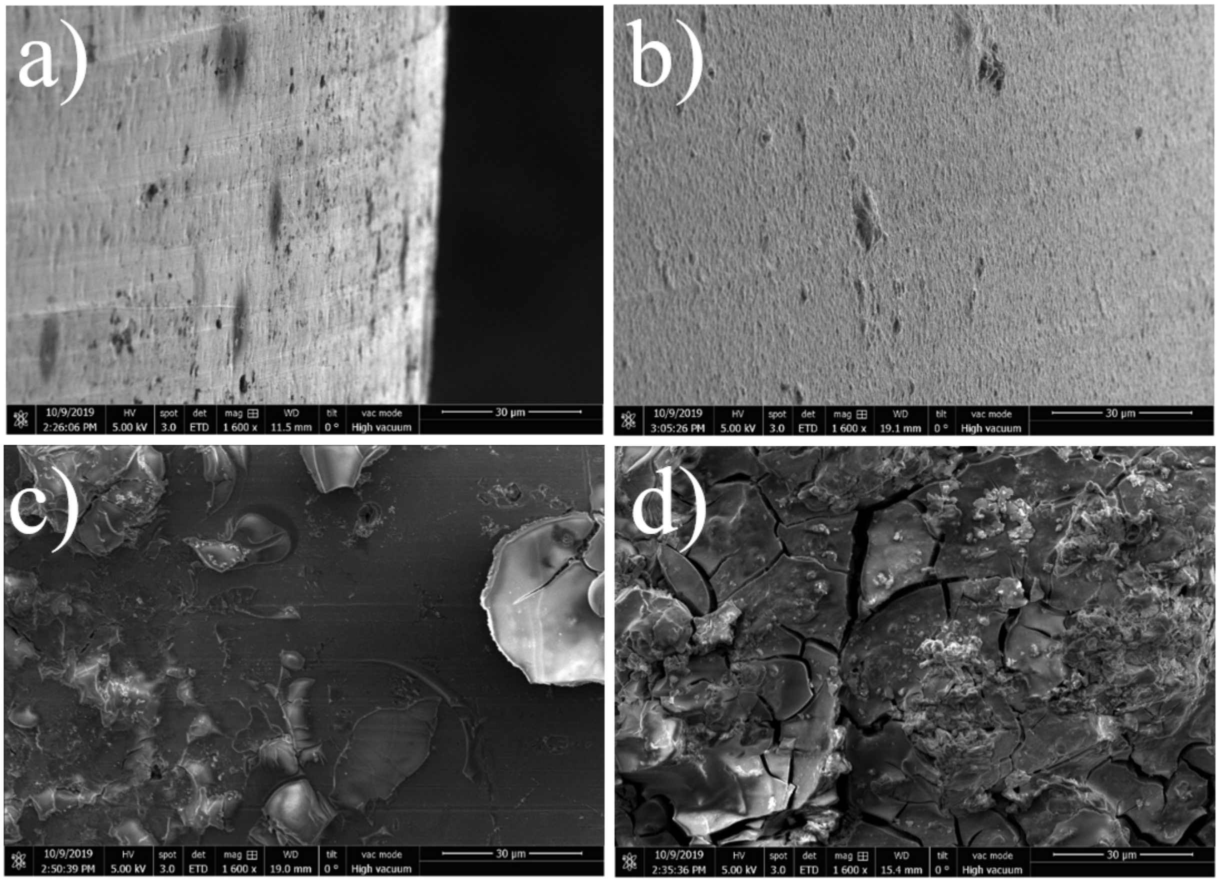

Figure 4.38: a) Aluminium no coating, b) Aluminum – Aerodag-G coating, c) Aluminium - Gold coating, d) Aluminium – Copper coating.

The coating materials for this shot series were as follows; Gold, Copper, Aerodag- G

(Graphite) with the corresponding work functions listed in Table 4.4. SEM images (Figure 4.38) of the surface of coated electrodes show distinct differences between the materials. With the Aerodag-G dip coating characterized by smooth sub micrometer roughness finish (Figure 4.38b). The Gold (Figure 4.38c) coated surface is characterized by large irregular surface imperfections on the order of >10 μm with interspersed regions of nanometer scale roughness. The surface of the Copper (Figure 4.38d) coated electrode is characterized by large surface imperfections and flakes on the order of >15 μm, while the surface of these flakes are on the order of sub nanometer roughness.

Table 4.4: Work functions of materials used in coating experiments

Material	Work function (eV)
Aluminium	4.3
Gold	5.1
Copper	5.0
Aerodag-G (Graphite)	4.62

The diagnostic setup for the series included 12-frame end-on gated optical imaging to monitor plasma formation in the gap, side on laser interferograms and a 12-probe B-dot array to monitor current distribution about the length of the liner through the duration of the current pulse (as seen in previous sections).

Figure 4.39 shows the framing (red square) of the 12 frame camera top-down on the anode plate centered on liner head and the gap. The zoomed region shows a single frame of the camera (-7 ns), with the liner, anode, and magnetic field probes orientation labeled. With this we can investigate the breakdown initiation and plasma emission growth in the gap at 10 ns steps through the duration of the current pulse.

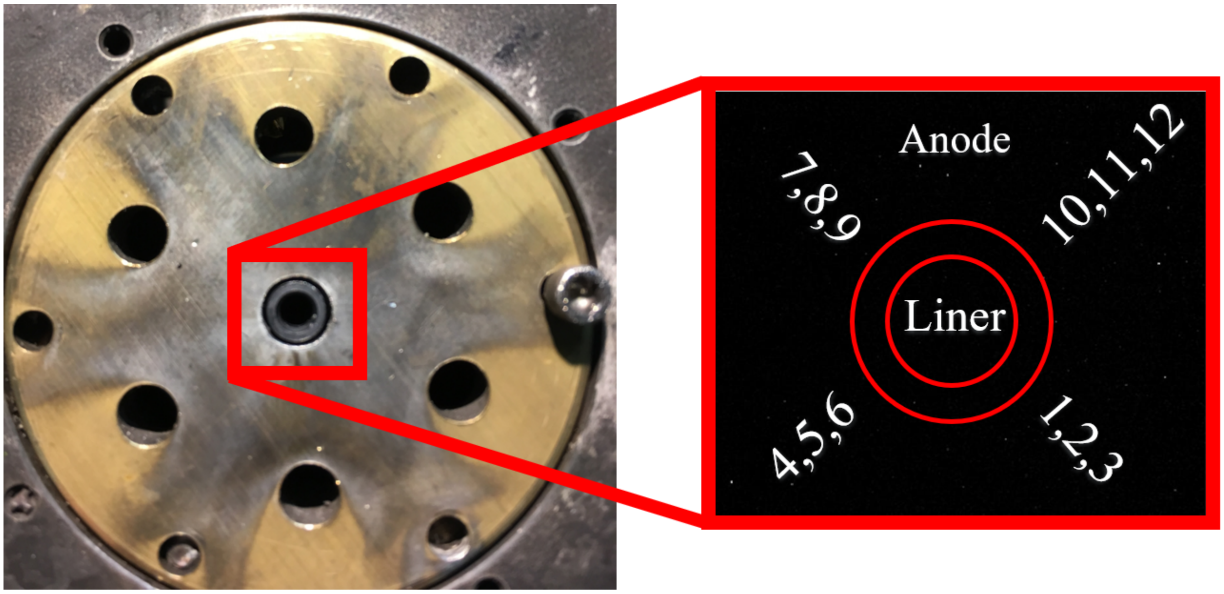

Figure 4.39: 12 frame camera framing of the gap with probe locations labeled.

Figure 4.40 shows 8 of the 12 gated optical images of a 200 μm gap, four frames are outside the current pulse and not shown [13]. Emission from the plasma in the gap forms at 17 ns, this is a typical time for breakdown emission to form for non-coated aluminium liners. As the frames move forward in time and the current continues to rise we see new localized spots of plasma forming in the gap at varying intensities (that increase and decrease), as well as localized spots spreading and fading out. Note that the plasma while abundant, does not ever fill the entirety of the gap through the duration of the current pulses shown (77 ns).

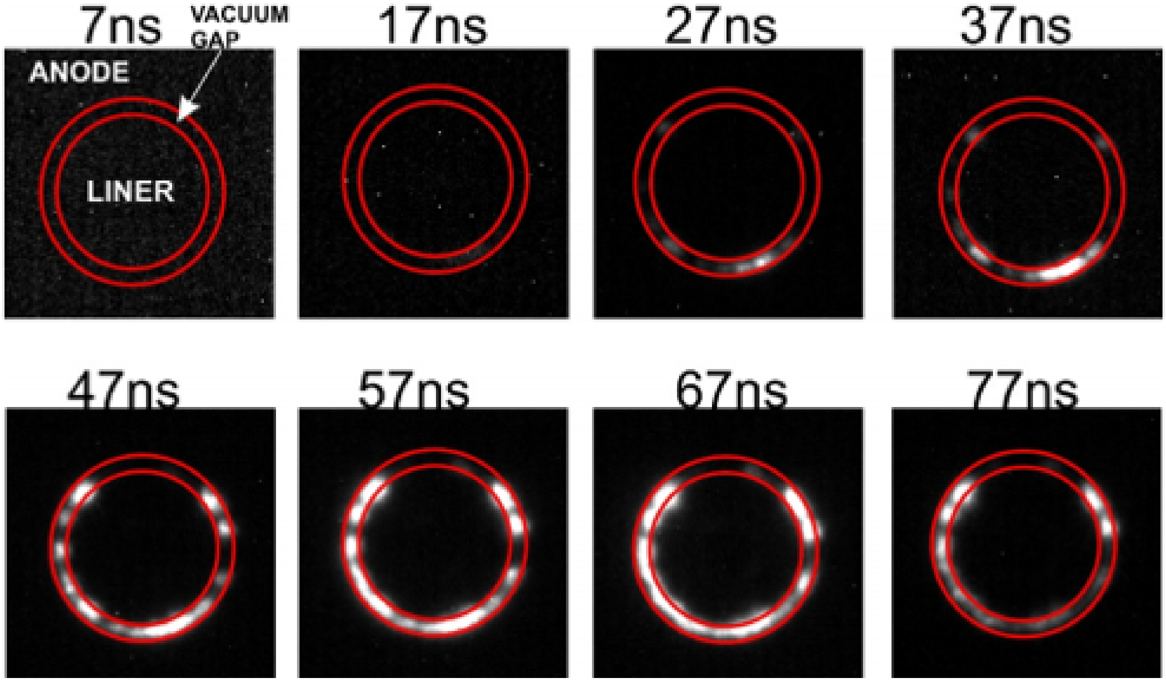

Figure 4.40: Gated optical images (10 ns) for a non-coated coated aluminium liner head, for a 200 μm gap

If we then examine the integrated magnetic field signals in Figure 4.41 we see firstly that the magnetic field signals do not overlap for the duration of the current pulse, which as described in the previous section indicates asymmetric current density distribution along the axis of the liner that persist through the duration of the current pulse. Again, we can then correlate asymmetry in breakdown formation in the gap to asymmetry in current density distribution in the liner.

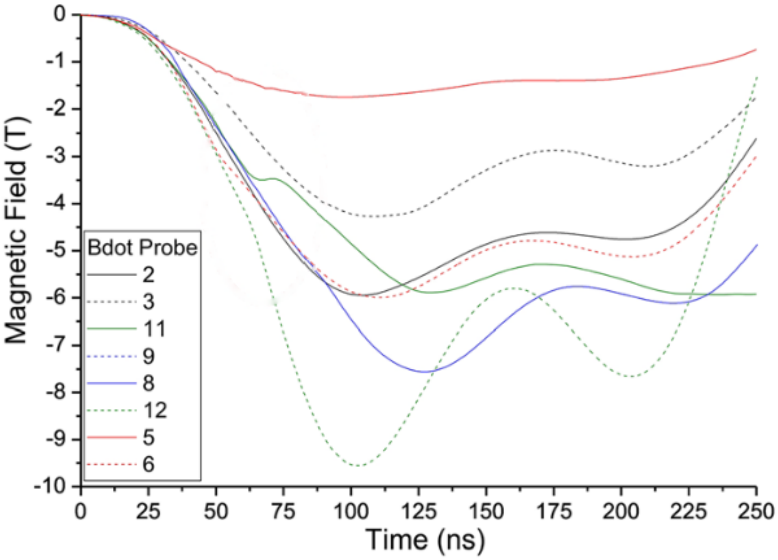

Figure 4.41: Magnetic field array traces for the non-coated aluminium liner head, 200 μm gap.

Figure 4.42 shows 11 of 12 frames of gated optical images for a copper coated aluminium liner head for a 200 μm. A very faint breakdown initiation emission can be seen at 30 ns (just right of center) nearest the 10, 11, 12 probe location. The emission spot grows gradually from 30 ns to 60 ns before stopping. The offset emission persists through the current pulse duration. We can then correlate the emission behavior in the gap to the magnetic field probe traces in Figure 4.43. Immediately we see once more that the traces are not overlapping, indicating asymmetric current density distribution, with probes 8, 10 measuring the largest fields which correspond to the asymmetric emission location.

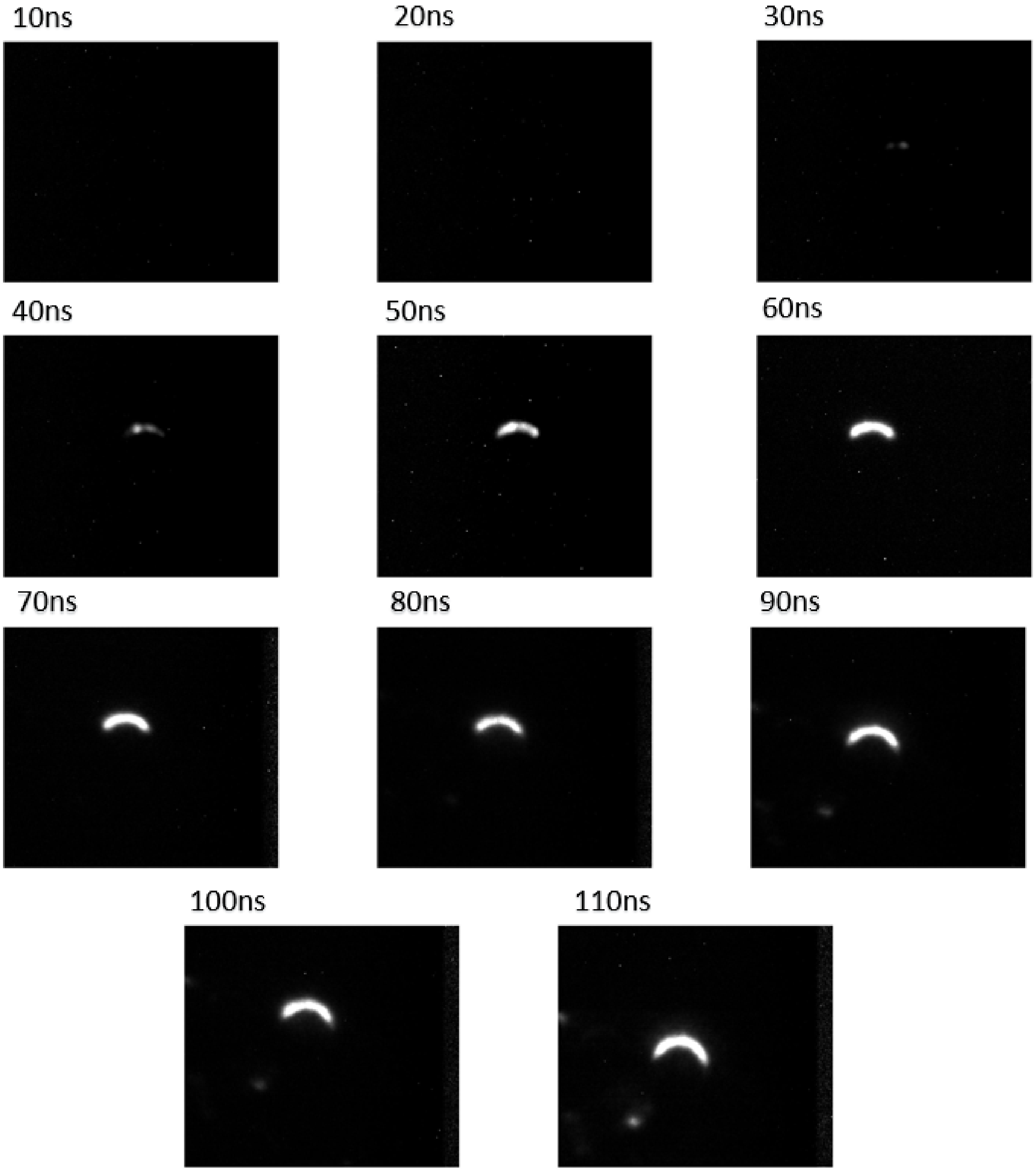

Figure 4.42: Gated optical images (10 ns) for a copper coated aluminium liner head, for a 200 μm gap.

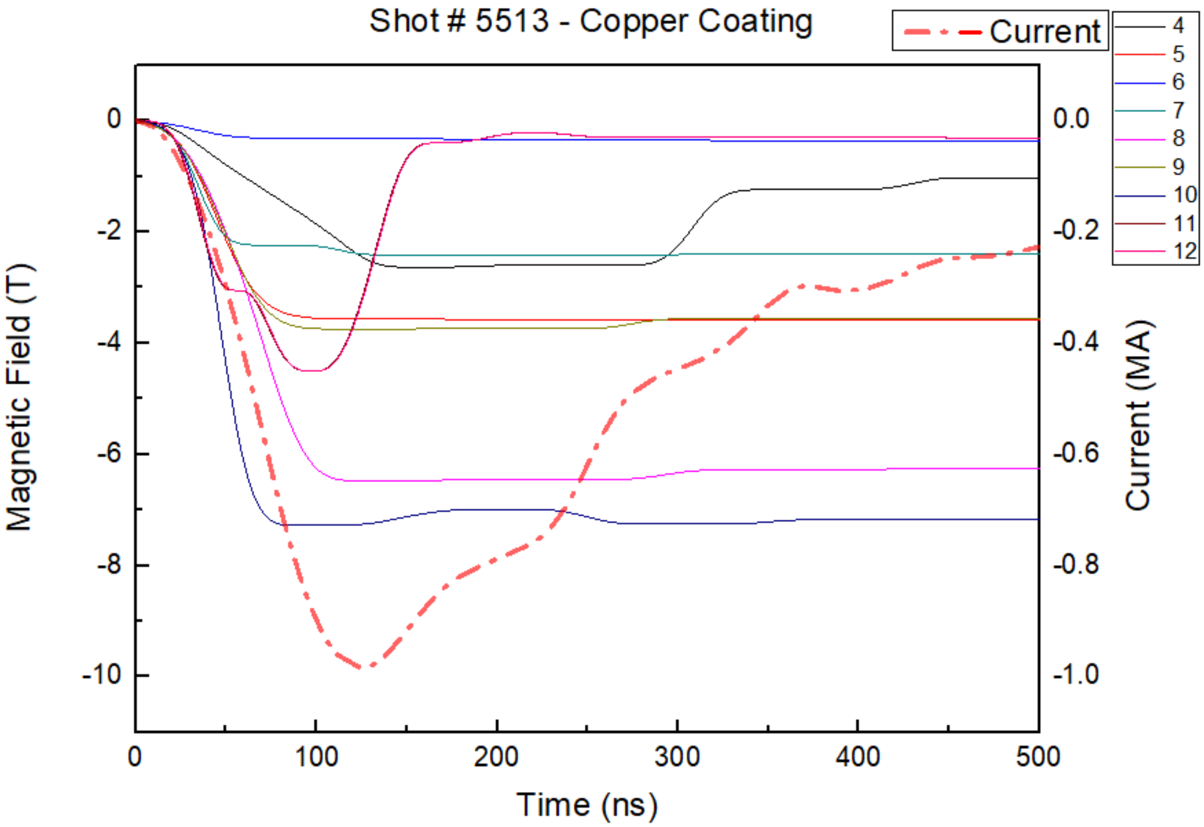

Figure 4.43: Magnetic field array traces for the copper coated aluminium liner head, 200 μm gap.

Figure 4.44 shows 11 of 12 frames of gated optical images for a gold coated aluminium liner head for a 200 μm gap. Initiation emission is seen at 40 ns near 10, 11, 12 and 1, 2, 3 that remains in the location for the duration of the current pulse and a late time (90 ns) secondary localized emission forming near 7, 8, 9 probes. The results of this secondary breakdown can be seen in the corresponding magnetic field probe traces (Figure 4.45), where more probes are moving towards the highest value of 8+ Tesla. Again, early offset in gated optical images–even with multiple breakdowns– leads to a non-uniform distribution of magnetic fields, and thus non-uniform current density distribution along the liner.

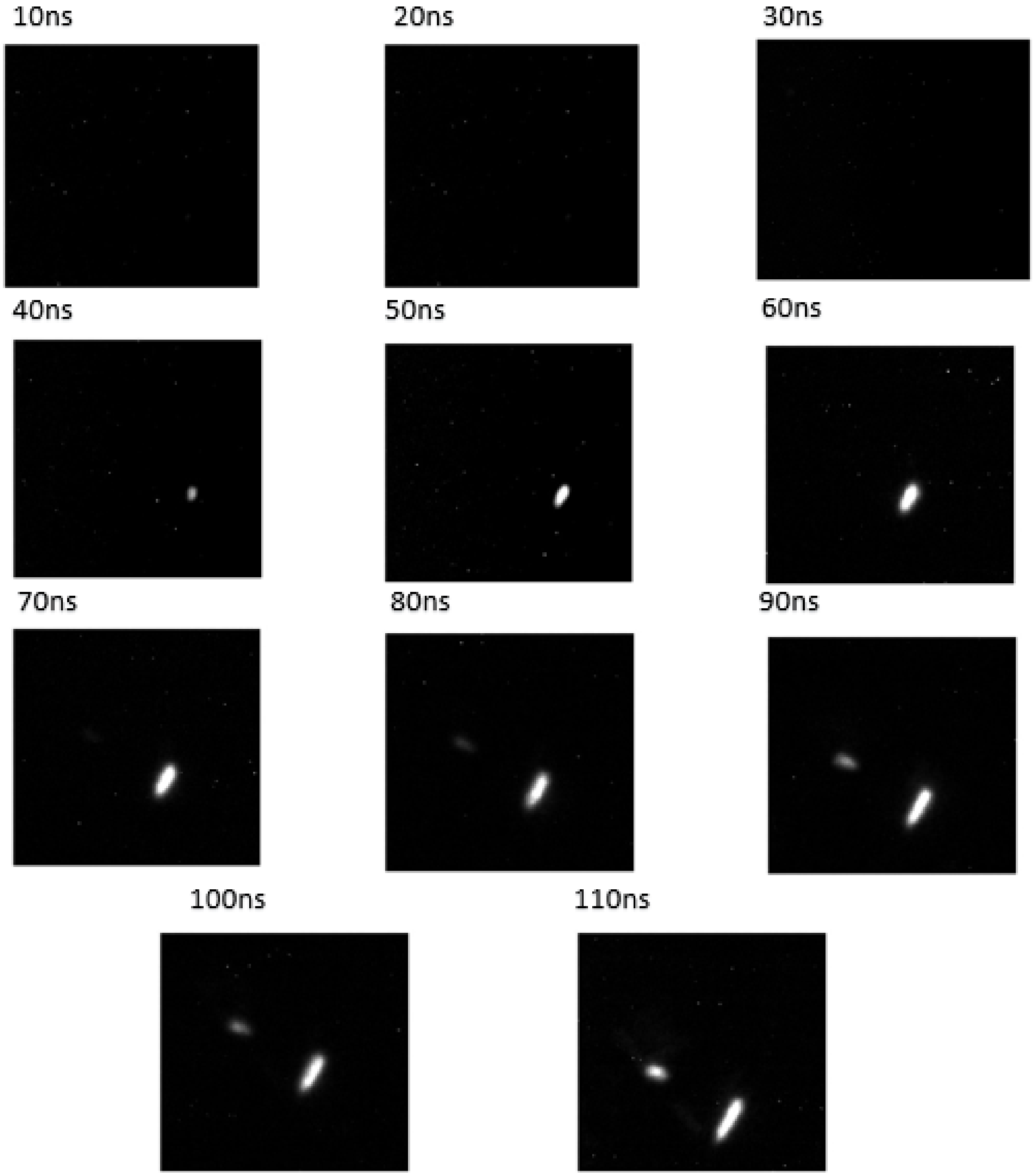

Figure 4.44: Gated optical images (10 ns) for a Gold coated aluminium liner head, for a 200 μm gap

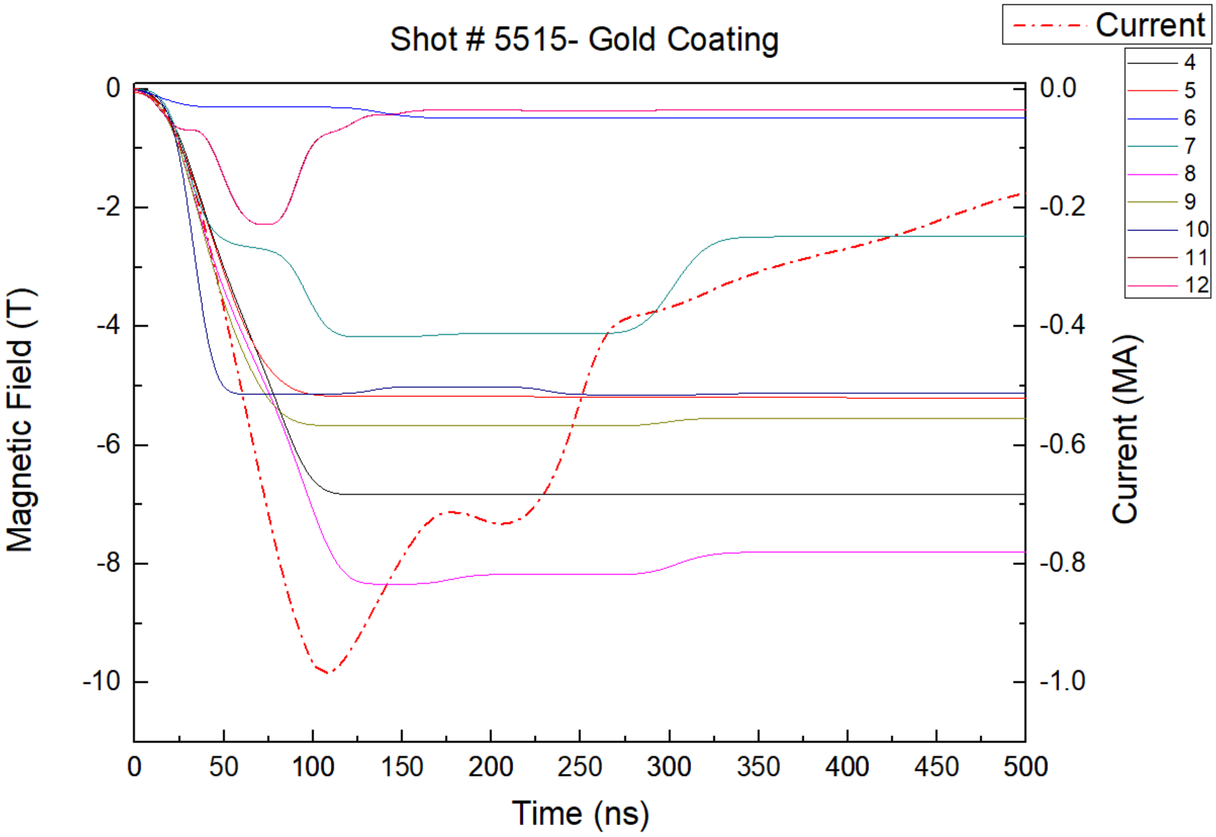

Figure 4.45: Magnetic field array traces for the gold coated aluminium liner head, 200 μm gap.

Figure 4.46 shows 11 of 12 frames of gated optical images for graphite coated aluminium liner head for a 200 μm gap. Initiation emissions is seen at the earliest frame taken (10ns) and is nearly uniform. As the current pulse rises, the emission in the gap expands and fills completely by 80 ns and remains fully uniform through peak current. This is the first time a uniform gap has been seen in my research. Corresponding magnetic field traces (Figure 4.47) follow one another very closely, overlapping in most cases. This indicates a near uniform current density distribution in the surface of the liner, while asymmetry still exists the vacuum gap fills rapidly from the onset of the current drive and slowly becomes more uniform towards peak.

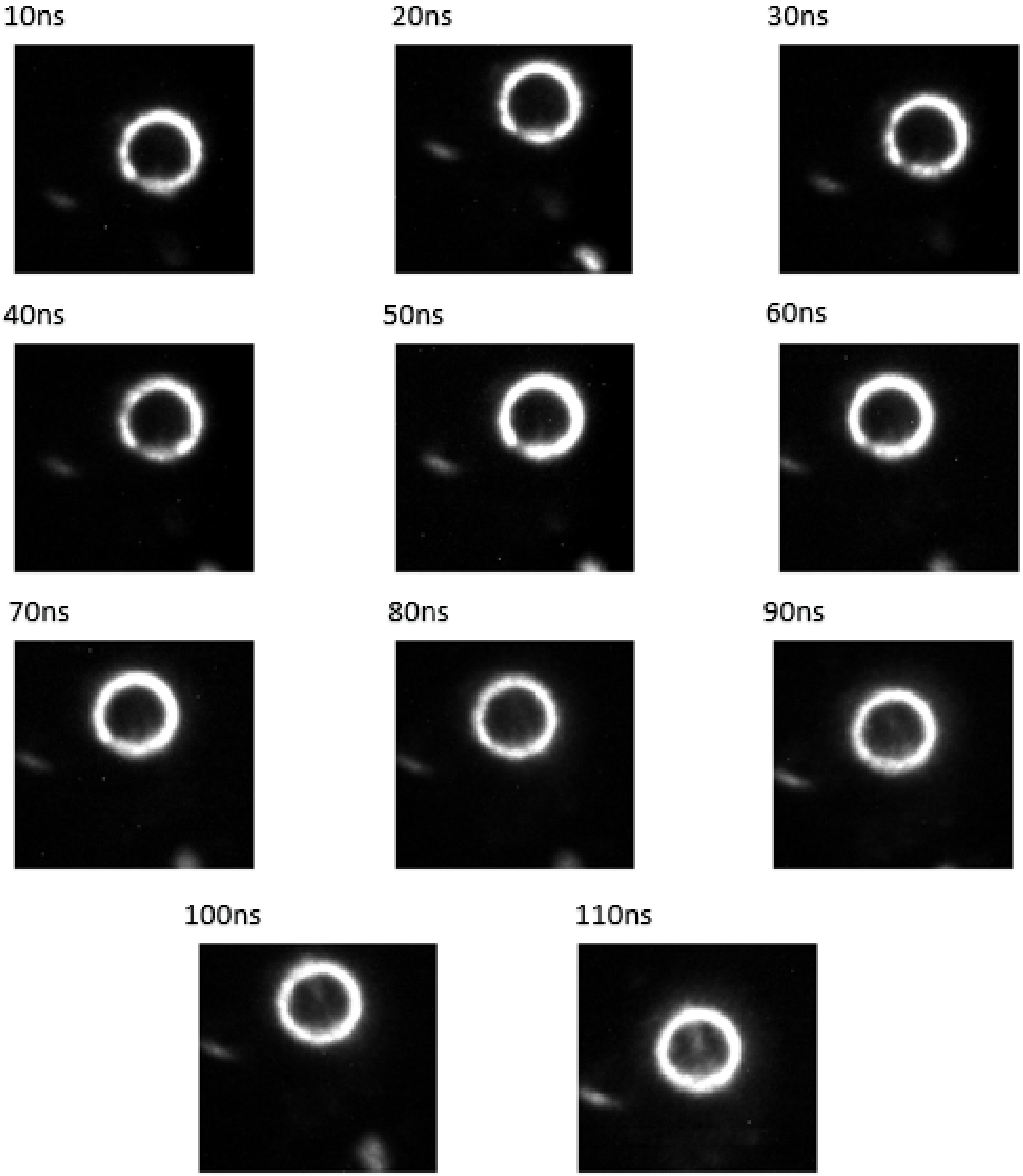

Figure 4.46: Gated optical images (10 ns) for a Aerodag-G coated aluminium liner head, for a 200 μm gap

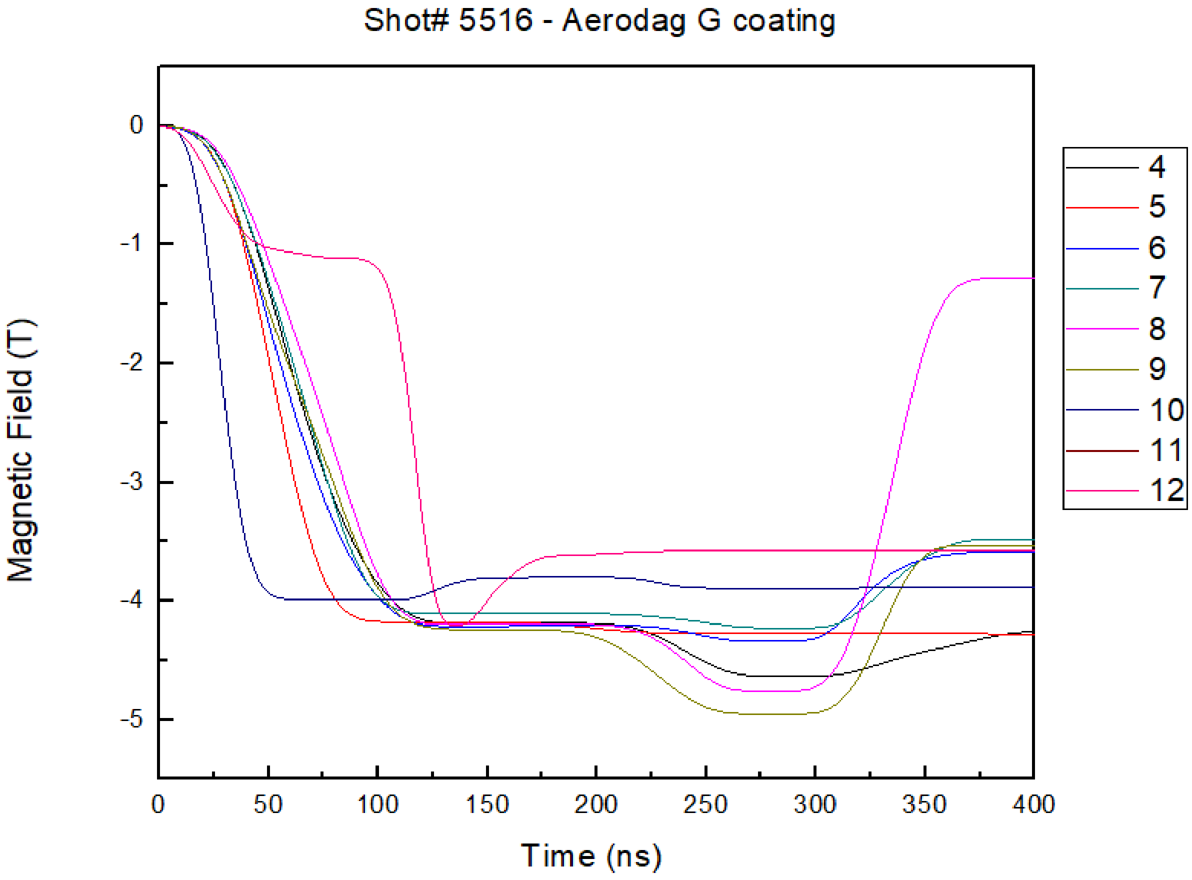

Figure 4.47: Magnetic field array traces for the graphite coated aluminium liner head, 200 μm gap.

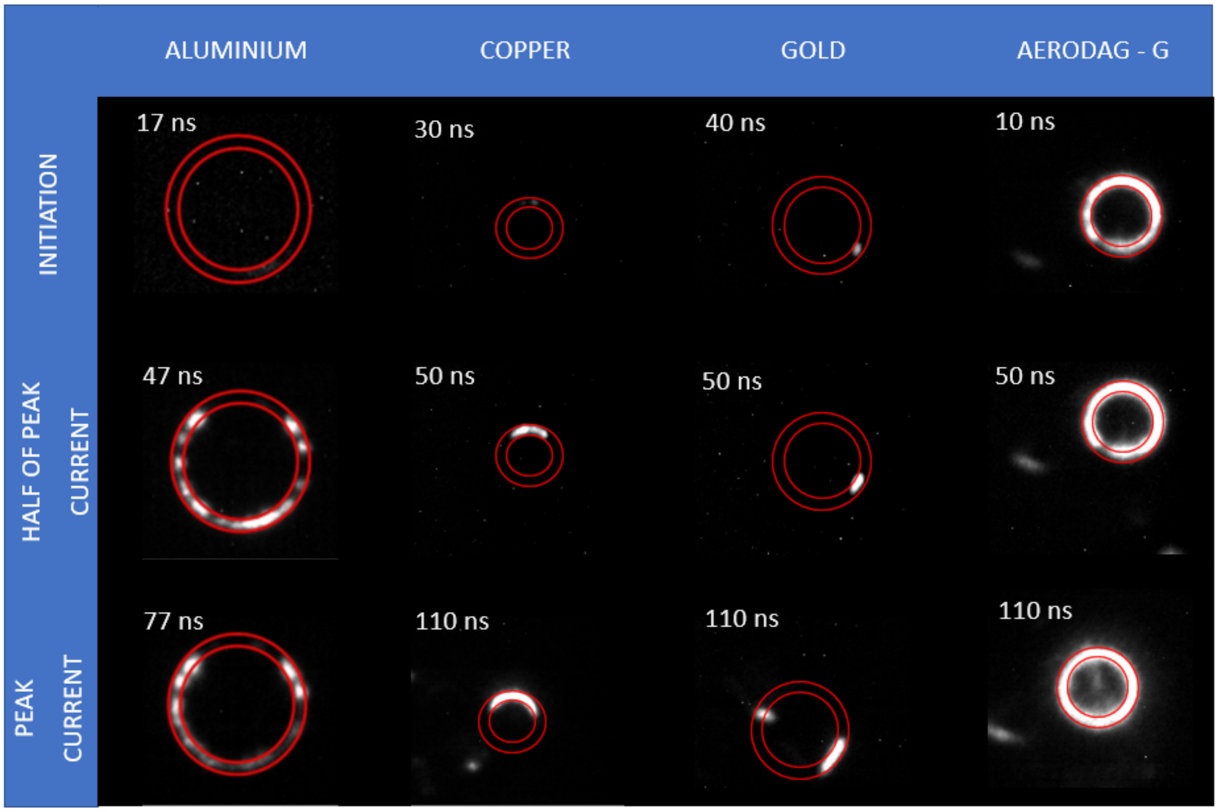

Figure 4.48: Magnetic field array traces for the graphite coated aluminium liner head, 200 μm gap.

In order to understand the effects the work function has on breakdown formation and distribution for each of the coatings we compare the gated optical emission images at initiation, half peak, and peak current (Figure 4.48). At initiation we see that Aerodag-G nearly fills at 10 ns into the current pulse, the non-coated aluminium gap has a small faint breakdown that forms at 17 ns, Copper emission first forms at 30 ns into the current pulse, and gold at 40 ns. With respect to aluminium, our base line for this comparison, that is an initiation difference of -7 ns for Aerodag, +13 ns for Copper, and +23 ns for Gold. This initiation time difference means that Aerodag is more likely to breakdown, and copper and gold are less likely to breakdown (increased hold off on initiation). If we then compare the work functions of the materials from Table 4.4 we see that Copper and Gold have work functions of 5.0 eV and 5.1 eV respectively, these are .7 eV larger than aluminium. This increased work function could play a role in the increased hold off, on initiation time of breakdown. When comparing aluminium to Aerodag-G, we see a 0.32 eV difference, yet time of initiation is a -7ns difference between them. To understand this discrepancy in the trend of increased work function and increased initiation hold off we look more closely at pre-shot SEM surface images of the coating surface.

As stated above with respect to Figure 4.38, SEM images of the coated electrodes show vastly different surfaces. Copper (Figure 4.38d) has multiple large surface imperfections on the order of $>15\ \mu$m, Gold (Figure 4.38c) has large irregular surface imperfections on the order of $>10\ \mu$m with interspersed regions of nanometer scale roughness. Aerodag-G (Figure 4.38b) has the most uniform surface finish of the coatings with sub μm scale surface imperfections that are relatively uniform distributed across the surface.

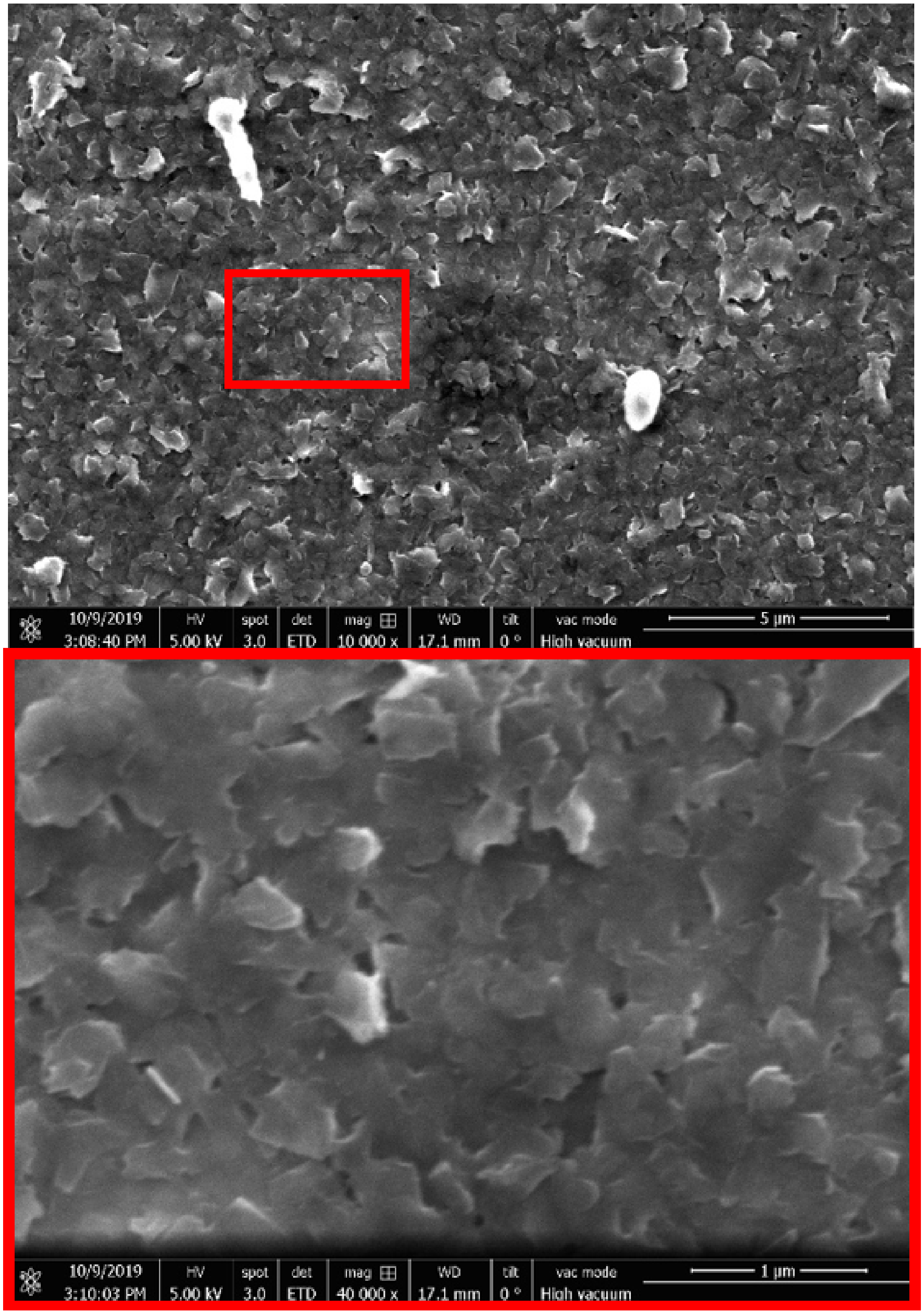

Figure 4.49: SEM imaging of Aerodag-G coated electrode x10000 magnification (left) and x40000 magnification (right)

Investigating the Aerodag-G coating further via SEM, the surface profile becomes far rougher. At x10,000 and x40,000 magnification, it is clear that the surface imperfections are sub μm scale are abundant. The surface imperfections also have a flaky texture in appearance. These surface imperfections could be driving uniformity in the Aerodag-G coated shot. This idea is substantiated by the literature on breakdown formation due to surface microprotrusions, as well as material assisted breakdown. The general idea is that at some height on a microprotrusion emitter tip, the current density heats the tip to a temperature hot enough to cause it to explode and propel into the gap via JxB force. The majority of the material ejected into the gap is ionized, while the remainder is transferred to the surface of the cathode and anode. With the significant increase in number of microprotrusions, the number of ejected emitter tips has increased and thus there is more material in the gap to be ionized. A simple diagram of this is shown in Figure 4.50, which shows the red blown-off material floating in the gap, shortening the distance between cathode and anode, which reduces the required electric field to cause a breakdown. Previous work on COBRA [14] posited that for a single plasma channel on COBRA that forms in a coaxial gap of 400 μm the density, temperature change slowly, and the rising current causes an increase in electron drift velocity, which triggers ion acoustic instability and an increase in resistivity. This increase in resistance causes a voltage drop increase across the electrodes, which in turn leads to an additional breakdown and plasma channel at a different location in the gap.

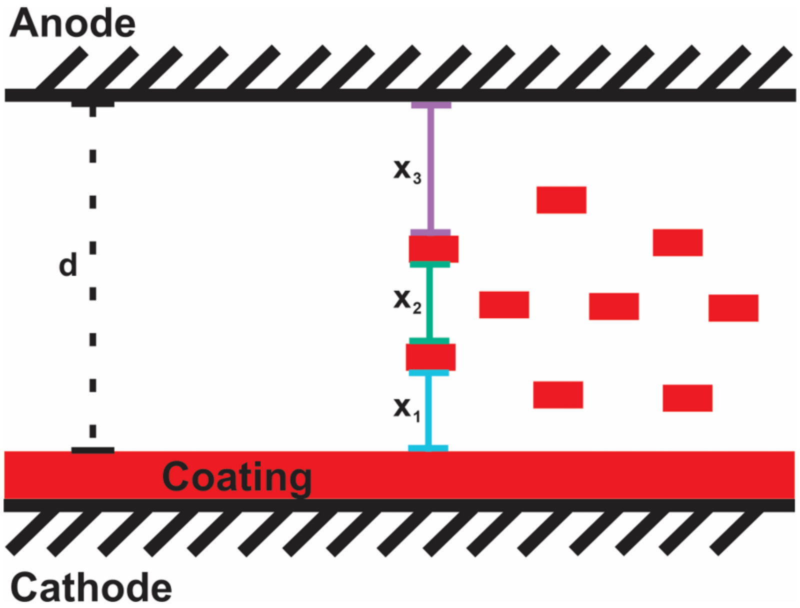

Figure 4.50: Material assisted breakdown diagram

All of this together suggests that within 10 ns (Figure 4.48 Aerodag 10 ns) of the current rise, many plasma channels form simultaneously (due of the uniform protrusion filled surface), causing a large amount of conductive material to fill the gap. The resistance of the plasma channels increases rapidly, with the resulting voltage drop increase across the gap creating many additional plasma channels that result in a nearly uniform gap at initiation. As the current rises, the number of channels that can form do, filling the small percent of the unfilled gap that remains. In addition it is important to note that the material on the cathode surface is ”fueling” the plasma jets (see Chapter 3) that form in the gap, so the more readily available ”fuel” there is, the more plasma will form within the current pulse duration. In the case of the Aerodag-G spray, there is a substantial amount of fuel as is apparent in the abundance of plasma emission observed in gated optical images.

Additionally, from our gated optical images as mentioned above, the gap is nearly filled 10 ns into the current pulse. From previous gated optical images we know that initiation occurs sometime between 0-20 ns. This would indicate that the initial breakdown voltage was enough to create multiple channels. If we reference Chapter 3.6, for sufficient particle size and energy, cathode and anode spots can be initiated by accelerated (by the electric field) microparticles onto the surface of the anode/cathode. We know that the voltage in the gap is typically peaked at (70 kV), so our average electric field is $\sim 10^8$ V/m with the field on the microprotrusions along the surface being 10-1000 times higher (see previous sections and Chapter 3), from Figure 4.49 we can estimate that our micro particles are of radius $\sim 0.25 \mu m$. We can then use Equation 3.17 to estimate the charge of our particle in the applied electric field, $\sim 10^{-15}$C, so our energy can be estimated as $\sim 10^{-10} J$, solving for velocity we can estimate our particles have a velocity of $\sim 0.07 km/s$. This puts us in the regime of particles that are not moving fast enough and with enough energy to ionize, partially ionize, and potentially deform the surface just initiating breakdown. If we then vary our particle radius size, we can see at what value that we enter the regime of particle impact initiation. Figure 4.51 shows a plot of tabulated impact velocity and energy for increasing particle radius. The blue line denotes the size of which particles accelerated into the electrode surface have enough energy and velocity to either ionize or deform the electrode surface to initiate breakdown. We find that particles over the size of 1.6 μm a particle on the surface will have enough energy and velocity. If we consider the flaky nature of the SEM images and the uniform distribution of microprotrusions of the aerodag coating, it is safe to assume that particles accelerated to the surface of the electrodes could be on the order of a few μm and that this is potentially a mechanism that causes rapid breakdown initiation and gap fill at 10 ns.

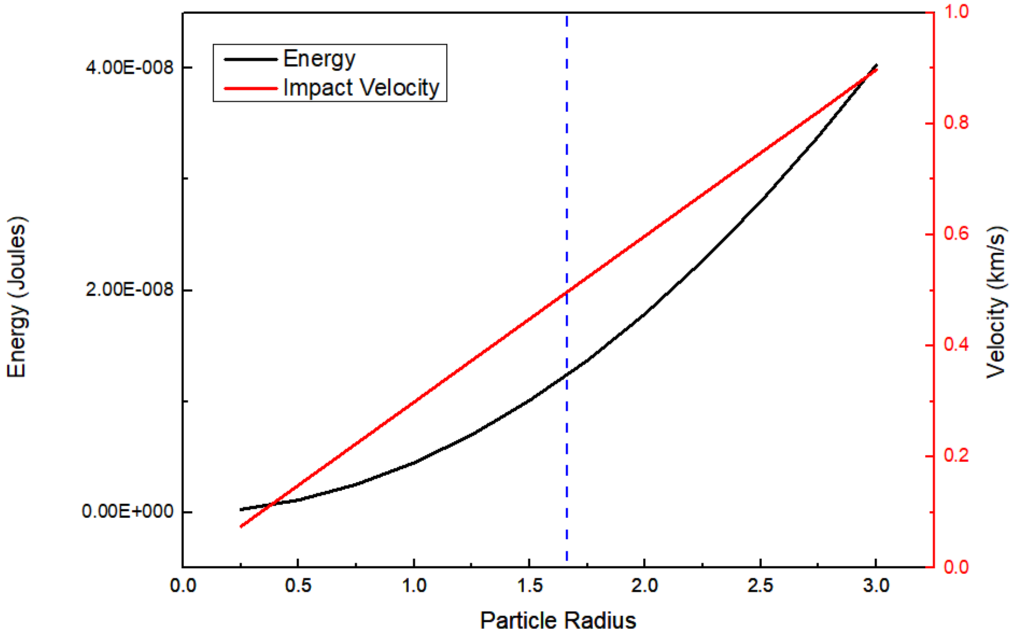

Figure 4.51: Particle impact velocity and energy versus particle radius, with the blue dotted line representing the particle radius threshold for impact initiation

4.4 External Axial Magnetic Field Experiments

In the previous section we have shown an Aerodag (graphite) coated liner achieving uniform plasma fill in the gap resulting in a uniform current density distribution at 1 MA. The immediate question is how else can we achieve a uniform fill? In this section we explore this question by applying an external axial magnetic field to the coaxial vacuum gap at 1MA to see the effects of a JxB force on plasma the forms in the gap.

4.4.1 Coated and Non-Coated (Aerodag) Liners at 1MA

An experimental series was devised to address points of interest regarding the initiation of plasma at the liner gap at the power feed cathode, and how the presence of an external magnetic field effects this. All targets were machined at Cornell using aluminium alloy (5056). Like the previous experiments, the target dimensions and design mimic the Z-targets (Figure 4.52), having an outer diameter of 8.16 mm, a thickness of 300 μm, and a height of 40 mm. The target connects at the cathode and is inset into a concentric anode where there is a large radial gap of 1300 μm. Figure 4.37 in the red outline, shows a simple diagram of the load region. The large cathode gap is held at 1300 μm by the use of an alignment cap inserted into the gap before tightening down the return structure that forms the gap. For this series we moved to a larger gap in hopes of having better resolution of movement in the gap.

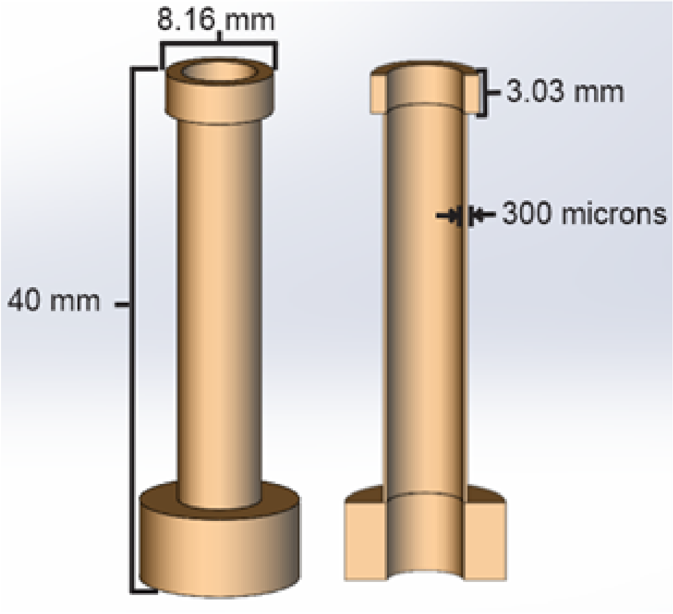

Figure 4.52: Cornell Liner dimensions

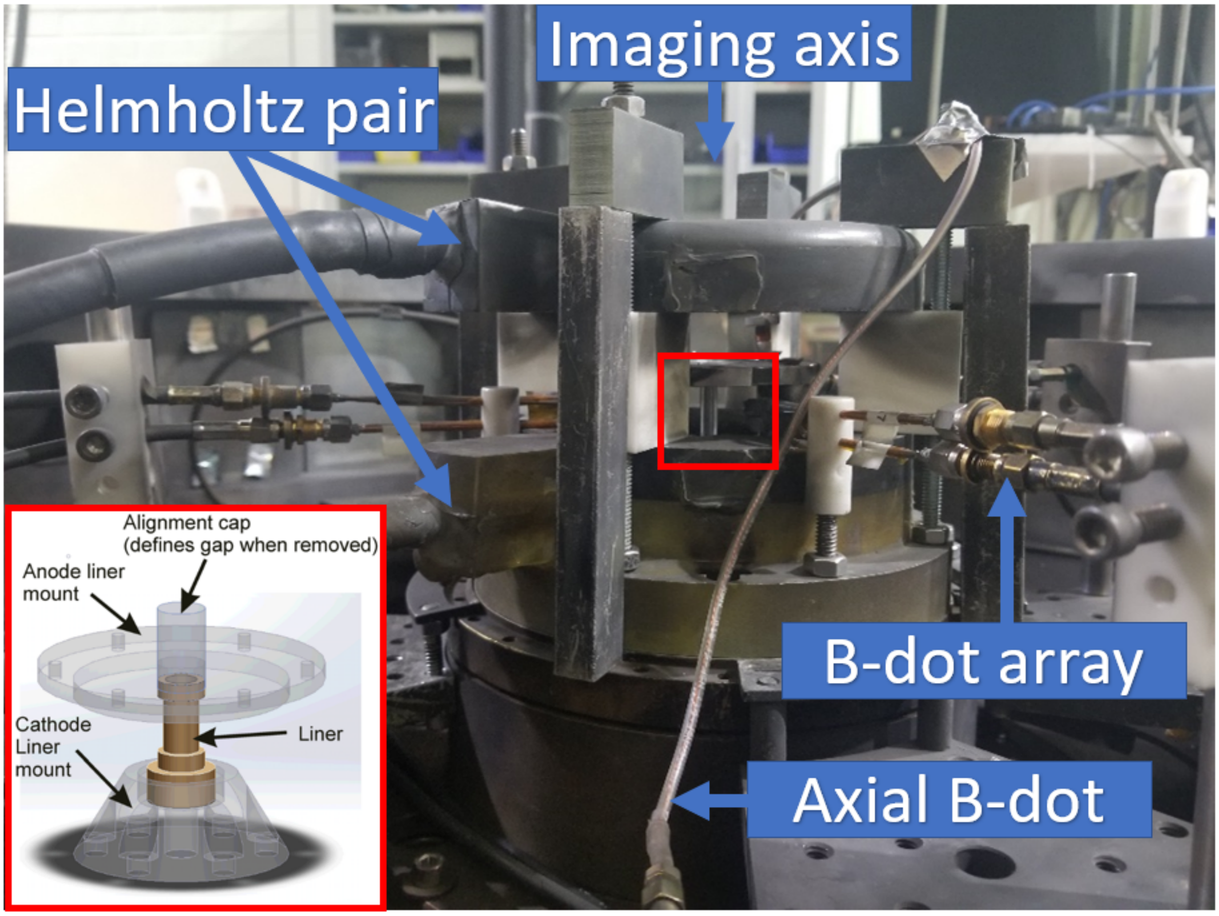

Figure 4.53: COBRA load diagram with and diagnostics labled

The diagnostic setup included (Figure 4.53) 12-frame end-on axial gated optical imaging (same as used in the previous section), a Helmholtz coil pair (up to 1.9 T) around the load, 8-probe B-dot array around the length of the liner (similar to above), and a single axial b-dot probe placed in the the anode plate (Figure 4.54 red square)

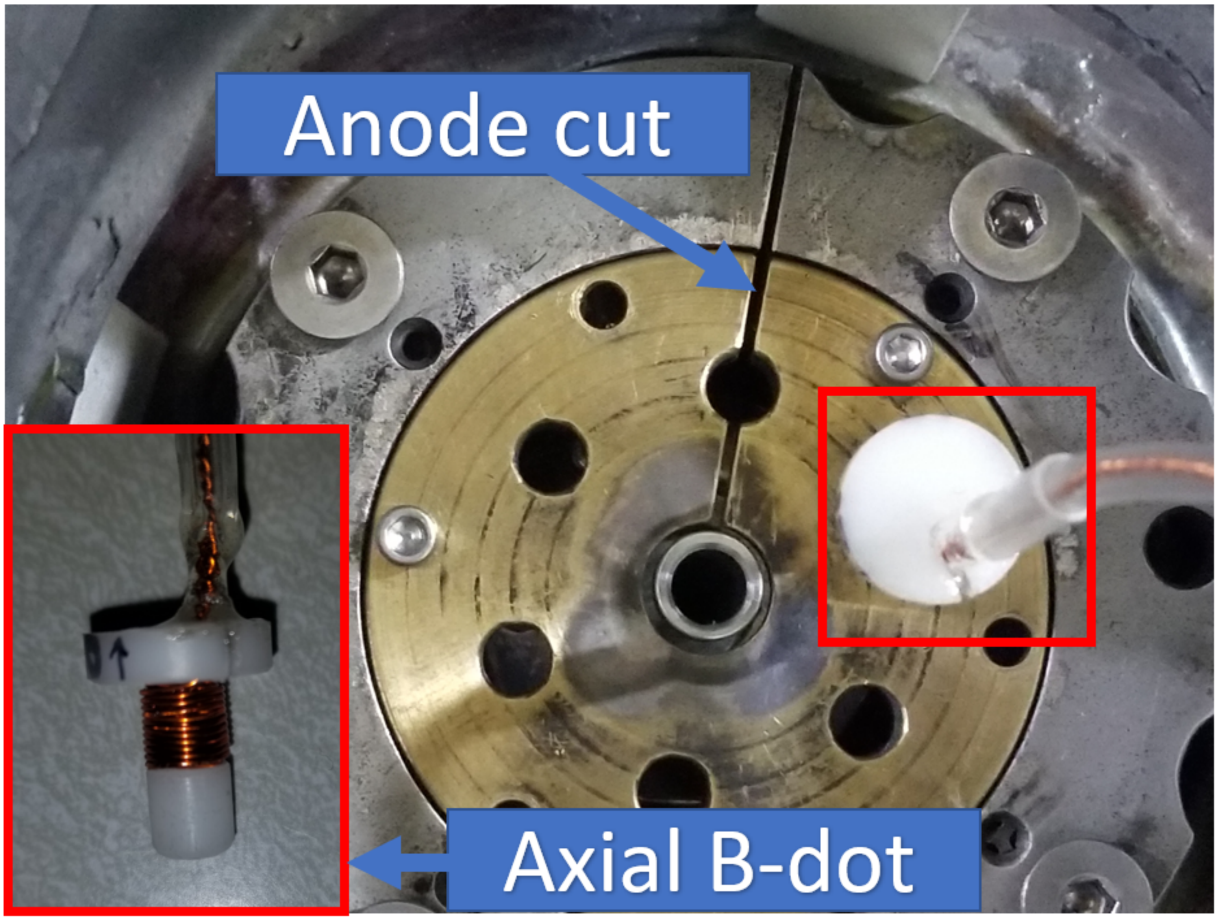

Figure 4.54: Top-down view of external magnetic field experiment anode plate with anode cut and axial magnetic field probe placement

The anode plate shown in Figure 4.54 has a$\sim$1 mm wide cut from the gap to the end of the anode plate. This was done to allow the external axial magnetic field to flux into the gap.

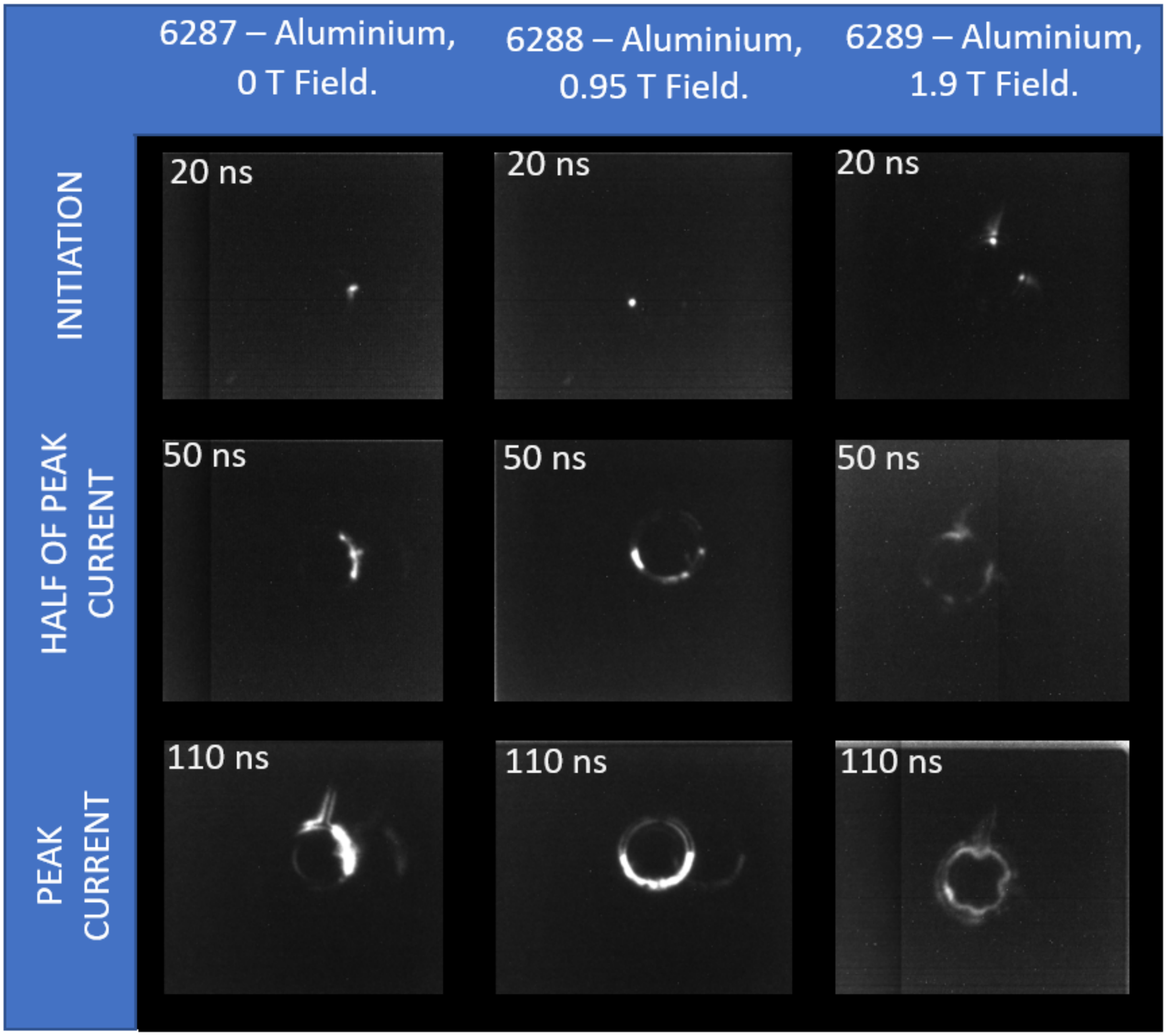

Figure 4.55: Image matrix of 12-frame gated optical images taken for three different shots, 6287, 6288, 6289 at 20 ns, 50 ns and 100 ns

We then investigated the extent that an axial magnetic field effects azimuthal plasma distribution in a coaxial gap by comparing 12- frame gated optical imaging for the three shots presented in Figure 4.55 at current rise breakpoints of initiation, half of peak, and peak. We see that for 6287, a 0 Tesla field shot the plasma initiation and behavior is in line with what has been seen in previous work at gap sizes of 50-1100 microns. Plasma forms in a single azimuthal location and grows as the current rises, but the gap does not fill. A change in the plasma fill behavior is observed when the external magnetic field is set to 0.95 Tesla, after initiation, we see the plasma is spread to about 50% of the gap by peak current, with most of the gap being illuminated. At 1.9 Tesla the increased expansion behavior continues, reaching a filled gap state at peak current. This is important because this is the first time a non-coated liner gap has filled in the history of the liner experiments on COBRA. The above figure shows that an external axial magnetic field does indeed influence the azimuthal plasma spread in a coaxial gap

To investigate and quantify the degree to which plasma formed in a coaxial gap spreads about the azimuth, with and without an external axial magnetic field, we developed two simple test cases to offset where plasma would initiate and at what relative size it would initiate so as to monitor and compare its growth optically via 12-frame gated imaging.

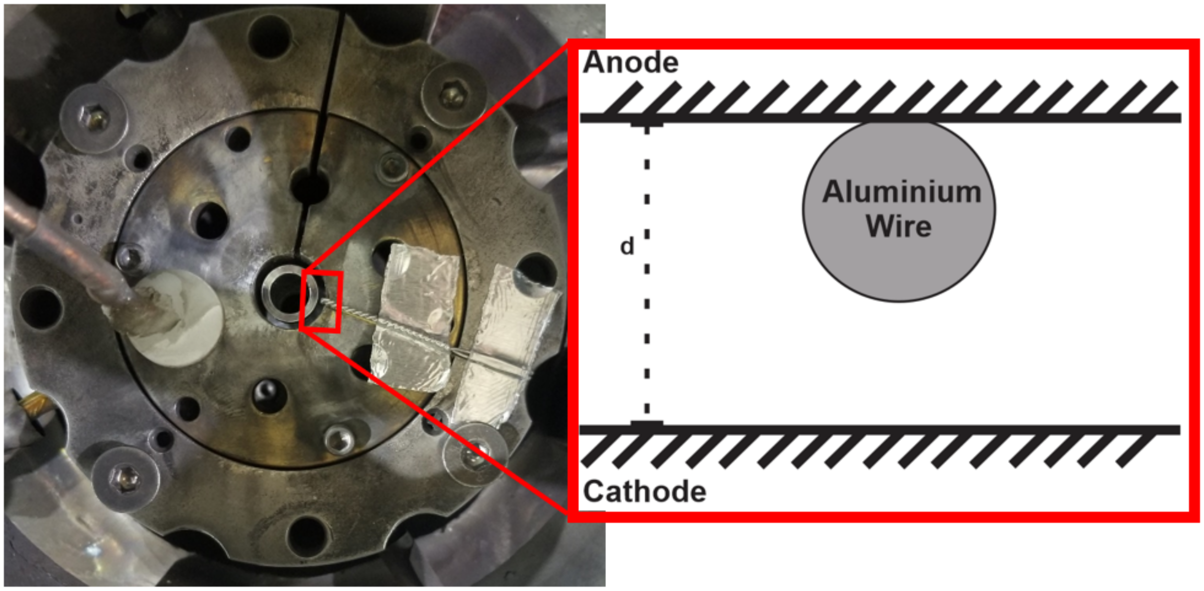

Figure 4.56: Aluminium wire placed in anode – cathode gap

The first case, Figure 4.56, a wire of known diameter (1200 μm) and azimuthal position is placed in the gap. The wire diameter closes the gap to 100 μm. Monitoring the gap via 12-frame gated optical imaging we can then measure the azimuthal spread of plasma in the gap every 10 ns for three different external magnetic field values, 0 Tesla, 0.95 Tesla and 1.9 Tesla

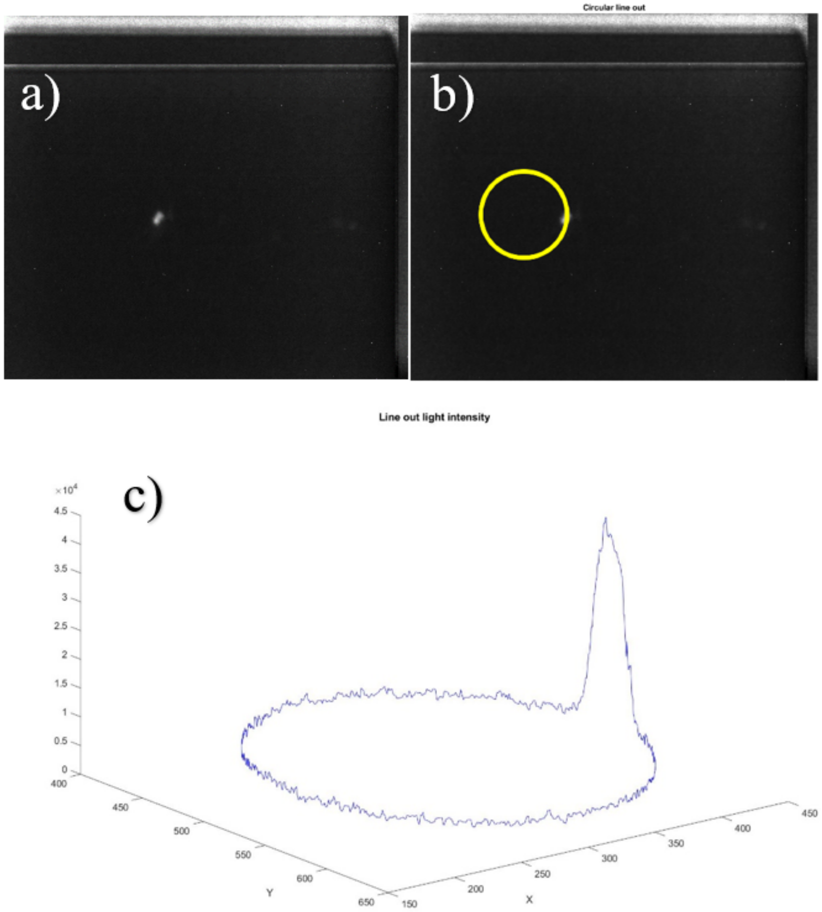

Figure 4.57: Single frame of End-on 12 frame gated imaging camera at 20 ns (a) with a circular lineout placed around the vacuum gap region (b) and the resultant intensity profile of the circular lineout (c).

To investigate the behavior of the plasma in the gap, we take a circular lineout of an individual frame and use the resultant intensity profile to quantify the width of the plasma in the gap at that time, this process is shown in Figure 4.57 for a frame at 20ns for shot 3601. Doing this for all frames in a shot we can plot and determine the direction of the JxB force exerted on the plasma.

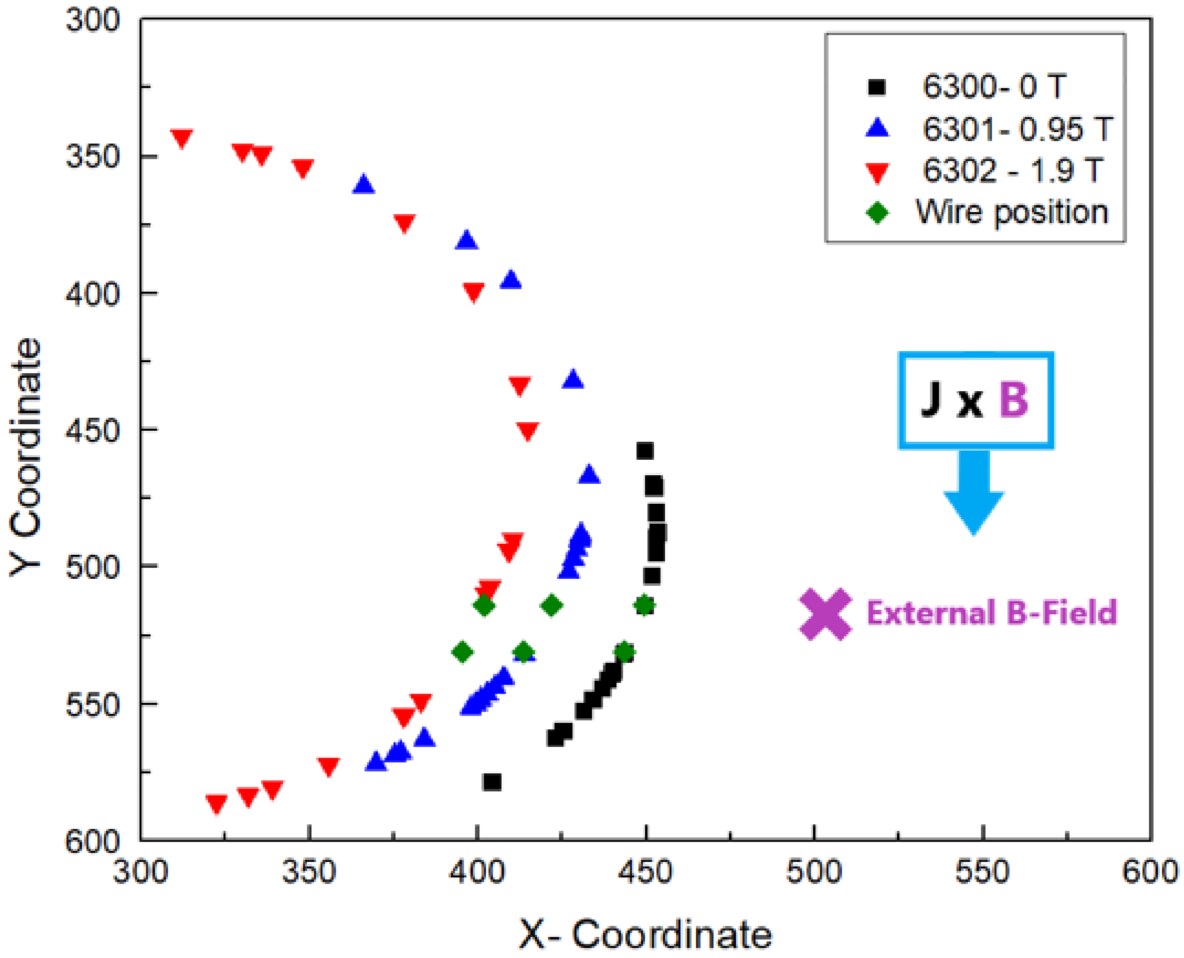

Figure 4.58: Circular lineout leading edge of azimuthal expansion width of plasma in the gap for three shots at three external magnetic fields. The wire position is marked in green, the magnetic field (purple) is into the page, with JxB in the clock wise direction. Note these data collected are from the same time in the current drive.

Figure 4.58 shows a plot of the circular lineout widths of 3 shots with and without magnetic field. The wire position is denoted in the graph by green dots, and the external magnetic field is into the page for shots 6301(0.95T), and 6302(1.9T). Extended widths are measured for both 6301(0.95T) and 6302(1.9T) as compared to 6300(0T). Note that the apparent direction of motion (CC) is at odds with electrodynamics (JxB (CW)), this anomalous behavior will be investigated and addressed at the end of this section.

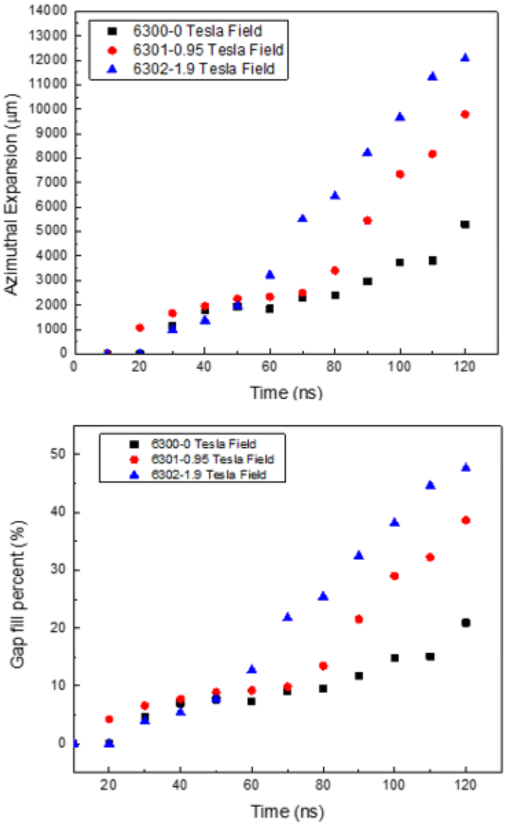

Figure 4.59: Azimuthal expansion vs. time (left) for three shots at three external magnetic fields, on the right the gap fill percent vs time for the same three shots. Significant change occurs after 60 ns.

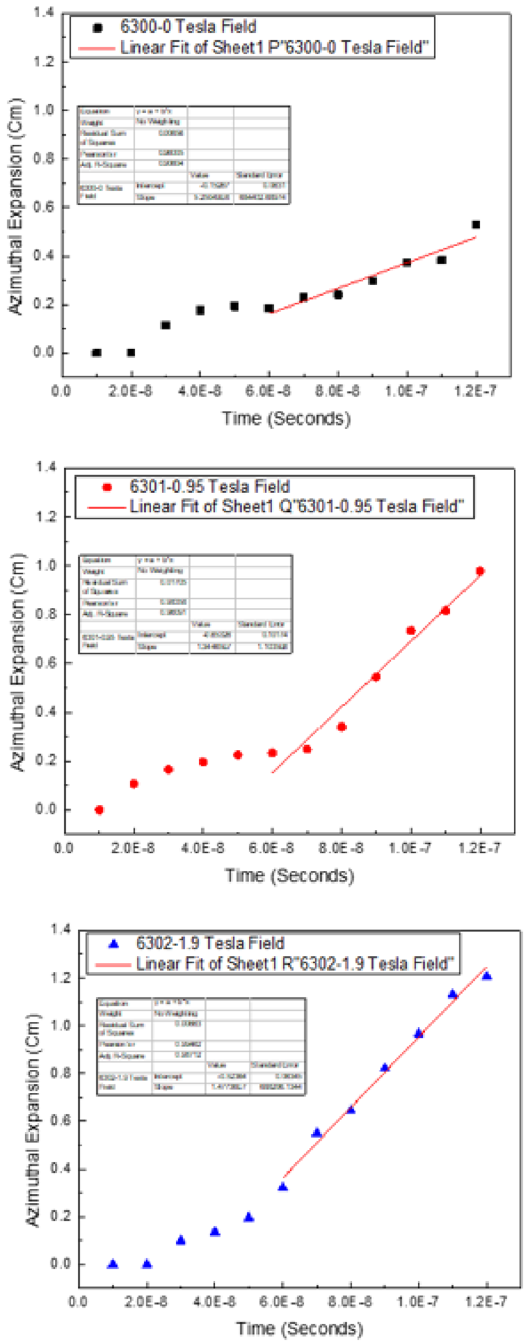

Figure 4.60: Linear fit from 60 ns to 120 ns for 6300, 6301, 6302 respectively

Using this method, we are able to then measure the expansion width as a function of time for the three shots in question. The results plotted in Figure 4.59, show that as the applied axial external magnetic field is increased the amount of azimuthal expansion increases. This increase amounts to$\sim$15% increase at 0.95 Tesla and$\sim$30% at 1.9T. The resultant velocity of each of these cases can then be estimated by finding the slope of a linear fit of the data (Figure4.60) from 60 ns to 120 ns. The measured velocity for 6300, 6301, 6302, are $5.4x10^6$ cm/s, $1.3x10^7$ cm/s, and $1.5x10^7$ cm/s respectively.

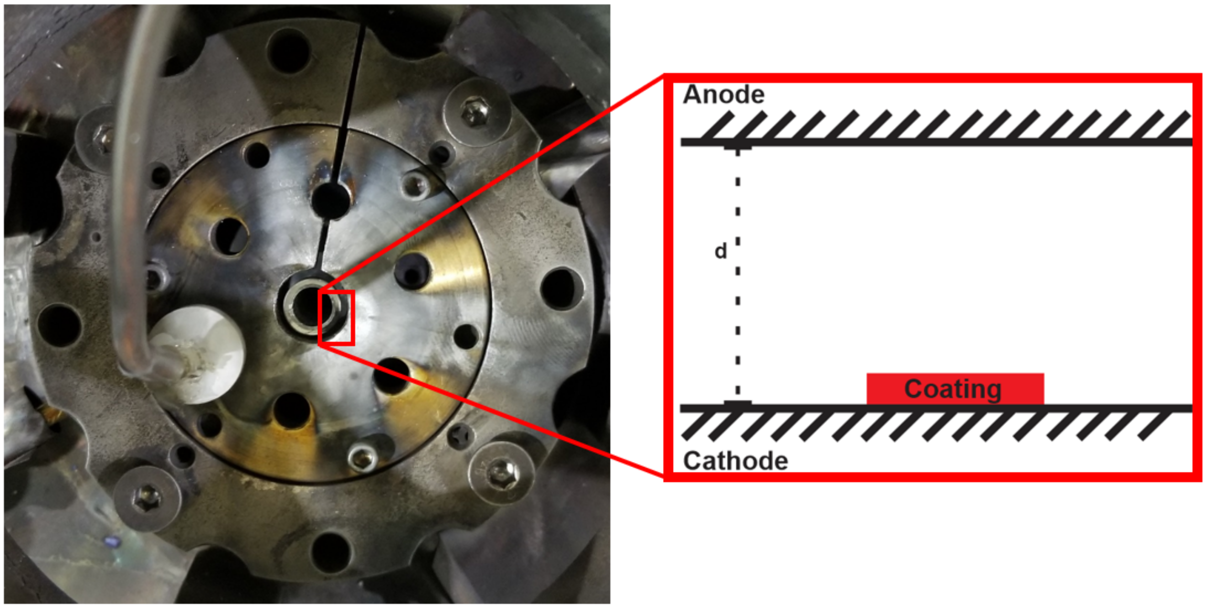

Figure 4.61: Aerodag offset coating liner in anode plate.

The second case, shown in Figure 4.61, has an Aerodag painted section of the surface of the liner, with a known width (4 mm), thickness (45 μm), and azimuthal position. Again, monitoring the gap via 12-frame gated optical imaging we can measure optically the azimuthal spread of the plasma every 10 nanoseconds for a 0 Tesla shot and a 1.9 Tesla shot using the method described above. Figure 4.62 shows that with an external magnetic field of 1.9 Tesla the azimuthal spread increases to nearly fill the entire gap. This increase amounts to a difference of $\sim$30% at 1.9 T. The resultant velocity of each of these cases can again be found via the slope of a linear fit of the data (Figure 4.63) from 60 ns to 120 ns. The measured velocity for 6296, and 6297 are 1.8E7 cm/s, and 2.8E7 cm/s respectively.

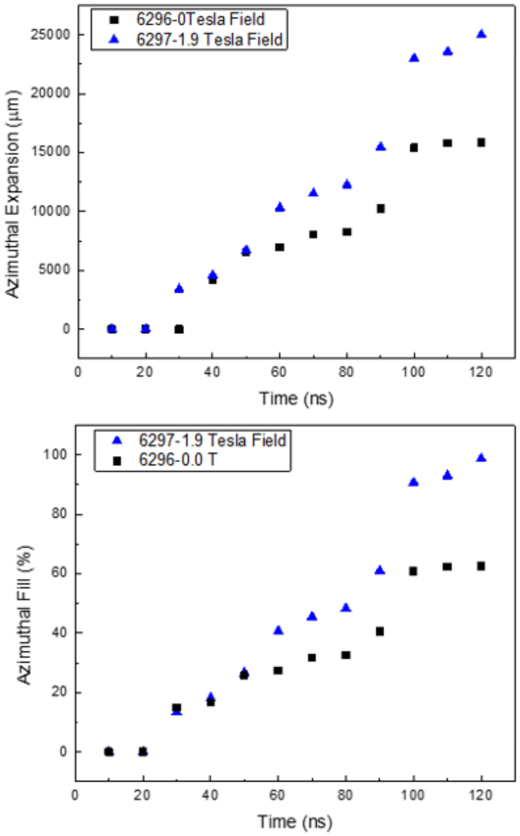

Figure 4.62: Azimuthal expansion vs. time (top), azimuthal fill percent (bottom), for liners with a graphite coating.

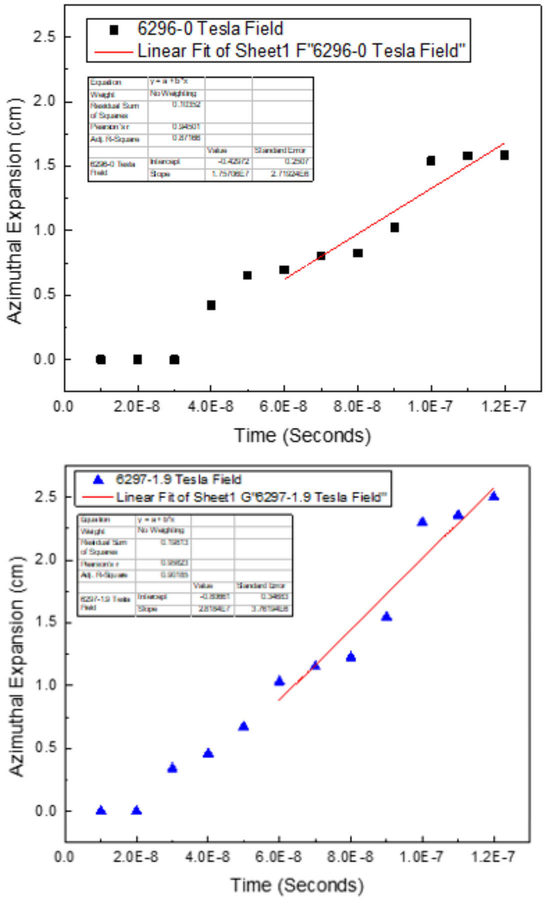

Figure 4.63: Linear fit from 60 ns to 120 ns for 6296(top), and 6297 (bottom)

We can compare our measured expansion velocity to measurements and calculations from the literature [3]. For an aluminium liner at 0 Tesla the average velocities are on the order 10^6cm/s, this is in good agreement with the 0T 5.4E6 cm/s velocity for the wire in the gap case. According to the literature [41] [45], in the presence of a magnetic field the velocity increases two fold. In Chapter 3, many of the cited experimental works suggest that velocity of cathode spots increases linearly with magnetic field, if we plot our expansion velocity for each case (Figure 4.64).

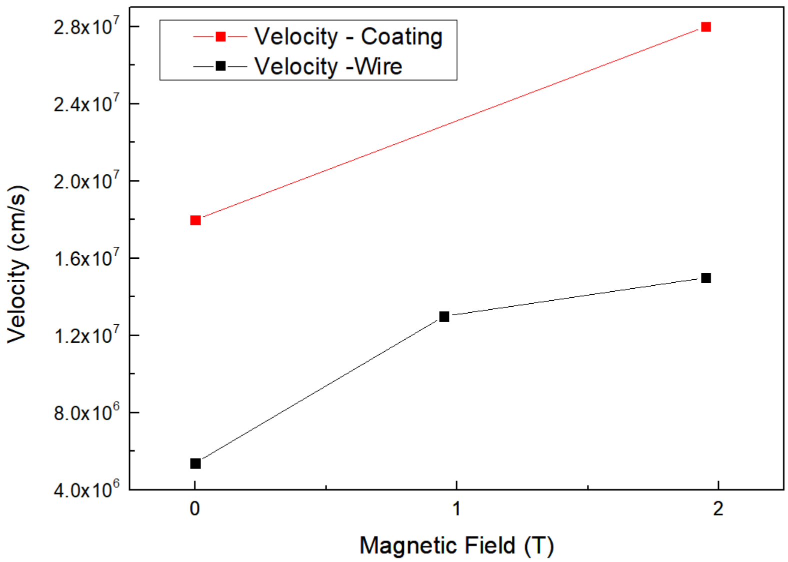

Figure 4.64: Velocity measurements for wire in the gap (black) and the off-set aerodag coating (red) with increasing magnetic field

For the wire case, we have a∼2x increase in velocity from 0T-0.95T, and an increase in velocity of 0.2E7 cm/s from 0.95T to 1.9T. For the coated electrode, we have a∼1.5x increase in velocity from 0T-1.9T. Both of these cases are in good agreement with the literature, see Chapter 3 for detailed velocity calculations and estimates. Differences in the velocity between the wire case and the coated cathode is∼2x, and is likely due to the surface profile of Aerodag and the area of the coating compared to aluminium.

Using the experimental data, we can estimate how long the plasma will take to fill the gap for a fixed current density and an increasing axial magnetic field. From our circular lineout intensity plots of 12 frame gated optical imaging, we have measured width (1074 μm) of the off-set plasma at initiation (20ns) at 0.95 Tesla, and a current of 48 kA. In addition we can assume the mass of the initiated plasma as the mass of the aluminium in a skin depth $\sim 6.5x10^{-5}kg$. Using these values we find that the time to fill is ~296 ns, which is about twice the duration of the current pulse, and in line with the measured ~ 40 % fill at 150 ns. We do the same thing for the off-set graphite coating finding that at 1.9 Tesla, the gap should fill in 123 ns (Figure 4.59). The results plotted in Figure 4.65 show that with the above conditions, even with an external magnetic field of 30 Tesla, the gap takes 36 ns to fill with an off-set aluminium wire and as fast as 16 ns with an Aerodag off-set coating.

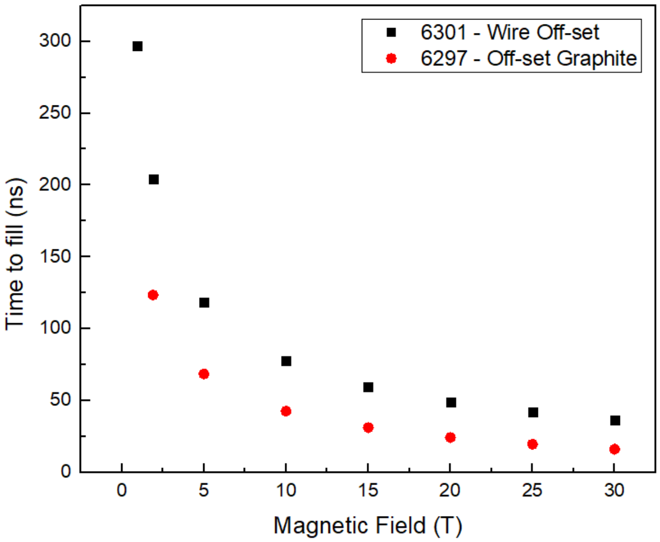

Figure 4.65: Time to fill for a constant current density J and increasing external axial magnetic field for an aluminium wire off-set(black) and an off-set graphite coating (red).

For the MagLIF load on the Z-machine (Chapter 1), the above results suggest that at a significantly higher current density (26MA) and with a 30 Tesla external axial magnetic field, even if the gap is offset, the resultant JxB from the external field should be more than enough to force the gap to be filled. If we use experimental and estimated values we can suggest on what time scale this could happen on the Sandia Z-machine. At 20 ns we have~2 MA of current, for simplicity we will use the same mass as above. Therefore, with a 30 Tesla external field and the above estimates the gap will fill in$\sim$8 ns. From our previous project review on coated liners, we showed that a filled gap means uniform current density distribution. Therefore, it is likely that the current density into the surface of the liner on a MagLIF shot on the Z-machine is likely to be uniform within 10 nanoseconds of initiation. This means that the current in the liner is likely uniform$\sim$40 ns before the liner begins to implode ($\sim$50 ns) [80].

In previous sections we have shown that breakdown spots are non-stationary and form randomly in the vacuum gap on a nanosecond timescale, with new breakdowns more likely to appear near existing breakdowns, but still overall stochastic. In the presence of an external axial field we have shown above that the breakdown behavior changes significantly, rapidly spreading and filling the gap as the magnetic field increases. But in what direction do the breakdowns move? To investigate this recall Figure 4.58, which shows the circular lineout edge of azimuthal expansion width of plasma formed in the gap for three shots at three different external magnetic fields. The wire position is marked in green to show the starting width and to act as a reference for expansion, the magnetic field is marked as into the page, with the direction of JxB (clockwise). However this is not what was the measured direction of breakdown formation. In fact, what we see is motion/expansion in both vector directions with the dominant motion/expansion in the opposite direction, -JxB, known in the literature as ”retrograde motion.” I will note here that this behavior is not fully understood and many different models exist attempting to explain it [41],[32], [45], [38], [3],[6],[62].

To get a better idea of what is happening, we consider the behavior at the surface of the gap. Figure 4.66 is a simple diagram of a vacuum gap with an external axial magnetic field. For simplicity, only a single plasma channel is considered to have formed at this instance, when in reality there are many. The current density J and magnetic field directions are labeled. The general idea is that when an axial external magnetic field is applied to the gap , the occurrence of new breakdowns (black dotted circles) becomes directional following -JxB vector (red arrow), in addition to the random nature of breakdown formation as seen in previous sections of this document. Whereas the plasma channel itself moves in the vector direction of JxB (green arrow), this can be explained by the generation of a self field of the breakdown spot and the external field, as these produce a large magnetic pressure on one side of the breakdown spot that forms on the cathode. This in turn increases the probabilities of the next spot igniting on the retrograde side.

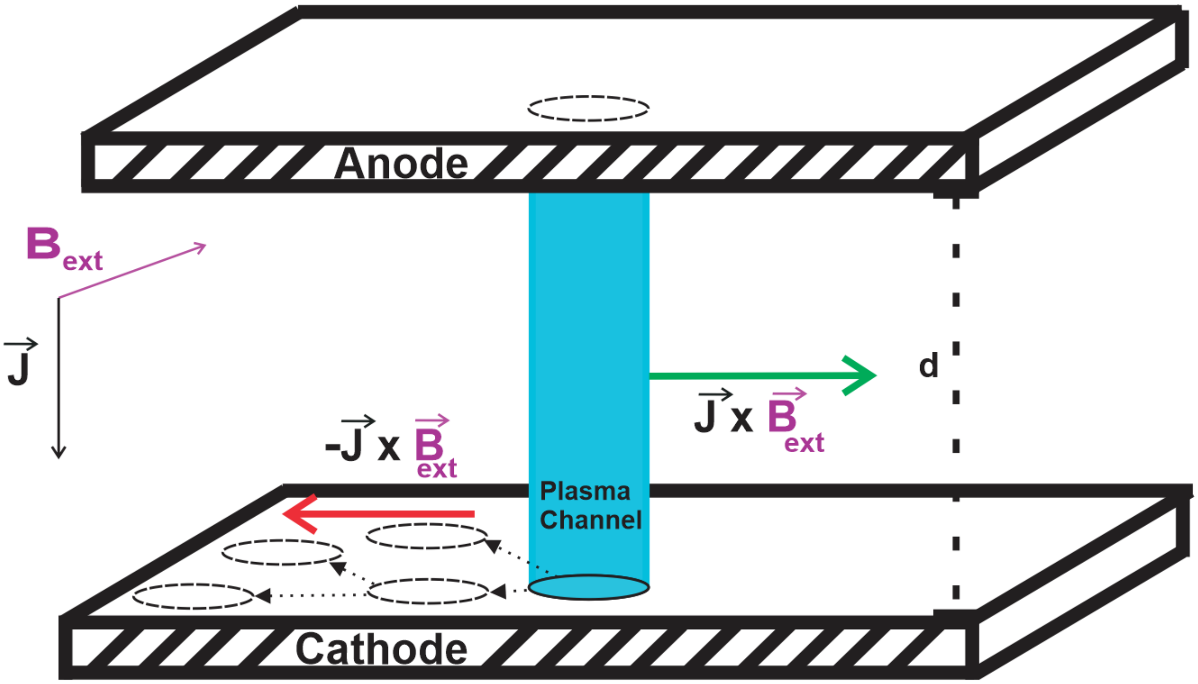

Figure 4.66: Schematic diagram of breakdown with an axial magnetic field

We can see this behavior experimentally in gated optical images for shot 6288, which is an aluminium liner that is non-coated, non-offset with a 1300 μm gap and a 0.95 T axial magnetic field. Figure 4.67 shows two gated optical images, at 20 ns with plasma emission in the lower left hand corner and is highlighted by a red circle, 10 ns later in frame 30 ns the same initiation spot is highlighted with an addition of four additional emission spots that have formed in the -JxB vector direction.

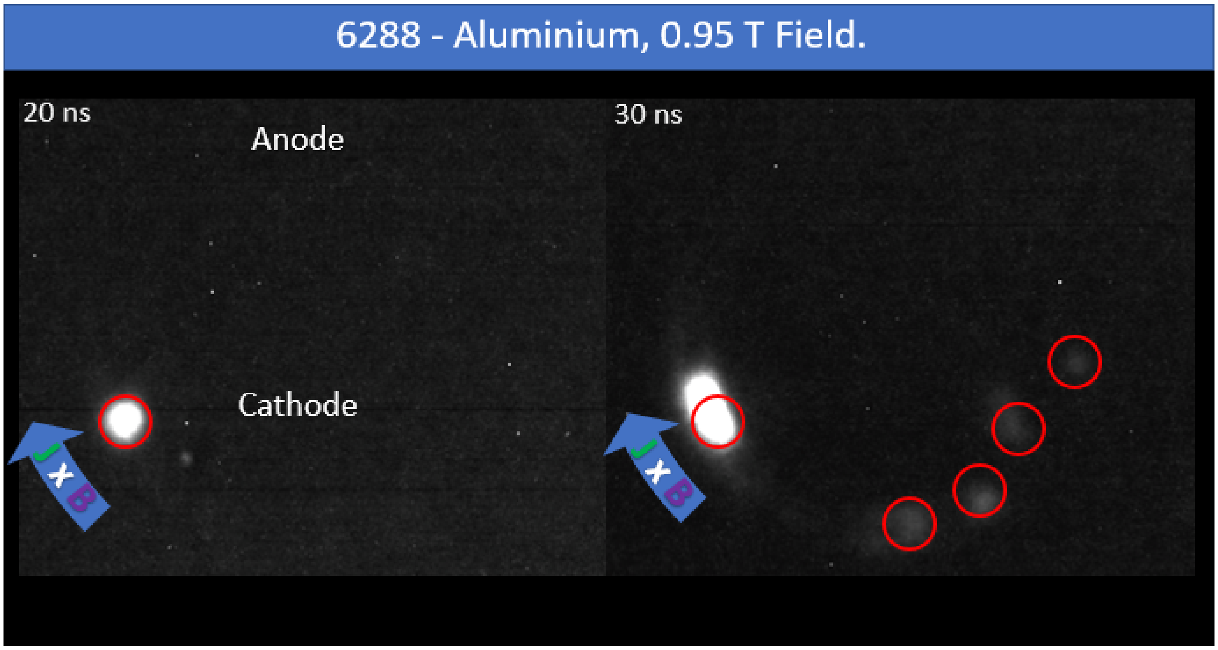

Figure 4.67: Gated optical images at 20 ns (initiation) and 30 ns for experimental Shot 6288, Aluminium liner 1300 μm gap(no coating) with a 0.95 Tesla axial magnetic field (into page) and the resultant JxB force is in the clockwise direction.

This behavior persists through the duration of the current pulse. Figure 4.68 shows 10 gated optical images for shot 6288 with plasma emissive initiation sites circled in red. Again, we see the spots form in the direction of the -JxB direction. If we focus on the first frame (20 ns) initiated emissive spot in the bottom left and watch its growth, we can see that as the current rises, and the frames increase in time step, the plasma that has formed expands radially in the JxB direction, using the same circular lineout program as before we can estimate the velocity of the expansion of this emission site as $\sim 1.6x10^7$cm/s

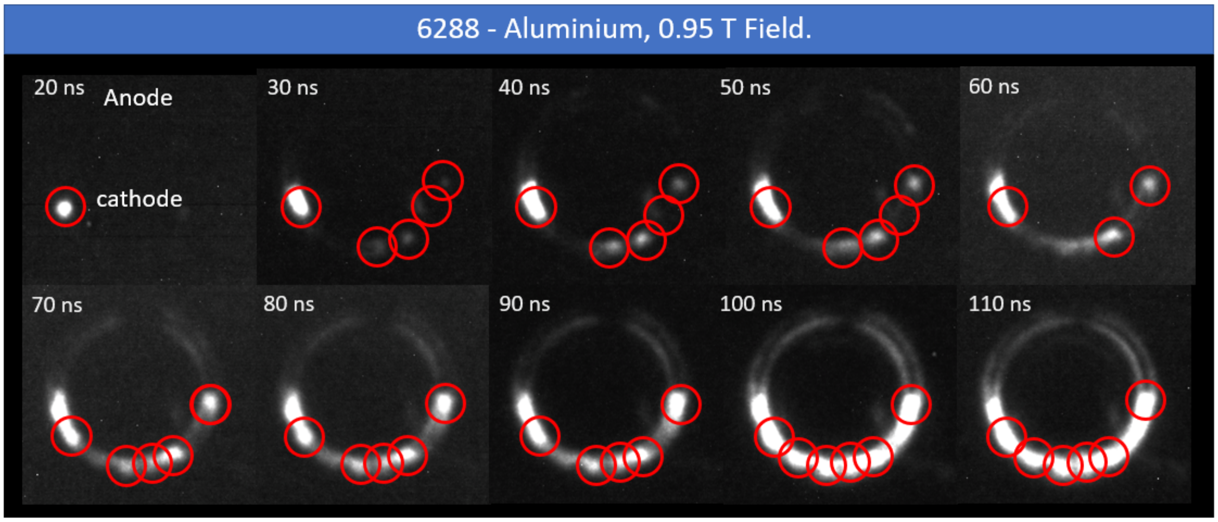

Figure 4.68: 10 Gated optical images at 10 ns steps along the current rise for experimental Shot 6288, Aluminium liner 1300 μm gap(no coating) with a 0.95 Tesla axial magnetic field (into page)

We can then compare this behavior to the shot 6287 for an aluminium non-off-set liner with a 0 Tesla field. Figure 4.69 shows two gated optical image frames at 20ns with plasma emission in the upper right hand side (red circle), and a frame at 30 ns. As the current rises new spots form on either side of the initial breakdown, this formation of additional random channels is thought to be due to resistive restrike [14]. We can again plot the full sequence of gated optical images (Figure 4.70) and see that like the previous data presented in this document the an initial spot forms grows, new spots are generated that in turn grow through the current rise with late time spots forming. With these frames we can use the circular lineout program to estimate the expansion speed of the emission sites observed in the gated optical image frames. We find that the velocity of expansion is $5.7x10^6$cm/s. Note this retrograde motion is observed in all shots performed in the experimental campaign that had an external magnetic field.

If we consider the expansion of our velocity to be adiabatic, and just based on thermal expansion into the vacuum we can say the velocity at 0T is equivalent to the sound speed. Comparing to the 0.95T velocity we see that $v_{0.95T} > v_{0T}$ which is necessarily caused by the JxB force acting on the plasma column as in our picture. If we then compare the behavior of the breakdowns, in the 0T case (Figure 4.70 to those in the 0.95 T case (Figure 4.68) we see that in the presence of a magnetic field the emission spots follow the anti-amperian motion as described above, while when no field is present the motion returns to the random behavior seen in Figure 4.70, and the rest of the unmagnetized shots presented in this document.

Thus, the main driving factors for increasing the fill of plasma around a magnetized gap are; 1) JxB on the plasma jet spreads the plasma out in the gap, giving more area for current to be carried countering its ability to increase the number of breakdowns based on ionacoustic instability [14] and 2) new breakdown formations in the opposite direction of JxB are driven by the anti-amperian motion caused by the presence of the external magnetic field [5].

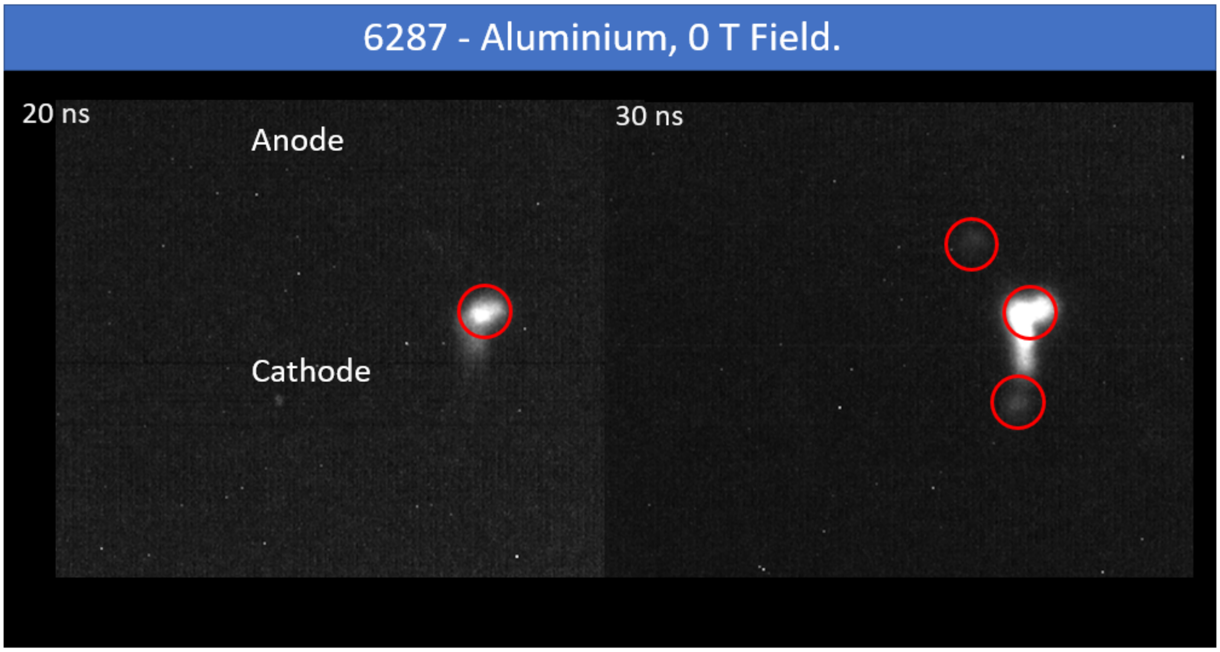

Figure 4.69: Gated optical images at 20 ns (initiation) and 30 ns for experimental Shot 6287, Aluminium liner 1300 μm gap(no coating) with a 0 Tesla axial magnetic field.

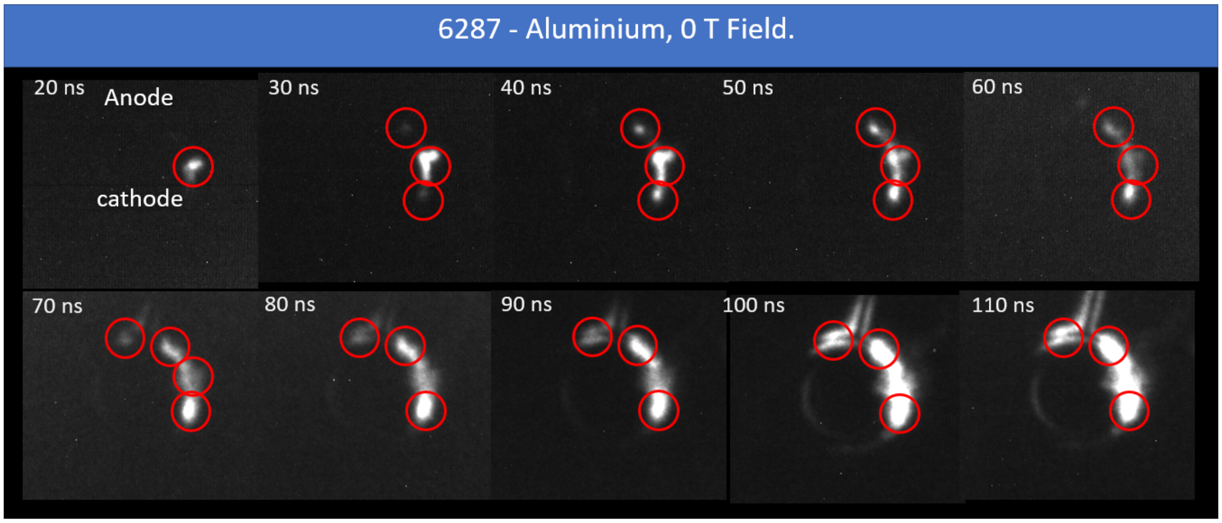

Figure 4.70: 10 Gated optical images at 10 ns steps along the current rise for experimental Shot 6288, Aluminium liner 1300 μm gap(no coating) with a 0 Tesla axial magnetic field

4.5 Fielding Probes at 26 MA

Throughout this chapter, I have shown how coaxial gap breakdown behaviors scale on experiments from 240 amperes to one megaampere. Thanks to the LDRD program at Sandia National Laboratories and Dr.Yager-Elorriaga and Dr.Gabriel Shipley, I was able to field magnetic field probe arrays on two separate experimental campaigns on the Sandia Z-machine.

4.5.1 Probe Design For 26 MA

The inside of the chamber of the Sandia Z-machine is an incredibly harsh environment. The hardware inside the chamber is completely obliterated after peak current. In addition, the proposed location of the probes for these shot series is very close to the load region (15 to 26 mm from the center of the load) and the amount of space available for the probes is very limited. With the above criteria in mind, we designed a mounting scheme and B-dot size. Figure 4.71 shows the aluminium B-dot mount, that holds two 18 mm micro B-dots (Figure 4.71 - red)whose loops are $\sim$2 mm apart, with the probes being opposite loop pairs (one up, one down). The hollow mount is filled with epoxy after the B-dots are mounted to secure the B-dot position so they do not move when Sandia Engineers place them in load specific positions within the chamber, this also gives some added protection for the probes themselves.

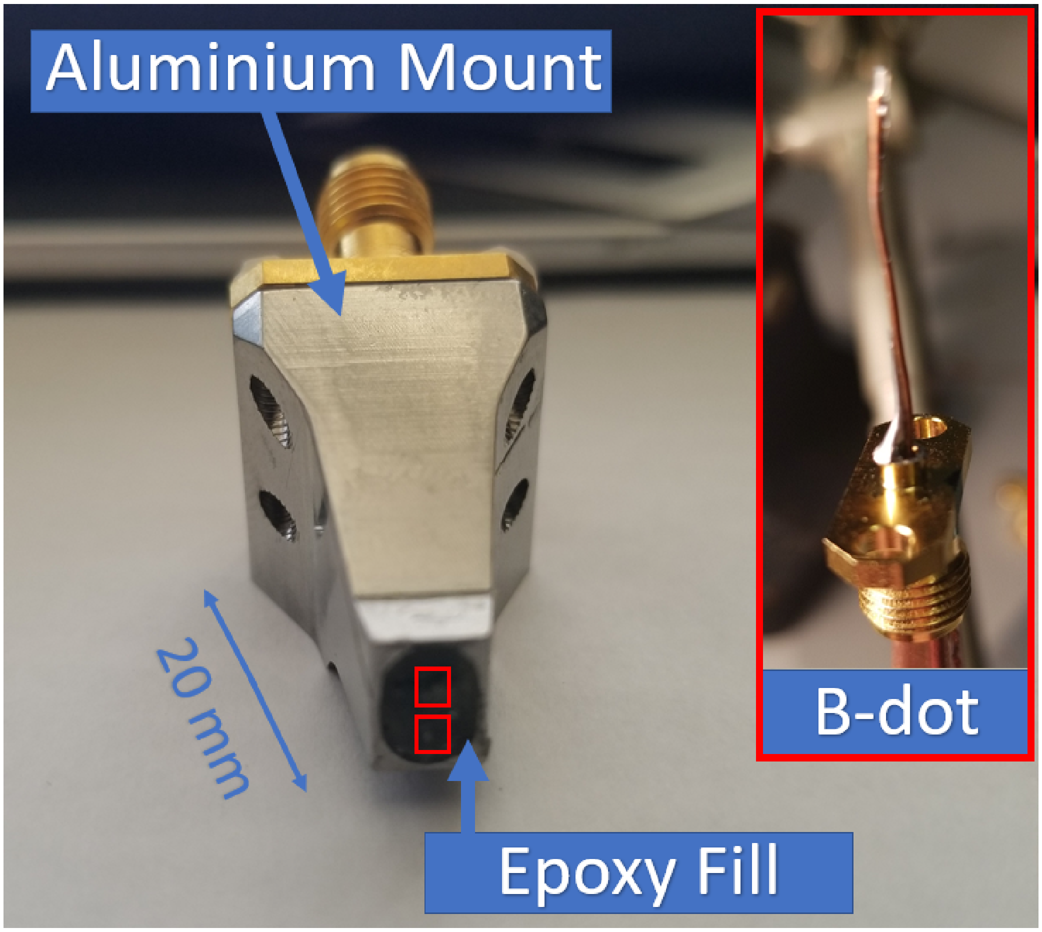

Figure 4.71: Magnetic field probe mount design labled, with micro B-dot outlined in red

4.5.2 Eddy and Dynamic Screw Pinch

We were able to field the above probes on two separate shot campaigns on the Sandia Z-Machine. The first was termed Eddy, and was looking at the stagnation phase of a magnetically driven liner implosion [44]. The second campaign termed Dynamic Screw Pinch, and was investigating a novel technique to mitigate the Magneto Rayleigh Taylor instability in the liner [69]. Of particular interest was if we could unfold information about current density distribution through and around each campaign's return structure through the use of fringe magnetic field probes.

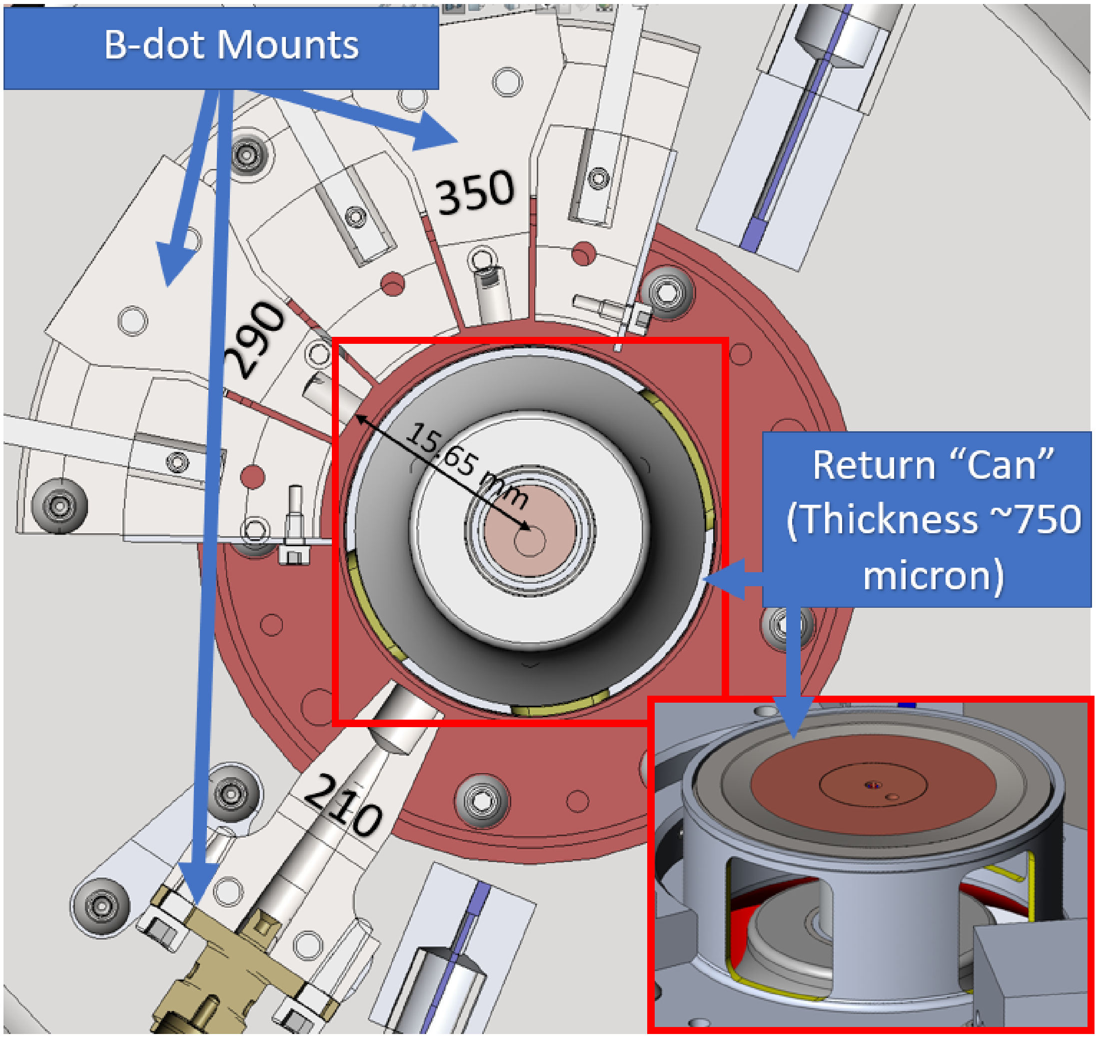

Figure 4.72: Eddy shot series load design with probe locations.

Figure 4.72 shows the Eddy shot campaign load with slotted return can structure (red square) and the location of the B-dot mounts with respect to the load. B-dots are located at three azimuthal locations, 210 °, 290°, and 350°, all of which have solid return structure in front of them that is generally 750 μm thick but can vary in thickness slightly.

In Eddy shot Z3423 all of the magnetic field probes fielded measured signals through the current pulse (Figure 4.73a) and were of the similar magnitudes to in house initial low/res Maxwell simulations for the geometry (Figure 4.73b), with probe locations denoted by the orange dots. When comparing to the current trace (BIB5000) we see the magnetic field probes all have a similar shape to one another, with a decrease in magnetic field just after peak, which is similar to the double hump behavior in the current signal that denotes stagnation, henceforth known as a stagnation bump. In addition, all the probes have a time delay that ranges from 1 ns - 741 ns (Table 4.5). Note, the naming schema of the probes are as follows; degree location, (t) top or (b) bottom position in mount.

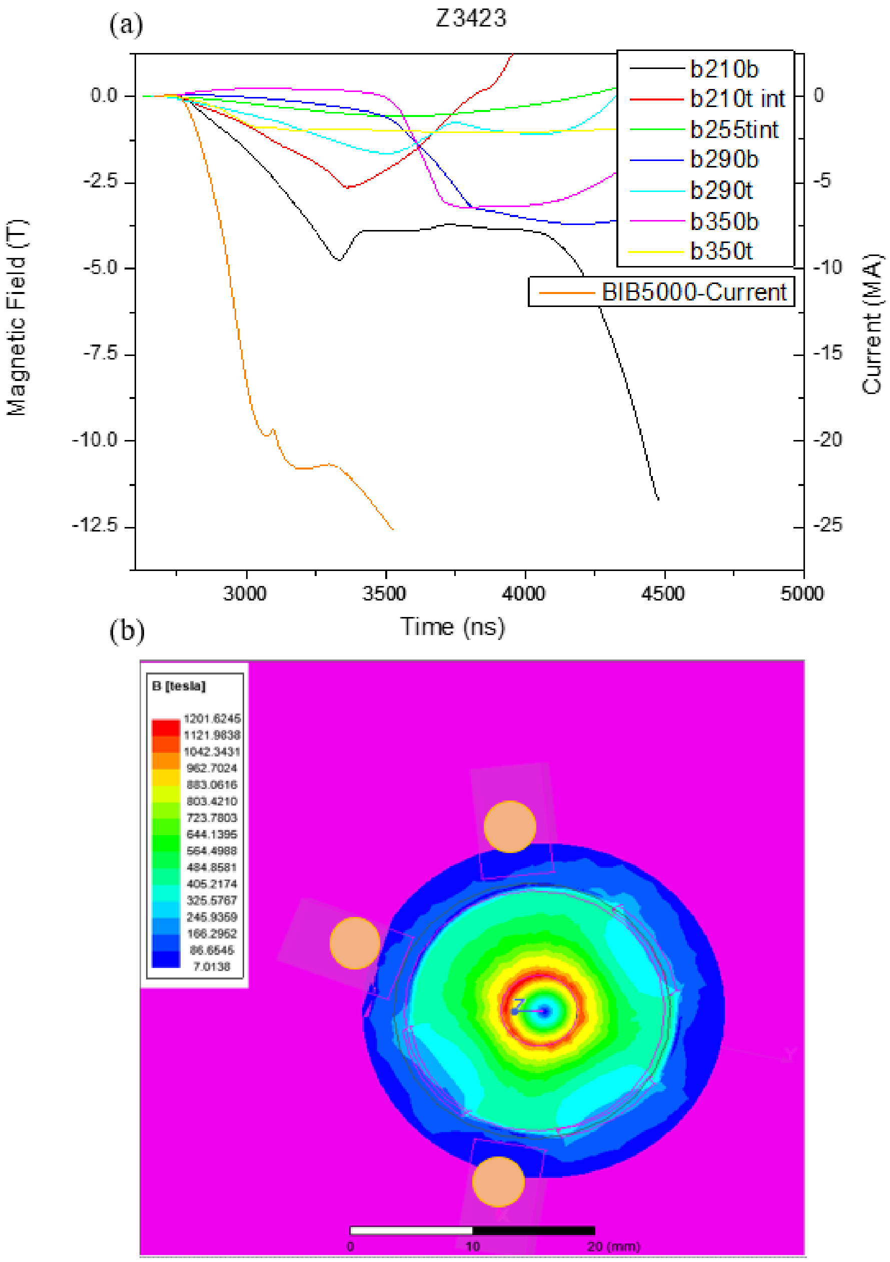

Figure 4.73: Z3423 Current and magnetic field traces (a) and Maxwell simulation of magnetic field magnitudes of the load.

Table 4.5: Magnetic field diffusion time measured for each probe in Eddy shot z3423

Probe	ΔB_t B-field diffusion time measured (ns)
b210b	259
b210t	288
b290b	741
b290t	431
b350b	736
b350t	1
BIB5000	0

If we then compare the fringe probes to the INNER MITL B-dot probes signals (Figure 4.74) we see the probes follow the general shape of the current pulse very closely, deviating in magnitude from one another as current rises. The delay seen in the fringe B-dot probes is not seen in the Inner- MITL B-dot probes. The reason for this is likely that the IMITL probes are ~60 mm away from the load (~30 mm away from fringe probes) and are measuring the Inner-MITL current, whereas the fringe probes are sat right in front of the return structure. We have shown in the previous sections of this chapter that 5 - 10 mm in length is plenty of distance for asymmetries to form and grow in ampere or megaampere experiments. This would account for the slight differences in magnitude measured in the inner-MITL as well as those seen in

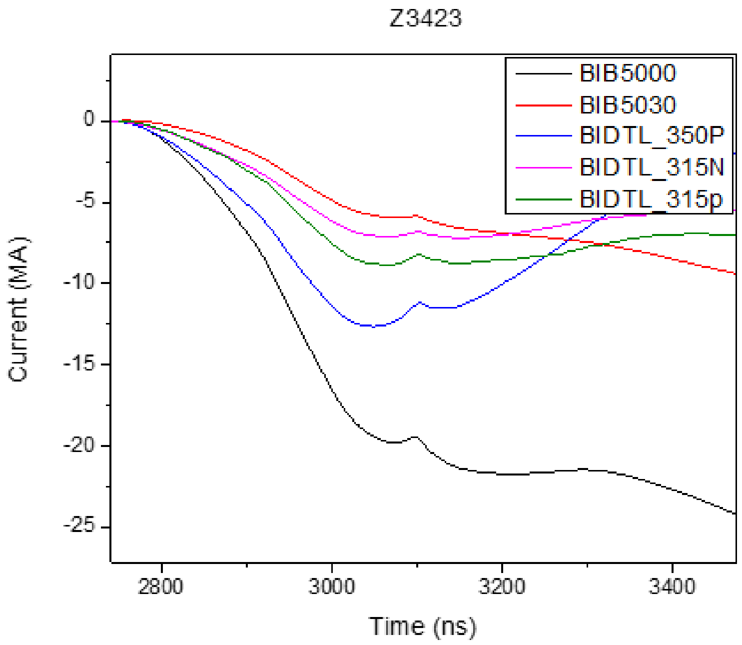

Figure 4.74: Z3423 Current traces from magnetic field probes in the Inner-MITL region.

In Eddy shot Z3491 only two of the probes survived, B290 and B350. The reason for the failure of the other probes is unknown. Figure 4.75 shows measured probe magnitude (a) that are similar to what is predicted by low resolution Maxwell simulations (b) for the load. The shape of the signals also have a stagnation bump and follow the same general form as the current (BIB5000) although again a time delay in the probes is present in this shot, with values of 712 ns and 814 ns (Table 4.6).

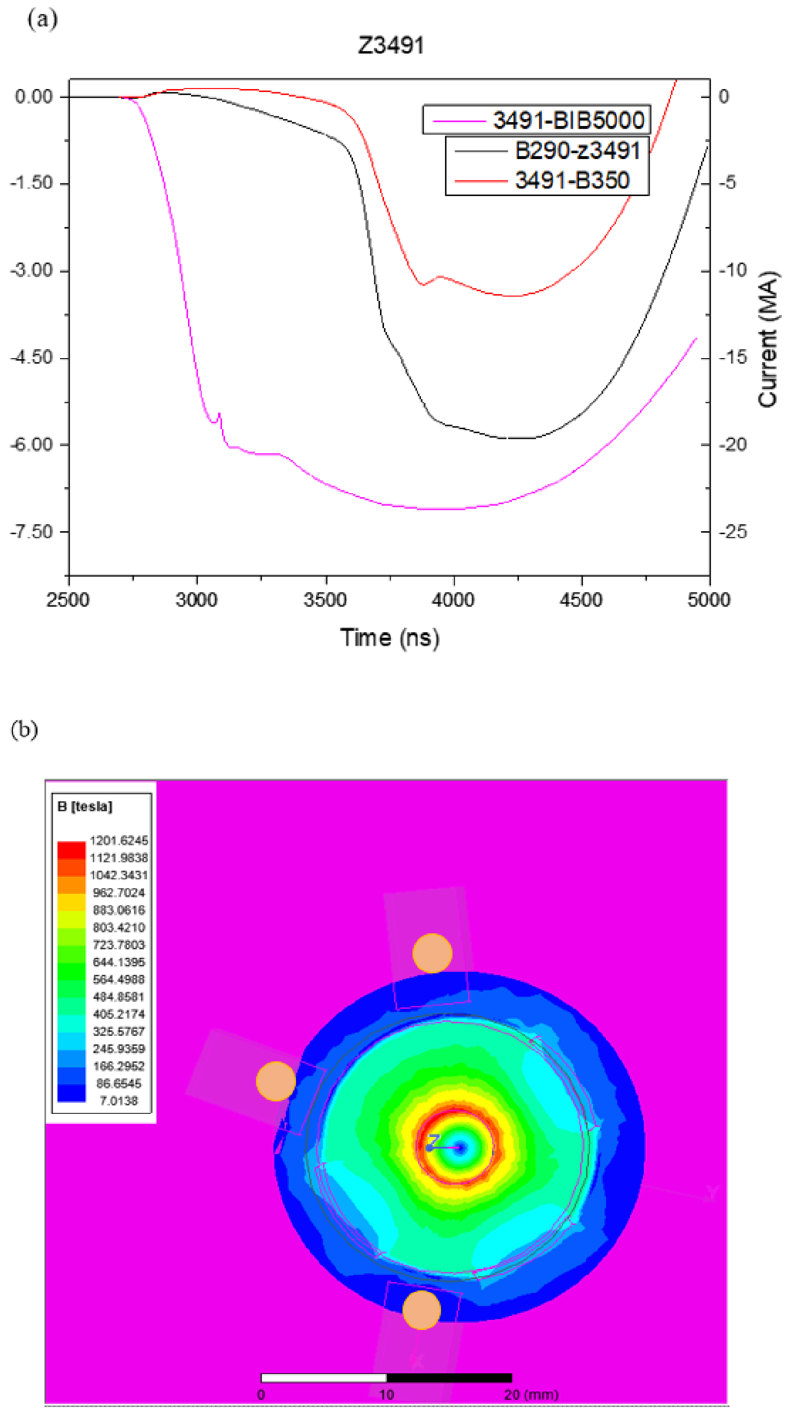

Figure 4.75: Z3423 Current and magnetic field traces (a) and Maxwell simulation of magnetic field magnitudes of the load.

Table 4.6: Magnetic field diffusion time measured for each probe in Eddy shot z3491

Probe	ΔB_t B-field diffusion time measured (ns)
b290b	712
b350b	814
BIB5000	0

If we compare the fringe probes above to the INNER MITL B-dot probes signals (Figure 4.76) we see the probes follow the general shape of the current pulse very closely, deviating in magnitude only slightly near the stagnation bump. The delay seen in the fringe B-dot probes is also not seen in the Inner- MITL B-dot probes, with the same explanation as above for the likely reason why.

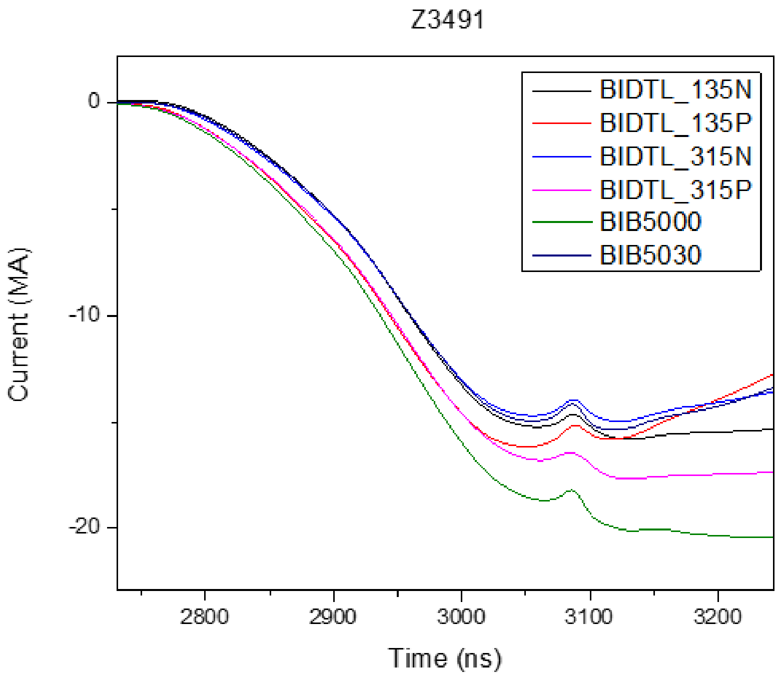

Figure 4.76: Z3491 Current traces from magnetic field probes in the Inner-MITL region.

As shown above, all fringe B-dot probes used in the Eddy campaign measured a time delay that ranges from 1 ns - 814 ns. The cause of this delay is likely due to the diffusion through the walls of the slotted aluminium return can structure. This structure is reported to be 750 μm thick with some small variation in thickness. A simple diffusion time calculation (4.3),

$$\tau = \frac{\mu a^2}{\eta} \tag{4.3}$$

with a being the thickness of the wall, μ being the permitivity, and η being the resistivity of solid aluminium ($2.8x10^{-8}\Omega$m) shows it would take 251 microseconds for the field to penetrate a solid 750μm aluminium wall. With the measured time scales in the 100's of nanoseconds it is likely that the state of the wall has a large effect on the diffusion time, and is likely not solid since the rapidly rising current of the Z-machine will cause resistive changes and heating in the return structure.

To investigate the state of the wall we used Spitzer resistivity

$$\eta_{\perp} = \frac{4\sqrt{2\pi}}{3} \frac{Ze^2 m_e^{1/2} \ln\Lambda}{(4\pi\varepsilon_0)^2 (k_{\mathrm{B}} T_e)^{3/2}} \tag{4.4}$$

where Z is the ionization, e is the electron charge, m_e is the electron mass, $\ln\Lambda$ is the Coulomb logarithm, ε_0 is the electric permittivity of free space, k_B is Boltzmann's constant, and T_e is the electron temperature in kelvins. Using historical data for the resistivity of aluminium, with a Z varying linearly over the temperature range from 1-4, we can plot the resistivity and resistive soak through time vs temperature (Figure 4.77). The plot shows that resistivity starts small (solid) and rises as temperature increases, the big peak in resistivity is just after the melting point where the aluminium is in a melt/liquid phase. Resistivity drops rapidly after this as the gas ionizes into a plasma. The smallest calculated soak-through time occurs in the liquid aluminium phase at 10's of microseconds. In order to achieve the right order of magnitude soak-through time, the resistivity of the return can structure needs to be on the order of $10^{-5}\Omega$m, which it does not reach with Spitzer.

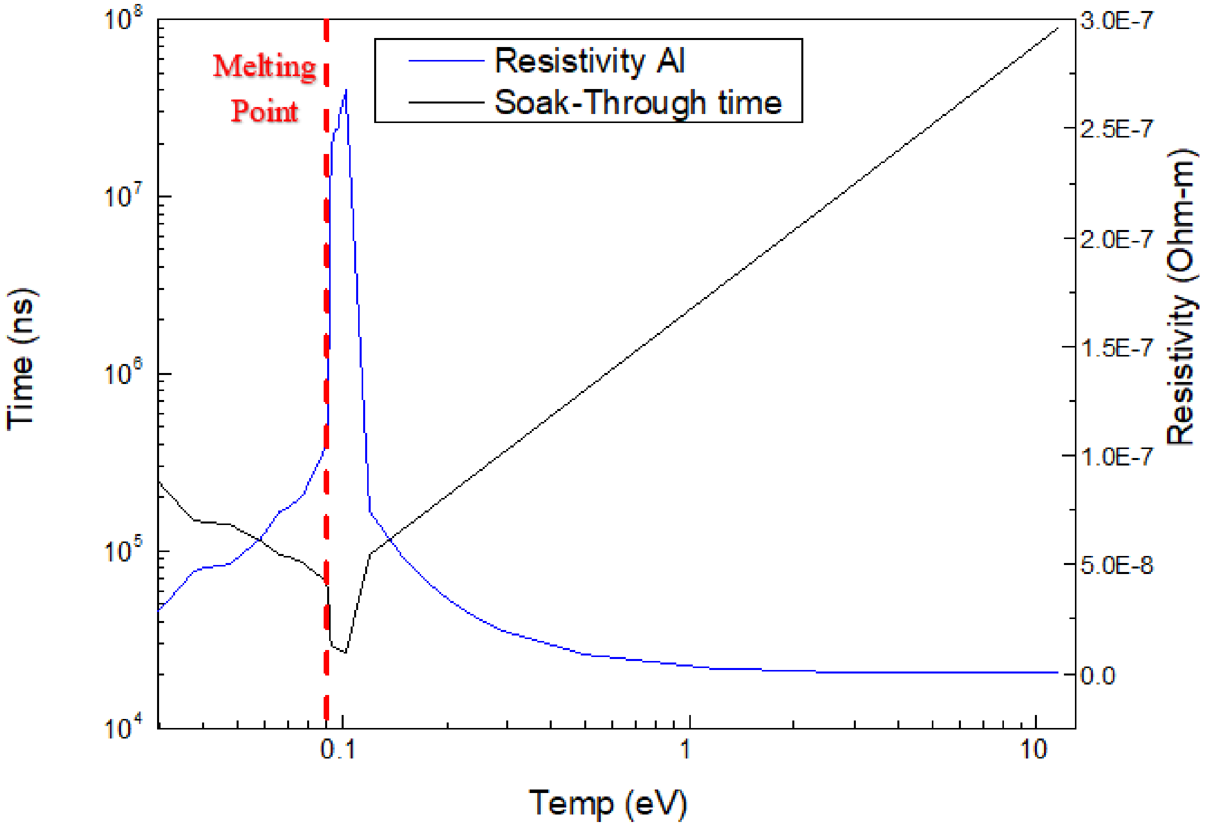

Figure 4.77: Spitzer resistivity of aluminium and diffusive soak through time versus temperature

Using data from Peterson et al [64], we reconstruct the LMD resistivity plot (Figure 4.78) for aluminium at a density of 2.71 g/cc vs. Temperature. With this data we then calculate the resistive soak-through time vs temperature. Again we see a large jump in resistivity when the temperature reaches melting point. When the temperature reaches >4 eV the soak-through time approaches values that are in line with what is seen in the probe measurements. It is important to note that in the referenced paper, the author looks at densities much lower than the one pictured here. In all of those densities, the resistivity approaches $\sim 10^{-5}\Omega$m faster, meaning they would have soak-through times in the 10's to 100's of ns. Without further diagnostic data, it is hard to say exactly what state the return can is in, though it is likely that based on LMD resistivity the return can is in a liquid/gas phase.

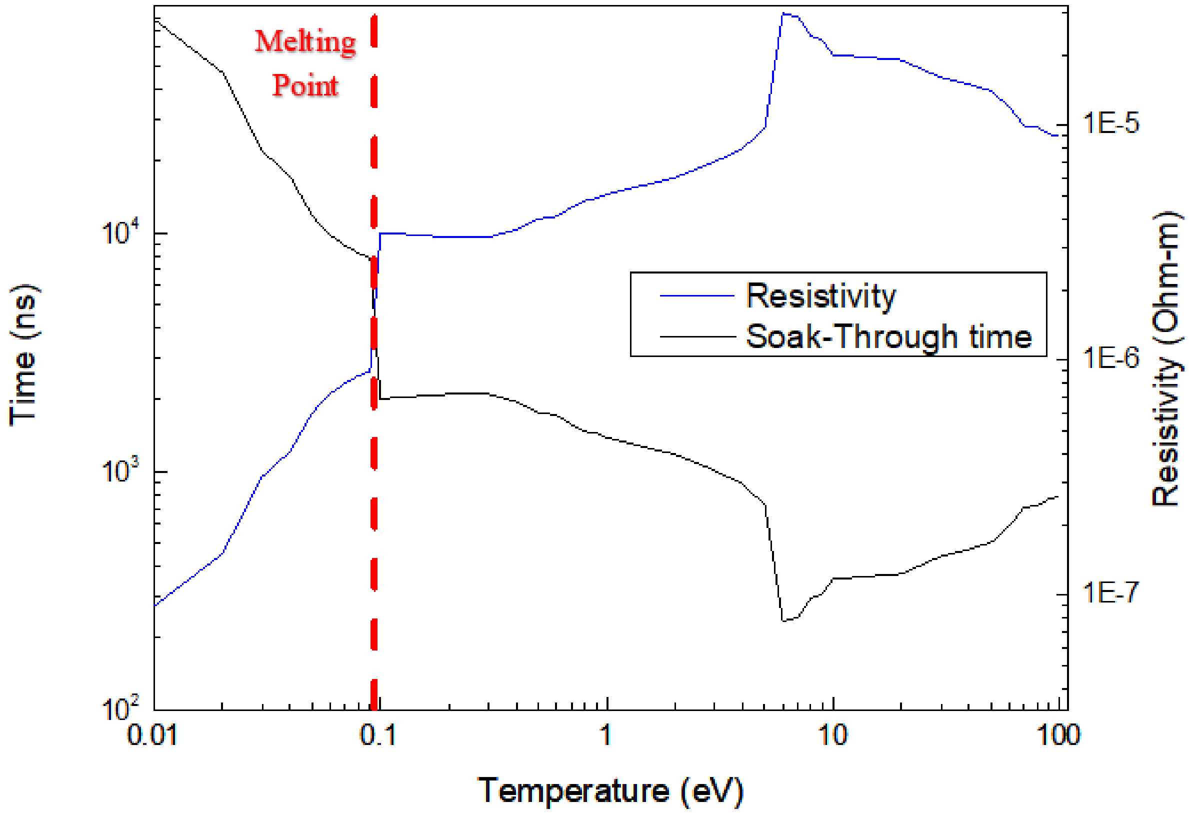

Figure 4.78: LMD resistivity of aluminium and diffusive soak through time versus temperature

With the above calculations and justification for the large time delay in signals, we attempt to use the triangulation technique on shot Z3423 by taking the peak value of each of the measured probes, the results of this are shown in Figure 4.79. The dark blue circles denote a top probe 3mm from the base of the mount, while the light blue circles denote a bottom probe 2 mm from the base of the mount. The red circles on the magnetic field traces denote the peak magnetic field values. The dark blue top probes indicate an offset towards 210°, the light blue bottom probes also indicate an offset towards the 210 probe mount. The slight shift in direction of current density from top probes to bottom probes, indicates moving current density. The measured offset could be due to an offset in current in the return structure and not necessarily the liner itself. This could also be a function of the presence of the return structure itself, as the return structure wall in front of the 210°mount is significantly smaller than that of the 290°and 350°, thus the larger signals measured could be due to an increased fringing field around the return structure at 210°. Though this behavior is not as overtly seen in the low resolution Maxwell simulations.

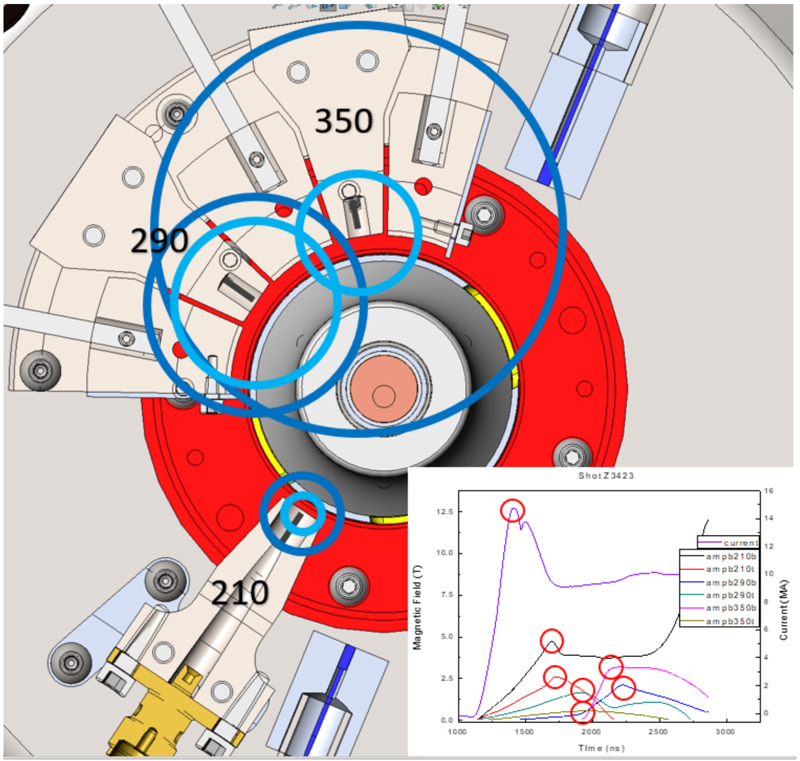

Figure 4.79: Shot Z3423 Triangulation with magnetic field probes peak signal circled in red

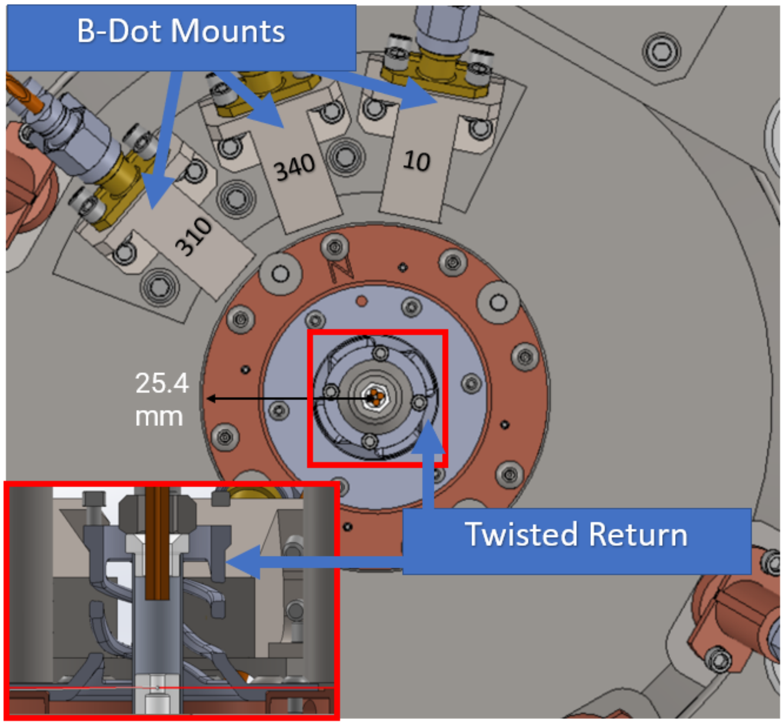

Figure 4.80: Dynamic Screw Pinch shot series load design with probe locations.

Figure 4.80 shows the Dynamic Screw Pinch (DSP) shot campaign load with twisted return structure (red square) and the location of the B-dot mounts with respect to the load. B-dots are located at three azimuthal locations, 310 °, 340°, and 10°. With the 10°probe measuring B_θ of the nearest twisted return arm.

.

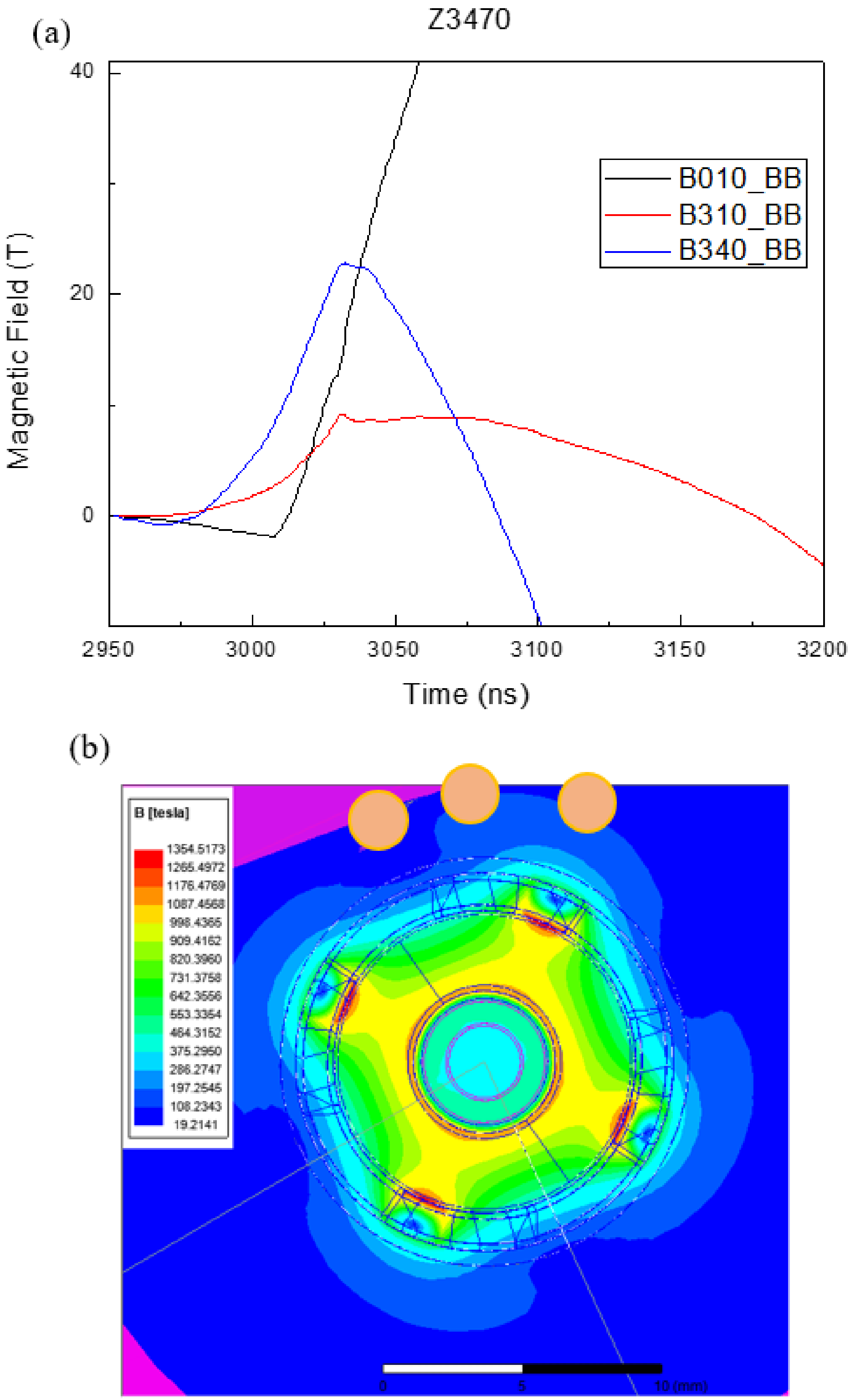

Figure 4.81: Z3470 Magnetic field traces (a) and Maxwell simulation of magnetic field magnitudes of the load.

In DSP shot Z3470 only the bottom magnetic field probes survived through the current pulse (Figure 4.81a) and were of the similar magnitudes to in-house initial low/res Maxwell simulations for the geometry (Figure 4.81b), with probe locations denoted by the orange dots. When examining the magnetic field traces, we see that the magnetic field probes all exhibit the stagnation bump. Of particular interest is the 10°probe shooting off into infinity just after stagnation. This is likely an indication of a potential flashover near this probe location, and this was later confirmed via imaging diagnostics in which current was shunted (near 10°probe location) down to 16 MA. Unfortunately because of this shunting, not much meaningful data can be pulled from this shot.

Chapter 5

Conclusions and Final Thoughts

”Roads go ever ever on
Under cloud and under star,
Yet feet that wandering have gone
Turn at last to home afar.”
-J.R.R. Tolkien, The Hobbit, ”The Last Stage”

5.1 Asymmetry in a Coaxial Gap Breakdown is Asymmetry In Current Density Distribution: Scaling Behaviors and Mitigation

Throughout the previous chapter, we have shown over thousands of shots through the use of an array of magnetic field probes that asymmetry in breakdown about the azimuth of a coaxial gap cause asymmetries in current density distribution along the axis of the electrode and persist for the duration of the current pulse. This behavior was shown to scale to megaampere analogous experiments on COBRA. These measured asymmetries in current density can be influenced by changes in the gap size and penetration depth.

Through the use of Fowler-Nordheim analysis, we have shown a shown a link between current density movement and increasing enhancement factor. In addition we have shown that the enhancement factor for a coaxial gap changes with varying gap size and penetration depth, and that this change is likely dominated by the electrode geometry, area of penetrating electrode, and the creation and destruction of microprotrusions that are large compared to the surface of the cathode. For gap sizes of 150 μm, 330 μm, 700 μm, the enhancement factor increases with penetration depth, which indicates an increase in current density movement, and this behavior is dominated by the electrode geometry and the surface area for breakdowns to form. For gap sizes of 50 μm, 100 μm, the average enhancement factor decreases with increasing penetration depth, indicating a decrease in current density movement, and is likely dominated by the increased number of breakdowns that result in significant topological changes to the surface of th electrode. This behavior causes the surface to smooth further decreasing microprotrusion height and thus enhancement factor.

At a megaampere, we have shown that coating the head of liners with various materials has an effect on breakdown formation, and that there is a correlation to these effects to the work function of the material used and the surface profile of the coating. Specifically we see increased initiation times for copper and gold, while decreasing initiation for Aerodag-G. In addition we have shown the first fully filled gap, and subsequent symmetric current density distribution in a coaxial gap from an Aerodag coated liner head. This is likely caused by the uniformly spaced surface imperfections and flaky conductive material that is accelerated by the voltage into the surface of electrodes to initiate explosively driven breakdown that spreads more material into the gap (some molten, some in the form of an expanding plasma jet).

In addition, we applied an external axial (z) magnetic field to the vacuum gap at a megaampere. We showed that it has an effect on the formation and propagation of breakdowns, increasing azimuthal spread of plasma and thus current density distribution in the liner. Again, we saw a full gap fill when using an Aerodag-G off-set coating. Showing that with an axial field even a severely off-set liner can achieve uniform plasma fill of the gap and thus current density distribution. Through analysis of gated optical images the main driving factors for increasing the fill of plasma around a magnetized gap are likely to be; 1) JxB on the plasma jet spreading plasma out into the gap, giving more area for current to be carried countering its ability to increase the number of breakdowns based on ionacoustic instability. 2) new breakdown formations in the opposite direction of JxB are driven by the anti-amperian motion caused by the presence of the external magnetic field.

We were also able to field fringe magnetic field probes on ride along shot campaigns on the Sandia Z-machine at $\sim$26 MA. We found that even in the harsh chamber environment, the triangulation technique can still measure information about the return can and potentially the load.

5.2 Implications and Final Thoughts

I have mentioned previously that coaxial gaps are in many different devices, such as the MagLIF design for the Sandia z-machine, transmission lines for various pulsed power devices, ion propulsion engines, plasma sources, etc. But what are the implications of the findings in this document for these devices?

For the push fit MagLIF design, if a coaxial gap is present we have shown it is probably not a problem for the gap at the cathode power feed because of the benefits of the external axial magnetic field and how rapid current will become symmetric in the load with respect to when the load with compress, but retrograde cathode motion could be an issue for the inner transmission line that has fringed axial magnetic field lines across the gap.

For ion propulsion engines, an Aerodag coated surface could be beneficial for fast plasma formation, and retrograde motion means you can potentially control arc formation direction in a rudimentary way with an external Magnetic field. Varying the gap size and penetration depth here could also be beneficial in increasing breakdown formation and current density distribution for initiation.

The asymmetries in breakdown formation and thus current density is likely an issue for most machines under 10s of MA and without an axial field that have a coaxial gap either in the power feed or the transmission lines.

The information presented here, while abundant, is still only just scratching the surface of the mechanics and behavior of breakdown formations in a coaxial gap. Plenty of work is left to be done and through my study of this it is no wonder that questions on breakdown have continued to be studied since$\sim$1905. Hopefully this work helps inch the field closer to understanding.

Bibliography

[1] A. Ainabayev, B. Berdenova, J. Norem, and Z. Insepov. Modeling of High-Gradient Vacuum Breakdown. (Md):1–8, 2014.

[2] David J Ampleford, SV Lebedev, SN Bland, SC Bott, JP Chittenden, CA Jennings, VL Kantsyrev, AS Safronova, VV Ivanov, DA Fedin, et al. Dynamics of conical wire array z-pinch implosions. *Physics of Plasmas*, 14(10):102704, 2007.

[3] André Anders and George Yu Yushkov. Ion flux from vacuum arc cathode spots in the absence and presence of a magnetic field. *Journal of Applied Physics*, 91(8):4824–4832, 2002.

[4] Charles C. Baker, Gustav A. Carlson, and Robert A. Krakowski. Trends and Developments in Magnetic Confinement Fusion Reactor Concepts. *Nuclear technology/fusion*, 1(1):5–78, 1981.

[5] I. I. Beilis. Vacuum arc cathode spot grouping and motion in magnetic fields. *IEEE Transactions on Plasma Science*, 30(6):2124–2132, 2002.

[6] I. I. Beilis. Vacuum arc cathode spot grouping and motion in magnetic fields. *IEEE Transactions on Plasma Science*, 30(6):2124–2132, 2002.

[7] I. I. Beilis. The vacuum arc cathode spot and plasma jet: Physical model and mathematical description, 2003.

[8] Isak I. Beilis. State of the theory of vacuum arcs. *IEEE Transactions on Plasma Science*, 29(5 I):657–670, 2001.

[9] Isak I Beilis. *Plasma and spot phenomena in electrical arcs* . 2020.

[10] R Beuhler and L Friedman. Larger cluster ion impact phenomena. *Chemical Reviews*, 86(3):521–537, 1986.

[11] GP Beukema. Conditioning of a vacuum gap by sparks and ion bombardment. *Physica*, 61(2):259–274, 1972.

[12] S. C. Bott-Suzuki, L. S. Caballero Bendixsen, S. W. Cordaro, I. C. Blesener, C. L. Hoyt, A. D. Cahill, B. R. Kusse, D. A. Hammer, P. A. Gourdain, C. E. Seyler, J. B. Greenly, J. P. Chittenden, N. Niasse, S. V. Lebedev, and D. J. Ampleford. Investigation of radiative bow-shocks in magnetically accelerated plasma flows. *Physics of Plasmas*, 22(5), 2015.

[13] S. C. Bott-Suzuki, S. W. Cordaro, L. S. Caballero Bendixsen, L. Atoyan, T. Byvank, W. Potter, B. R. Kusse, J. B. Greenly, and D. A. Hammer. Study of the time-resolved, 3-dimensional current density distribution in solid metallic liners at 1 MA. *Physics of Plasmas*, 23(9):1–7, 2016.

[14] Simon C. Bott-Suzuki, Samuel W. Cordaro, L. Atoyan, T. Byvank, W. Potter, B. R. Kusse, J. B. Greenly, D. A. Hammer, and C. A. Jennings. The Role of Ion Acoustic Instability in the Development of the Azimuthal Current Density Profile in Liner Experiments at 1 MA. *IEEE Transactions on Plasma Science*, 46(6):1921–1928, 2018.

[15] T. J. M. Boyd and J. J. Sanderson. *The Physics of Plasmas*. Cambridge University Press, 2003.

[16] SI Braginskii. Reviews of plasma physics, consultants bureau, new york,(1965); vol. 1.

[17] Robert T Brown and David C Smith. Laser-induced gas breakdown in the presence of preionization. *Applied Physics Letters*, 22(5):245–247, 1973.

[18] Tom Byvank. Applied Axial Magnetic Field Effects on Extended Magnetohydrodynamics Laboratory Plasma Jets : Experiments and Simulations. (May), 2018.

[19] P. Chapelle, J. P. Bellot, H. Duval, A. Jardy, and D. Ablitzer. Modelling of plasma generation and expansion in a vacuum arc: application to the vacuum arc remelting process. *Journal of Physics D: Applied Physics*, 35(2):137–150, 2002.

[20] Francis F. Chen. *Erratum to: Introduction to Plasma Physics and Controlled Fusion*. 2018.

[21] S Cook and RV Latham. Microscopic surface processes associated with the bouncing impact of charged microparticles on high voltage electrodes. *Physica B+ C*, 104(1-2):17–24, 1981.

[22] S. W. Cordaro and S. C. Bott-Suzuki. Time and space resolved current density mapping in three dimensions using magnetic field probe array in a high voltage coaxial gap. *Journal of Applied Physics*, 122(21), 2017.

[23] Lawrence Cranberg. The initiation of electrical breakdown in vacuum. *Journal of Applied Physics*, 23(5):518–522, 1952.

[24] M. E. Cuneo, M. C. Herrmann, D. B. Sinars, S. A. Slutz, W. A. Stygar, R. A. Vesey, A. B. Sefkow, G. A. Rochau, G. A. Chandler, J. E. Bailey, J. L. Porter, R. D. McBride, D. C. Rovang, M. G. Mazarakis, E. P. Yu, D. C. Lamppa, K. J. Peterson, C. Nakhleh, S. B. Hansen, A. J. Lopez, M. E. Savage, C. A. Jennings, M. R. Martin, R. W. Lemke, B. W. Atherton, I. C. Smith, P. K. Rambo, M. Jones, M. R. Lopez, P. J. Christenson, M. A. Sweeney, B. Jones,

L. A. McPherson, E. Harding, M. R. Gomez, P. F. Knapp, T. J. Awe, R. J. Leeper, C. L. Ruiz, G. W. Cooper, K. D. Hahn, J. McKenney, A. C. Owen, G. R. McKee, G. T. Leifeste, D. J. Ampleford, E. M. Waisman, A. Harvey-Thompson, R. J. Kaye, M. H. Hess, S. E. Rosenthal, and M. K. Matzen. Magnetically driven implosions for inertial confinement fusion at Sandia National Laboratories. *IEEE Transactions on Plasma Science*, 40(12):3222–3245, 2012.

[25] JE Daalder. A cathode spot model and its energy balance for metal vapour arcs. *Journal of Physics D: Applied Physics*, 11(12):1667, 1978.

[26] Caio P. de Castro, Thiago A. de Assis, Roberto Rivelino, Fernando de B. Mota, and Caio M. C. de Castilho. Using static linear response theory to describe field emission field enhancement and a field-induced insulator-conductor transition. *Journal of Vacuum Science and Technology B*, 39(6):060601, 2021.

[27] Richard G Forbes. 21st Century Planar Field Emission Theory and its Role in Vacuum Breakdown Science. (1), 2021.

[28] Richard G. Forbes, Jonathan H.B. Deane, Andreas Fischer, and Marwan S. Mousa. Fowler-nordheim plot analysis: A progress report. *Jordan Journal of Physics*, 8(3):125–147, 2015.

[29] Ralph Howard Fowler. The thermionic emission constant a. *Proceedings of the Royal Society of London. Series A, Containing Papers of a Mathematical and Physical Character*, 122(789):36–49, 1929.

[30] Ralph Howard Fowler and Lothar Nordheim. Electron emission in intense electric fields. *Proceedings of the Royal Society of London. Series A, Containing Papers of a Mathematical and Physical Character*, 119(781):173–181, 1928.

[31] Jeffrey P. Freidberg. *Plasma physics and fusion energy*, volume 9780521851. 2007.

[32] Peter T Gallagher. Introduction to plasma physics (py5012) lectures 1 & 2: Basic concepts. *Lecture slides* 2012.

[33] J. B. Greenly, J. D. Douglas, D. A. Hammer, B. R. Kusse, S. C. Glidden, and H. D. Sanders. A 1ma, variable risetime pulse generator for high energy density plasma research. *Review of Scientific Instruments*, 79(7):073501, 2008.

[34] John Greenly, Matthew Martin, Isaac Blesener, David Chalenski, Patrick Knapp, and Ryan McBride. The role of flux advection in the development of the ablation streams and precursors of wire array z-pinches. *AIP Conference Proceedings*, 1088(1):53–56, 2009.

[35] RJ Harvey, RA Lee, AJ Miller, and JK Wigmore. Aspects of field emission from silicon diode arrays. *IEEE Transactions on Electron Devices*, 38(10):2323–2328, 1991.

[36] Emmanouel Hourdakis, Garnett W. Bryant, and Neil M. Zimmerman. Electrical breakdown in the microscale: Testing the standard theory. *Journal of Applied Physics*, 100(12), 2006.

[37] B. Jüttner. Erosion Craters and Arc Cathode Spots in Vacuum. *Beiträge aus der Plasmaphysik*, 19(1):25–48, 1979.

[38] Burkhard Jüttner and Ingmar Kleberg. The retrograde motion of arc cathode spots in vacuum. *Journal of Physics D: Applied Physics*, 33(16):2025–2036, 2000.

[39] Michael Keidar and Isak I. Beilis. *Electrical Discharges*, volume 5. 2018.

[40] A. J. Kemp, M. M. Basko, and J. Meyer-ter Vehn. Ignition conditions for magnetically insulated tamped ICF targets in cylindrical geometry. *Nuclear Fusion*, 41(2):235–241, 2001.

[41] IG Kesaev. Electric-arc cathode processes, Nauka, Moscow 1968.

[42] Yuto Kikuchi, Shigeyasu Matsuoka, Akiko Kumada, Kunihiko Hidaka, Taiki Donen, and Mitsuru Tsukima. Motion observation of particles between electrodes and subsequent breakdown phenomena in vacuum. *Proceedings - International Symposium on Discharges and Electrical Insulation in Vacuum, ISDEIV*, pages 133–136, 2014.

[43] Ronald C. Kirkpatrick, Irvin R. Lindemuth, and Marjorie S. Ward. Magnetized Target Fusion: An Overview. *Fusion Technology*, 27(3):201–214, 1995.

[44] P. F. Knapp, M. R. Martin, D. H. Dolan, K. Cochrane, D. Dalton, J. P. Davis, C. A. Jennings, G. P. Loisel, D. H. Romero, I. C. Smith, E. P. Yu, M. R. Weis, T. R. Mattsson, R. D. McBride, K. Peterson, J. Schwarz, and D. B. Sinars. Direct measurement of the inertial confinement time in a magnetically driven implosion. *Physics of Plasmas*, 24(4), 2017.

[45] Jonathan Kolbeck, André Anders, Isak I. Beilis, and Michael Keidar. Micro-propulsion based on vacuum arcs. *Journal of Applied Physics*, 125(22), 2019.

[46] AG Korop, IS Genes, VS Ronin, NB Kartavenko, TD Pavlova, and NF Ordzhonikidze. Cytologic study in assessing the effectiveness of chemotherapy in patients with ovarian cancer. *Laboratornoe delo*, (9):49–51, 1989.

[47] F. Le Pimpec, C. Gough, M. Paraliev, R. Ganter, C. Hauri, and S. Ivkovic. Vacuum breakdown limit and quantum efficiency obtained for various technical metals using dc and pulsed voltage sources. *Journal of Vacuum Science and Technology A: Vacuum, Surfaces, and Films*, 28(5):1191–1202, 2010.

[48] Shimin Li, Yingsan Geng, Zhiyuan Liu, and Jianhua Wang. A breakdown mechanism transition with increasing vacuum gaps. *IEEE Transactions on Dielectrics and Electrical Insulation*, 24(6):3340–3346, 2017.

[49] I. R. Lindemuth and R. C. Kirkpatrick. Parameter space for magnetized fuel targets in inertial confinement fusion. *Nuclear Fusion*, 23(3):263–284, 1983.

[50] Evgenii Aleksandrovich Litvinov, Gennadii A Mesyats, and DI Proskurovskii. Field emission and explosive electron emission processes in vacuum discharges. *Soviet Physics Uspekhi*, 26(2):138, 1983.

[51] Received May. Further studies in the emission of electrons from cold metals. *Proceedings of the Royal Society of London. Series A, Containing Papers of a Mathematical and Physical Character*, 124(795):699–723, 1929.

[52] R D Mcbride, D E Bliss, M R Gomez, S B Hansen, M R Martin, C A Jennings, S A Slutz, D C Rovang, P F Knapp, P F Schmit, T J Awe, M H Hess, R W Lemke, D H Dolan, D C Lamppa, M R L Jobe, L Fang, K D Hahn, G A Chandler, G W Cooper, C L Ruiz, A J Maurer, G K Robertson, M E Cuneo, D B Sinars, K Tomlinson, G Smith, R R Paguio, T P Intrator, T E Weber, and J B Greenly. SANDIA REPORT Implementing and diagnosing magnetic flux compression on the Z pulsed power accelerator. 2015.

[53] G. A. Mesyats. Ectons and their role in plasma processes. *Plasma Physics and Controlled Fusion*, 47(5 A), 2005.

[54] G. A. (Gennadii Andreevich) Mesyats. *Cathode phenomena in a vacuum discharge : the breakdown, the spark, and the arc*. Nauka Publishers, Moscow, 2000.

[55] Gennady A. Mesyats. Ecton mechanism of the cathode spot phenomena in a vacuum Arc. *IEEE Transactions on Plasma Science*, 41(4):676–694, 2013.

[56] Gennady A. Mesyats. Ecton mechanism of the cathode spot phenomena in a vacuum arc. *IEEE Transactions on Plasma Science*, 41:676–694, 2013.

[57] Dan Nicolaescu. Physical basis for applying the fowler–nordheim j–e relationship to experimental i–v data. *Journal of Vacuum Science and Technology B: Microelectronics and Nanometer Structures Processing, Measurement, and Phenomena*, 11(2):392–395, 1993.

[58] M Okawa, T Shioiri, H Okubo, and S Yanabu. Area effect on electric breakdown of copper and stainless steel electrodes in vacuum. *IEEE Transactions on Electrical Insulation*, 23(1):77–81, 1988.

[59] J. Ongena, R. Koch, R. Wolf, and H. Zohm. Magnetic-confinement fusion. *Nature Physics*, 12(5):398–410, 2016.

[60] S. A. Onischenko, E. V. Nefedtsev, and D. I. Proskurovsky. Magnetic field effect on the pulsed breakdown strength of vacuum gaps. *Proceedings - International Symposium on Discharges and Electrical Insulation in Vacuum, ISDEIV*, 2016-Novem:3–6, 2016.

[61] J Robert Oppenheimer. On the quantum theory of the capture of electrons. *Physical review*, 31(3):349, 1928.

[62] NE Perskii, Valerii Ivanovich Sysun, and Yulian Davydovich Khromoi. Dynamics of vacuum-discharge cathode spots. *Teplofizika vysokikh temperatur*, 27(6):1060–1067, 1989.

[63] F. E. Peterkin and P. F. Williams. Physical mechanism of triggering in trigatron spark gaps. *Applied Physics Letters*, 53(3):182–184, 1988.

[64] Kyle J. Peterson, Daniel B. Sinars, Edmund P. Yu, Mark C. Herrmann, Michael E. Cuneo, Stephen A. Slutz, Ian C. Smith, Briggs W. Atherton, Marcus D. Knudson, and Charles Nakhleh. Electrothermal instability growth in magnetically driven pulsed power liners. *Physics of Plasmas*, 19(9), 2012.

[65] DI Proskurovsky and VP Rotshtein. Electron current density on anode of vacuum diode with needle cathode operating under explosive emission conditions. *Soviet Physics Journal*, 16(11):1602–1603, 1973.

[66] J.D. Ramboz. Machinable rogowski coil, design, and calibration. *IEEE Transactions on Instrumentation and Measurement*, 45(2):511–515, 1996.

[67] O. W. Richardson. Thermionic emission from systems with multiple thresholds. *Proceedings of the Physical Society of London*, 36(1):383–398, 1923.

[68] P. F. Schmit and D. E. Ruiz. A conservative approach to scaling magneto-inertial fusion concepts to larger pulsed-power drivers. *Physics of Plasmas*, 27(6), 2020.

[69] P. F. Schmit, A. L. Velikovich, R. D. McBride, and G. K. Robertson. Controlling rayleigh-taylor instabilities in magnetically driven solid metal shells by means of a dynamic screw pinch. *Physical Review Letters*, 117(20):1–6, 2016.

[70] W Schottky. Cold and hot electron discharges. *Z. Phys*, 14:63, 1923.

[71] Peter Clark Schrafel. MAGNETIZED PLASMA JETS IN EXPERIMENT AND SIMULATION by. (August), 2014.

[72] T. B. A. Senior and J. L. Volakis. Appendix B: Special functions. *Approximate Boundary Conditions in Electromagnetics*, pages 312–326, 2011.

[73] B. Seznec, Ph Dessante, L. Caillault, J. L. Babigeon, Ph Teste, and T. Minea. Controlled electron emission and vacuum breakdown with nanosecond pulses. *Journal of Physics D: Applied Physics*, 49(23), 2016.

[74] D. B. Sinars, M. A. Sweeney, C. S. Alexander, D. J. Ampleford, T. Ao, J. P. Apruzese, C. Aragon, D. J. Armstrong, K. N. Austin, T. J. Awe, A. D. Baczewski, J. E. Bailey, K. L. Baker, C. R. Ball, H. T. Barclay, S. Beatty, K. Beckwith, K. S. Bell, J. F. Benage, N. L. Bennett, K. Blaha, D. E. Bliss, J. J. Boerner, C. J. Bourdon, B. A. Branch, J. L. Brown, E. M. Campbell, R. B. Campbell, D. G. Chacon, G. A. Chandler, K. Chandler, P. J. Christenson, M. D. Christison, E. B. Christner, R. C. Clay, K. R. Cochrane, A. P. Colombo, B. M. Cook, C. A. Coverdale, M. E. Cuneo, J. S. Custer, A. Dasgupta, J. P. Davis, M. P. Desjarlais, D. H. Dolan, J. D. Douglass, G. S. Dunham, S. Duwal, A. D. Edens, M. J. Edwards, E. G. Evstatiev, B. G. Farfan, J. R. Fein, E. S. Field, J. A. Fisher, T. M. Flanagan, D. G. Flicker, M. D. Furnish, B. R. Galloway, P. D. Gard, T. A. Gardiner, M. Geissel, J. L. Giuliani, M. E. Glinsky, M. R. Gomez, T. Gomez, G. P. Grim, K. D. Hahn, T. A. Haill, N. D. Hamlin, J. H. Hammer, S. B. Hansen, H. L. Hanshaw, E. C. Harding, A. J. Harvey-Thompson, D. Headley,

M. C. Herrmann, M. H. Hess, C. Highstrete, O. A. Hurricane, B. T. Hutsel, C. A. Jennings, O. M. Johns, D. Johnson, M. D. Johnston, B. M. Jones, M. C. Jones, P. A. Jones, P. E. Kalita, R. J. Kamm, J. W. Kellogg, M. L. Kiefer, M. W. Kimmel, P. F. Knapp, M. D. Knudson, A. Kreft, G. R. Laity, P. W. Lake, D. C. Lamppa, W. L. Langston, J. S. Lash, K. R. Lechien, J. J. Leckbee, R. J. Leeper, G. T. Leifeste, R. W. Lemke, W. Lewis, S. A. Lewis, G. P. Loisel, Q. M. Looker, A. J. Lopez, D. J. Lucero, S. A. Maclaren, R. J. Magyar, M. A. Mangan, M. R. Martin, T. R. Mattsson, M. K. Matzen, A. J. Maurer, M. G. Mazarakis, R. D. McBride, H. S. McLean, C. A. McCoy, G. R. McKee, J. L. McKenney, A. R. Miles, J. A. Mills, M. D. Mitchell, N. W. Moore, C. E. Myers, T. Nagayama, G. Natoni, A. C. Owen, S. Patel, K. J. Peterson, T. D. Pointon, J. L. Porter, A. J. Porwitzky, S. Radovich, K. S. Raman, P. K. Rambo, W. D. Reinhart, G. K. Robertson, G. A. Rochau, S. Root, D. V. Rose, D. C. Rovang, C. L. Ruiz, D. E. Ruiz, D. Sandoval, M. E. Savage, M. E. Sceiford, M. A. Schaeuble, P. F. Schmit, M. S. Schollmeier, J. Schwarz, C. T. Seagle, A. B. Sefkow, D. B. Seidel, G. A. Shipley, J. Shores, L. Shulenburger, S. C. Simpson, S. A. Slutz, I. C. Smith, C. S. Speas, P. E. Specht, M. J. Speir, D. C. Spencer, P. T. Springer, A. M. Steiner, B. S. Stoltzfus, W. A. Stygar, J. Ward Thornhill, J. A. Torres, J. P. Townsend, C. Tyler, R. A. Vesey, P. E. Wakeland, T. J. Webb, E. A. Weinbrecht, M. R. Weis, D. R. Welch, J. L. Wise, M. Wu, D. A. Yager-Elorriaga, A. Yu, and E. P. Yu. Review of pulsed power-driven high energy density physics research on Z at Sandia. *Physics of Plasmas*, 27(7), 2020.

[75] J. C. Slattery, J. F. Friichtenicht, and D. O. Hansen. High-voltage breakdown initiated by particle impact. *Applied Physics Letters*, 7,23–25, 1965.

[76] I N Slivkov, V I Mikhaylov, N I Sidorov, and A I Nastyukha. Electrical breakdown and discharge in a vacuum. *FOREIGN TECHNOLOGY DIV WRIGHT-PATTERSON AFB OH*, 1972.

[77] S. A. Slutz. Scaling of magnetized inertial fusion with drive current rise-time. *Physics of Plasmas*, 25(8), 2018.

[78] S. A. Slutz, M. C. Herrmann, R. A. Vesey, A. B. Sefkow, D. B. Sinars, D. C. Rovang, K. J. Peterson, and M. E. Cuneo. Pulsed-power-driven cylindrical liner implosions of laser preheated fuel magnetized with an axial field. *Physics of Plasmas*, 17(5), 2010.

[79] Stephen A. Slutz and Roger A. Vesey. High-gain magnetized inertial fusion. *Physical Review Letters*, 108(2):1–5, 2012.

[80] D.A. Yager-Elorriaga, M.R. Gomez, D.E. Ruiz, S.A. Slutz, A.J. Harvey-Thompson, C.A. Jennings, P.F. Knapp, P.F. Schmit, M.R. Weis, T.J. Awe, G.A. Chandler, M. Mangan, C.E. Myers, J.R. Fein, B.R. Galloway, M. Geissel, M.E. Glinsky, S.B. Hansen, E.C. Harding, D.C. Lamppa, W.E. Lewis, P.K. Rambo, G.K. Robertson, M.E. Savage, G.A. Shipley, I.C. Smith, J. Schwarz, D.J. Ampleford, K. Beckwith, K.J. Peterson, J.L. Porter, G.A. Rochau, and D.B. Sinars. An overview of magneto-inertial fusion on the Z machine at Sandia National Laboratories. *Nuclear Fusion*, 62(4):042015, 2022.